TÉCNICO LISBOA

Small-volume membrane filtration using Centrifugal Nanofiltration Devices

Madalena Amaral Caldas

Thesis to obtain the Master of Science Degree in

Chemical Engineering

Supervisor(s): Prof. Vítor Manuel Geraldes Fernandes

Examination Committee

Chairperson: Prof. Isabel Maria Delgado Jana Marrucho Ferreira
Supervisor: Prof. Vítor Manuel Geraldes Fernandes
Member of the Committee: Prof. Mónica Cristina Faria Besteiro

December 2023

Declaration

I declare that this document is an original work of my own authorship and that it fulfills all the requirements of the Code of Conduct and Good Practices of the Universidade de Lisboa.

Acknowledgments

First of all, I would like to extend my deepest gratitude to my supervisors, Professor Vitor Geraldes and Professor Miguel Rodrigues, for suggesting this thesis, for their guidance and invaluable feedback. Their expertise and insights were essential in shaping this work.

Special acknowledgment goes to my colleague, Patrícia Henriques. Her guidance and patience throughout the experimental stages were crucial to the progress and quality of my research. Beyond her professional support, I also want to thank her for listening to my numerous frustrations and for her encouragement throughout the journey of this thesis.

Special thanks to my lab colleagues, who provided constructive criticism and much-needed breaks from the long hours of research.

To all my cherished friends—from those I've known since childhood and school to the ones I met in college—thank you for the encouragement, understanding, and the light-hearted moments that kept me sane during this intense period. A special acknowledgement to Bárbara, Catarina and Carolina, for being my biggest cheerleaders since day one. My experience at Técnico would not have been the same without you.

Heartfelt appreciation is extended to my family. To my mother and father, Luísa Amaral e Carlos Caldas, your unconditional belief in me and your constant love, support and patience have been crucial in this journey. I'd also like to specially thank my second father, Carlos Barata, without whom I wouldn't be the person I am today.

Last but certainly not least, to my boyfriend, Miguel Lopes, thank you for being my anchor, for your patience, and for always standing by my side through the highs and lows.

This accomplishment is not just my own but is the result of the collective efforts of everyone who has touched my life during this period.

Resumo

Nos últimos anos, a necessidade de métodos de filtração que minimizem a perda de amostras e recursos, especialmente em indústrias que manuseiam compostos de alto valor, tem crescido. Esta tese visa otimizar o desempenho de dispositivos de nanofiltração centrífuga (CNF), tornando-os mais eficientes para operações em pequena escala (cerca de 10 mL), sem comprometer a eficácia do processo de filtração.

Para alcançar este objetivo, foi desenvolvido um dispositivo CNF com design inovador, utilizando simulações de Dinâmica dos Fluidos Computacionais (CFD) para prever a pressão dentro do dispositivo. A metodologia incluiu a caracterização da membrana numa unidade SEPA, com área ativa de membrana de 140 cm^2, para estabelecer parâmetros de referência. Posteriormente, avaliou-se o dispositivo CNF, que possui uma área ativa de membrana de 2,4 cm^2. Os testes desempenhados nos dois tipos de dispositivos avaliaram a permeabilidade hidráulica e na rejeição de solutos (NaCl, lactose e $MgSO_4$) sob uma gama de pressões de 7 a 40 bar.

Os resultados mostraram que o CNF consegue replicar a permeação de água da SEPA. Contudo, a polarização da concentração afetou as taxas de rejeição e fluxo de permeado, especialmente para sais. O estudo também destacou a necessidade de testes extensivos para selecionar uma amostra representativa da membrana industrial.

Conclui-se que os dispositivos CNF são promissores para indústrias que pretendam economizar os seus recursos, onde a conservação de amostras é crucial. O estudo realça a importância de considerar a polarização de concentração e a variabilidade da membrana no design e metodologia de processos de nanofiltração, incentivando inovações futuras.

Palavras-chave: Filtração por membrana, Nanofiltração centrífuga, Célula de filtração de pequenos volumes, Variabilidade da membrana

Abstract

In recent years, the need for filtration methods that minimize the loss of samples and resources, especially in industries handling high-value compounds, has grown. This thesis aims to optimize the performance of Centrifugal Nanofiltration (CNF) devices, making them more efficient for small-scale operations (about 10 mL) without compromising the efficacy of the filtration process.

To achieve this goal, a CNF device with an innovative design was developed, using Computational Fluid Dynamics (CFD) simulations to predict the pressure inside the device. The methodology included characterizing the membrane in a SEPA unit, with an active membrane area of 140 cm^2, to establish reference parameters. Subsequently, the CNF device, which has a membrane active area of 2.4 cm^2, was evaluated. Tests performed on both equipment measured the hydraulic permeability and solute rejection (for NaCl, lactose, and $MgSO_4$) under a range of pressures from 7 to 40 bar.

The results showed that the CNF can replicate the water permeation of the SEPA unit. However, concentration polarization affected the rejection rates and permeate flux, especially for the salts. The study also highlighted the need for extensive testing to select a representative sample of the industrial membrane.

In conclusion, CNF devices are promising for industries who seek to save resources. The study highlights the importance of considering concentration polarization and membrane variability in the design and methodology of nanofiltration processes, encouraging future innovations.

Keywords: Membrane filtration, Centrifugal nanofiltration, Small-volume filtration device, Membrane variability

Contents

Acknowledgments v
Resumo vii
Abstract ix
List of Tables xv
List of Figures xvii
Nomenclature xxi
Glossary 1

1 Introduction **1**
1.1 Overview 1
1.2 Motivation 2
1.3 Objectives 2
1.4 Dissertation Development Methodologies 2
1.5 Thesis Outline 3

2 Membrane Filtration Background **5**
2.1 Pressure-driven Membrane Processes 6
2.2 Types of Membranes 9
2.3 Membrane Characterization 11
2.4 Membrane Transport Theory 12
2.4.1 Solution-diffusion Model 13
2.4.2 Pore-flow Model 15
2.5 Mass Transport Limitations 16
2.5.1 Fouling 16
2.5.2 Concentration Polarization 17
2.6 Nanofiltration 18
2.6.1 Nanofiltration Exclusion Mechanisms 20
2.7 Centrifugal Nanofiltration 24
2.7.1 CNF Device 26

3 Materials and Methods **29**
3.1 Materials 29

3.2 Methods . . . 29
3.2.1 SEPA . . . 29
3.2.2 CNF Device . . . 32
3.2.3 Simulation of experimental conditions . . . 38
3.2.4 Analytic methods . . . 40

4 SEPA **43**
4.1 Introduction . . . 43
4.2 Hydraulic Permeability . . . 45
4.3 Solute Rejection . . . 46

5 Centrifugal Nanofiltration Device **51**
5.1 Introduction . . . 51
5.2 Simulation postprocessing . . . 51
5.3 Membrane Preparation for CNF Device Testing . . . 57
5.4 Evaluation of SEPA Membrane in CNF Devices . . . 58
5.4.1 Preparation . . . 58
5.4.2 Pressure Correction Methodology . . . 59
5.4.3 Hydraulic Permeability . . . 61
5.4.4 Selection of Membranes for Rejection Testing . . . 62
5.4.5 Solute Rejection in CNF Device . . . 65
5.5 Introduction of a New Membrane Set . . . 69

6 Conclusions **73**

Bibliography **75**

A Chapter 3 Appendixes **79**
A.1 Membrane Properties . . . 79
A.2 SEPA Properties . . . 80
A.3 Frequency Calibration Line . . . 80
A.4 Calibration Lines . . . 81
A.4.1 $MgSO_4$ . . . 81
A.4.2 NaCl . . . 81
A.4.3 Lactose . . . 82

B Chapter 4 Appendixes **83**
B.1 Hydraulic permeability (SEPA) . . . 83
B.2 Membrane rejection and permeate flux (SEPA) . . . 84

C Chapter 5 Appendixes **87**

C.1 Pressure simulation 87

C.2 Pressure correction (CNF1) 91

C.3 Pressure correction (CNF2) 93

C.4 Hydraulic permeability (CNF1) 94

C.5 Solute rejection and permeate flux (CNF1) 95

C.6 Hydraulic permeability (CNF2) 98

C.7 Membrane rejection and permeate flux (CNF2) 99

List of Tables

2.1 Membrane processes with respective driving forces and applications. 6

2.2 Retention distinctions between nanofiltration (NF) and reverse osmosis (RO) [5]. 8

2.3 Pore size, operating pressure, compounds removed and retain particles for RO, NF, UF and MF [5, 8]. 9

4.1 Equation for the linear regression and its corresponding hydraulic permeability value, obtained from the slope. 45

4.2 NFS (TFC 100-250Da) membrane rejection specifications (Appendix A.1). 46

4.3 Average rejection results obtained in the SEPA unit with the feed pressure of 7.6 bar, and comparison with the reference values. 48

5.1 Integrated pressure in the membrane surface, at a rotational speed of 7000 rpm, and conversion to values in both Pascals (Pa) and bars (bar). 53

5.2 Pressure values on the membrane surface for the simulation at 7000 rpm. It includes the pressure applied by a 10 mL volume of fluid (p_3), the pressure at maximum fluid volume (p_1), and the pressure at the surface of a 10 mL volume (p_2). 55

5.3 Correlations between pressure (bar) as a function of rotational speed (rpm), various fluid volumes. 56

5.4 Relationship between desired pressure levels (expressed in bar) and their corresponding speed settings (in rpm) for the centrifuge. The ”Speed set in centrifuge” column indicates the rounded speed values set in the centrifuge. 57

5.5 Allocation of membranes to their respective devices. 58

5.6 Correlation between rotational speed (expressed in rpm), volume (in mL), and the corresponding pressure values in the centrifuge. 60

5.7 Final volume, final pressure, and corrected pressure values for different test conditions at varying rotational speeds. 60

5.8 Corrected pressure values for different solution concentrations at various test conditions and rotational speed. 61

5.9 Comparison of hydraulic permeability values obtained in the SEPA and in the CNF devices. 62

A.1 Properties of membrane used (NFS (TFC 100-250Da) - Sanitary NF Membrane, by *Synder Filtration (California, USA)*. The properties listed were consulted in the pdf downloaded from *Synder*'s website in September 2022. 79
A.2 SEPA unit features and technical specification. 80

List of Figures

2.1 Schematic representation of a membrane process [5]. 5

2.2 Schematic representation of a two phased system separated by a membrane (adapted from Mulder [5]). 6

2.3 Schematic representation of linear molecules passing through the membrane and globular molecules of the same molecular weight being rejected [6]. 7

2.4 Osmotic effects across a semipermeable membrane [6]. 8

2.5 Types of membranes based on morphologic structure. Adapted from Baker. 10

2.6 Cross-section of asymmetric membrane (image adapted from Yuenyao et al. [11]) 11

2.7 Water flux as a function of the applied pressure (adapted from Mulder [5]). 12

2.8 Schematic representation of mass transport through the membrane according to A) pore-flow model and B) solution-diffusion model [14]. 13

2.9 Schematic representation of chemical potential, pressure, and solvent activity gradients across the membrane, according to the solution-diffusion model [12]. 13

2.10 Schematic representation of chemical potential, pressure, and solvent activity gradients across the membrane, according to the pore-flow model [12]. 15

2.11 Concentration profile in membranes experiencing concentration polarization. (C_m – feed solution concentration at the membrane surface; C_b – bulk solution concentration; C_p – permeate concentration; δ – thickness of the boundary layer) [14]. 17

2.12 Commercial nanofiltration membranes and their properties [18]. 19

2.13 Schematic representation of the steric or size exclusion mechanism. (Adapted from Suhalim et al.). 20

2.14 Schematic representation of solute exclusion mechanisms [20]. 21

2.15 Schematic representation of Donnan effect. A) Positively charged membrane. B) Negatively charged membrane. Adapted from Suhalim et al.. 22

2.16 Schematic representation of how an ionic species nearing the NF membrane surface generates a repulsive image force [23]. 23

2.17 Schematic diagram of ions with hydration radius greater than the pore passing through [26]. 24

2.18 Top-down perspective of a fluid element rotating about an axis. The centrifugal force is represented by the blue vector, pointing radially outward from the rotation axis. The Coriolis force, shown by the green vector, is influenced by the fluid's velocity vector U, depicted by the grey vector. The direction of rotation and the fluid element's mass m are also highlighted. [2]. 25
2.19 Detailed overview of the CNF device components developed by Completo et al.. 26
2.20 CNF device, by Hams. A) Cross-sectional schematic highlighting the internal chambers and channels. B) Assembled device. [2] 27

3.1 Assembly of the SEPA CF Cell unit. 30
3.2 Schematic diagram of the SEPA crossflow filtration system. 31
3.3 SEPA fully assembled setup. 32
3.4 Design of the cylindrical body and lid as seen in the *Onshape* CAD (A) and after 3D printing (B). 33
3.5 Cross-section schematic representation of the CNF device. 34
3.6 Attachment mechanisms of the lid and cylindrical body. 34
3.7 Complete CNF device. 35
3.8 A) & B) Cross-sectional schematics of the CNF device, emphasizing membrane positioning. C) The 3D printed body with the membrane installed. 36
3.9 A) Sorvall™ RC 6 Plus Centrifuge, by *Thermo Scientific*. B) SS-34 Fixed Angle Rotor, by *Thermo Scientific*. 36
3.10 Schematic representation of the device inside the rotor and the solution within the device before centrifugation. The gray trapezoid represents the rotor. 37
3.11 Schematic representation of the liquid inside the device during the test. 38
3.12 Fluid geometry used for the *simFlow* simulation in two different views (A and B). 39
3.13 Mesh developed in *simFlow*. The inlet is indicated by the red plane (B), the outlet by the yellow plane (C), and the remaining green faces are defined as walls (A). 39

4.1 SEPA's membrane. 44
4.2 Water flux results in the SEPA unit. 45
4.3 Comparison of solute rejection obtained experimentally with manufacturer specifications. 47
4.4 SEPA unit permeate flux and rejection results. 49
4.5 Comparison of the permeate fluxes obtained for solutions with the same concentration but different solutes (Lactose, NaCl and $MgSO_4$). A) 5 g/L solutions. B) 10 g/L solutions. . 50

5.1 3D fluid volume simulation imported into *ParaView*, depicting the pressure distribution within the CNF device during the computational fluid dynamics (CFD) analysis. 52
5.2 Pressure variation in the membrane surface. 52
5.3 Results obtained from the application of the "Integrate Variables" tool, showing the integrated pressure within the selected section of the CNF device membrane surface. 53

5.4 Pressure contours illustrating the uniform pressure applied to the surface of the fluid. . . . 54
5.5 Visual representation of the process used to calculate pressure for volumes less than the maximum. . . . 54
5.6 Illustration of the 10 mL fluid volume obtained by clipping the original geometry, in the CNF device simulation. . . . 55
5.7 Correlation between rotational speed and pressure applied to the membrane, for various fluid volumes. . . . 56
5.8 Membrane section from the SEPA unit with the twenty-two individual membranes marked. The circular membranes in yellow were utilized in the subsequent CNF testing. . . . 57
5.9 Relationship between pressure (bar) and volume (mL) at varying centrifuge speeds ranging from 5600 rpm to 15700 rpm. Each line represents the trend for a specific rpm. . . . 59
5.10 Relationship between permeate flux (J_w) and applied pressure for SEPA and CNF membranes. Linear regression finds the hydraulic permeability, which is represented by the slope. . . . 62
5.11 Selection of eight membranes for CNF testing. The left panel shows the chosen membranes from the original 14. The right panel shows the chosen membranes with the new labeling (A to H). . . . 63
5.12 Hydraulic permeability values for all 14 membranes, with membranes A to H representing the selected ones. The horizontal lines represent the average permeability for both the entire set of membranes and the chosen ones. . . . 63
5.13 Comparison of permeate flux between the set of 14 membranes and the 8 selected membranes. . . . 64
5.14 Water permeate flux (J_w) of membranes A through H under varying pressure conditions. The black line represents the average permeability across all membranes at each pressure point. . . . 64
5.15 Comparison of average permeate flux as a function of applied pressure for the solutes Lactose, NaCl, and $MgSO_4$ between CNF devices and the SEPA unit. Error bars represent the standard deviation for the CNF measurements. . . . 65
5.16 Solute rejection rates of the three tested solutes – Lactose, NaCl, and $MgSO_4$ – across different applied pressures for each of the eight membrane devices (A-H). The average rejection trendlines for all membranes and for the membranes with superior rejection are highlighted in black and grey, respectively. . . . 66
5.17 Spatial positioning of individual membranes (A-H) in the SEPA section. Membranes highlighted in blue (D, F, G, H) consistently demonstrated the highest solute rejection rates, whereas those in orange (A, B, C, E) exhibited the lowest. . . . 66
5.18 Solute rejection rates of Lactose, NaCl, and $MgSO_4$ at varying flux rates. The graph compares the average rejection performance of membranes D, F, G, H against that of the SEPA unit. . . . 67

5.19 Comparative analysis of permeate flux (A) and solute rejection rates (B) for $MgSO_4$ solutions of two different concentrations (1 g/L and 2 g/L). The CNF device's performance is compared with the SEPA unit's results. 68
5.20 Schematic representation of the membrane sheet, illustrating both the SEPA's membrane and the locations from which the new set of membranes (numbered 1 through 8) were extracted. 69
5.21 Comparison of average hydraulic permeability as a function of pressure for two sets of membranes, CNF1 and CNF2 (Detailed data in Appendix C.6). 70
5.22 Comparison of average permeate flux for CNF1 and CNF2 membranes with varying pressures using three solutes: Lactose, NaCl, and $MgSO_4$. 70
5.23 Comparison of average rejection rates for CNF1 and CNF2 membranes with varying values of permeate flux, using three solutes: Lactose, NaCl, and $MgSO_4$. 71

A.1 Linear regression of flow as a function of frequency. 80
A.2 $MgSO_4$ calibration lines, for higher and lower concentrations. The line for lower concentration is used to determine the concentration of the permeate and other is used to determine the concentration of the concentrate. 81
A.3 NaCl calibration lines, for higher and lower concentrations. The line for lower concentration is used to determine the concentration of the permeate and other is used to determine the concentration of the concentrate. 81
A.4 Lactose calibration line, for low concentrations. 82
A.5 Lactose calibration lines, for higher concentrations. 82

Nomenclature

Greek symbols

$\Delta\pi$	Osmotic pressure gradient.
γ_1	Activity coefficient.
υ_i	Molar volume.

Roman symbols

Δp	Pressure gradient.
ω	Angular velocity.
ρ	Density.
A	Water phase transport parameter.
A_m	Membrane area.
B	Solute permeability coefficient.
B	Solute phase transport parameter.
C_f	Solute concentration in the feed.
c_i	Concentration of component i.
C_m	Solute concentration at the membrane's surface.
C_p	Solute concentration in the permeate.
$d\mu_i/dx$	Chemical gradient for component i.
D_s^m	Solute diffusion coefficient.
D_i	Diffusion coefficient.
J_i	Volumetric flux of component i.
J_s	Solute volumetrix flux.
J_w	Water volumetric flux.

K_w Solute-membrane partition coefficient.

l Pore lenght.

L_i Coefficient of proportionality.

L_p Hydraulic permeability.

m Mass.

p_f Pressure in the feed side of the membrane.

p_p Pressure in the permeate side of the membrane.

Q_w Water flow rate.

R Universal gas constant.

r Distance.

R_{obs} Observed rejection.

R_r Real rejection.

T Temperature.

V_m Molar volume of water.

Chemical Formula

Ca^{2+} Calcium ion.

Ca^{2+} Sulfate ion.

$CaCl_2$ Calcium chloride.

$K_2S_2O_5$ Potassium metabisulfite.

Mg^{2+} Magnesium ion.

$MgSO_4$ Magnesium sulfate.

Na_2SO_4 Sodium sulfate.

NaCl Sodium chloride.

SO_4^{2-} Sulfate ion.

Acronyms

ABS Acrylonitrile butadiene styrene.

CAD Computer-aided design.

CFD Computational Fluid Dynamics.

CNF Centrifugal Nanofiltration.

CP Concentration Polarization.

DSPM Donnan-Steric-Pore-Model.

DSPM-DE Donnan-Steric-Pore Model with Dielectric Exclusion.

MF Microfiltration.

MWCO Molecular weight cut-off.

NF Nanofiltration.

RO Reverse Osmosis.

SEDE Steric, Electric, and Dielectric Exclusion model.

STL Standard Triangle Language.

UF Ultrafiltration.

Chapter 1

Introduction

1.1 Overview

In recent years, the demand to embrace more sustainable methodologies has become the norm across all processes and industries. Filtration processes are no exception. Traditional methods, while effective, often require substantial resources, which becomes a real hinderance in industries such as the pharmaceutical research, where its activity involves the development of high value compounds. In this type of industry, research involves extensive testing using incredibly expensive samples, thus, it has become essential to find a solution that allows the filtration of smaller volume samples in order to significantly reduce not only the costs but also the otherwise inevitable waste.

Centrifugal Nanofiltration (CNF) represented a significant advance, allowing the concentration of molecules from small volume samples without the need for external pumping, thereby minimizing sample loss, operational costs and, consequently, the environmental footprint, addressing some of the most persistent challenges faced by traditional filtration methods.

The CNF device that will be studied in this thesis offers an innovative approach to nanofiltration, adapted to efficiently concentrate low molecular weight samples of small volume. This device has seen multiple iterations, originating from the pioneering work of Completo et al., whose aim was to create a laboratory-scale solution that could outperform traditional concentration methods. This prototype, predominantly made of aluminum, was inspired by centrifugal filtration devices and had a unique membrane orientation that ensured tangential flow of the solution due to centrifugal force. Although the prototype showed a promising concentration factor of up to 23, there were opportunities for further improvement. Hams then attempted to scale the CNF for commercial production, adopting a disposable design with materials like polycarbonate and 3D-printed components, but achieved a maximum concentration factor of only 5. Two significant areas of improvement identified were the sealing techniques and the potential increase in filtration pressure. Correia's version focused on optimizing the design, but effective sealing still presented challenges. With this historical context and known issues, the current research aims to improve the CNF device's design, building on the foundation established by Completo, Hams, and Correia, and addressing known limitations.

1.2 Motivation

This research is mainly motivated by the imperative need for sustainable and efficient filtration testing methods, especially in industries dealing with high-value, sensitive compounds. Traditional methods often require large volumes, leading to resource wastage and increased operational costs. Additionally, the environmental impact of these processes cannot be understated, given the global shift towards more sustainable practices. The CNF device, with its promise of small-volume testing, offers a future where industrial standards can be improved through an eco-friendly and economical alternative.

1.3 Objectives

The objective of this thesis is not only to improve the current capabilities of centrifugal nanofiltration devices, especially in terms of scalability, usability, and efficiency, but also to perfect the methodology for its industrial application. To achieve this, we will explore and validate a new centrifugal nanofiltration (CNF) device design, introducing a innovative sealing mechanism and integrating Computational Fluid Dynamics (CFD) simulations to predict and optimize performance parameters. Each chapter delves into critical aspects of this journey, from understanding the membrane's behavior under increasing pressure to the analysis of solute rejection rates and the eventual implications of device design on performance.

Additionally, given that membranes usually show consistent characteristics on a scale of approximately 1 m^2, we aim to determine whether it's feasible to select a membrane sample that accurately represents an industrial-grade membrane.

1.4 Dissertation Development Methodologies

The journey to develop and validate the redesigned centrifugal nanofiltration (CNF) device unfolded through a series of methodical steps. Initially, the new prototype was designed and built to overcome the limitations of existing CNF devices, by incorporating an innovative sealing mechanism.

Post the design phase, the research incorporated a Computational Fluid Dynamics (CFD) simulation, which is crucial in predicting the device's performance parameters. These simulations covered speeds between 3000 to 16000 rpm, following an extensive post-processing to built a correlation between centrifuge speed and pressure exerted on the membrane, for various feed volumes (5, 7, 12, and 15 mL).

Next, a 140 cm^2 membrane section was extracted from the membrane sheet selected for the research and characterized in the SEPA unit, a lab-scale filtration equipment designed to evaluate the efficacy of flat sheet membranes. The membrane was tested under the conditions described in its specification sheet, aiming to match the manufacturer's reference values. Additionally, hydraulic permeability and solute rejection tests were conducted at varying solute concentrations and pressures, ranging from 8 to 40 bar. The solutes examined were lactose, NaCl, and $MgSO_4$.

The final phase consisted of testing the CNF device using two sets of membranes: one from the membrane tested in the SEPA unit and another from a different section of the original membrane sheet.

The main goal was to determine whether the CNF device could replicate the results obtained in the SEPA unit. For this purpose, the membrane was segmented into circular sections, each 24 mm in diameter, to adapt to the CNF device's specifications. Hydraulic permeability and solute rejection were evaluated using specific solutions, with pressures ranging from 7.6 to 40 bar. The test solutions for the CNF device included lactose at 20 g/L, NaCl at 2 g/L, and $MgSO_4$ at 2 g/L. It should be noted that a pressure adjustment was necessary to account for the reduction in fluid volume caused by permeation.

For the secondary set, membranes cut from another region of the original sheet were tested to identify any variations in performance within the sheet. Identical tests, using the same solutions, were conducted, and the resulting data was compared with the results from the first membrane set.

Throughout these stages, particular attention was directed towards understanding the behavior of the membrane, analyzing solute rejection rates and permeate fluxes. The data collected provided valuable information into the CNF device's capabilities and highlighted areas ready for improvement, thus setting a solid foundation for future initiatives.

1.5 Thesis Outline

Chapter 2 delves into a detailed literature review, contextualizing the study within the scientific and industrial landscapes. In Chapter 3, the focus shifts to the methodologies employed, from the preparing the membrane and assembling the device, to the specifics of the experimental runs, thereby establishing a foundation for replicable research practices.

Chapter 4 presents a description of the experimental setup, results, and interpretation of the data collected from the SEPA unit, serving as a crucial reference for evaluating the CNF device's performance. The core of the research is developed in Chapter 5, where the CNF device's functionality is put to the test. This chapter initially focuses on the comparative analysis of the CNF device against the SEPA unit, and ends with the analysis of a second set of membranes.

Finally, Chapter 6 concludes the dissertation, bringing together the various stages of the research to reflect on the process from design to testing the CNF device. It considers the successes achieved, the lessons learned and suggests pathways for future research and development.

Lastly, the dissertation ends with Chapter 6, where conclusions are drawn. This chapter analyzes the various phases of the research, from design to testing the CNF device, highlighting the main accomplishments, while analyzing the challenges encountered and possible causes. Finally, considering the reached conclusions, the chapter presents suggestions for possible improvements to both the device's design and testing methodologies, in the hope that future research successfully achieves the proposed objectives.

Chapter 2

Membrane Filtration Background

Membrane filtration is a separation process that utilizes a membrane to separate components. This membrane can be defined as a selective barrier that separates two phases and restricts the permeation of specific chemical species [4].

As all separations processes, membrane filtration divides a feed stream into two streams: the permeate, depleted in species that the membrane rejects, and the concentrate, enriched in the same species [5]. This division can be seen in the figure below.

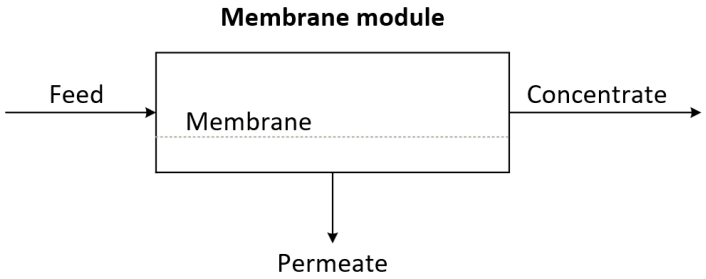

Figure 2.1: Schematic representation of a membrane process [5].

Both streams may be the desired product, depending on the goal of the separation. If the objective is to concentrate a solution, the concentrate stream is generally the desired product. However, if purification is the aim, either stream could be the product, depending on whether the unwanted impurities are retained or permeate the membrane [5].

The transport of selected components through the membrane occurs by applying a driving force across it (Figure 2.2).

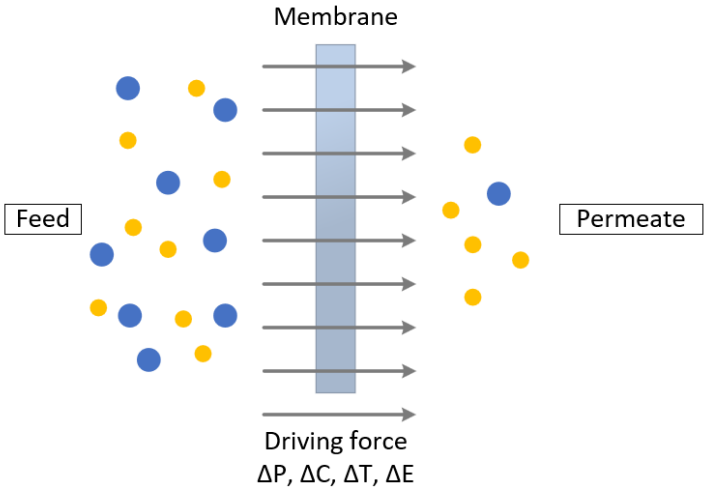

Figure 2.2: Schematic representation of a two phased system separated by a membrane (adapted from Mulder [5]).

The driving force responsible for movement through the membrane is determined by the gradient in the chemical potential (μ) of the component. This gradient is established due to variations in pressure, concentration, temperature or electrical potential between the two sides of the membrane. The flux (J) is expressed proportionally to the driving force by the following equation [6]:

$$J_i = -L_i \frac{d\mu_i}{dx} \tag{2.1}$$

where $d\mu/dx$ is the chemical potential gradient and L_i is a coefficient of proportionality.

While this work primarily focuses on filtration processes driven by pressure, particularly nanofiltration, Table 2.1 lists examples of processes driven by the other forces and their corresponding applications [7].

Table 2.1: Membrane processes with respective driving forces and applications.

Membrane process	**Driving force**	**Application**
Pervaporation	Concentration	Separation of mixtures of volatile liquids
Membrane Distillation	Temperature	Separation of water from non-volatile solutes
Electrodialysis	Electrical potential	Separation of ions from water and non-ionic solutes

2.1 Pressure-driven Membrane Processes

This study predominantly examines pressure-driven processes. These processes are characterized not only by the utilization of a pressure gradient as their driving force but also by the handling of solutions where the solvent is the continuous phase and solutes are present in comparatively low concentrations. Choosing the correct membrane depends on the solute particle size and chemical properties, which dictate specific pore size and distribution. The relationship between the solute and membrane structure determines the specific pressure-driven process to be used [5].

There are four main pressure-driven processes:

1. **Microfiltration (MF):** MF targets suspensions and emulsions with particle sizes ranging from 0.1 to 10 µm in diameter. The primary separation mechanism here is sieving. Since the membranes have high pore density and low hydrodynamic resistance, they don't require high operating pressures to generate high flux rates, usually operating at up to 2 bar [7].

2. **Ultrafiltration (UF):** UF separates macromolecular solutes, such as proteins and colloids. Just like MF, UF's separation mechanism is rooted in the concept of the molecular weight cut-off. Yet, it's not merely about weight; because of the smaller sized pores, the shape of a molecule can have significant implications on its ability to permeate the membrane. For instance, linear-shaped molecules might pass through pores of a specific diameter, while globular-shaped molecules of the same weight could be retained, as shown in Figure 2.3.

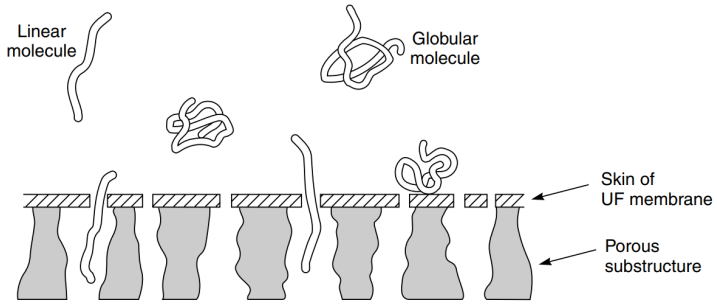

Figure 2.3: Schematic representation of linear molecules passing through the membrane and globular molecules of the same molecular weight being rejected [6].

When compared with microfiltration, UF shows two main distinctions. First, UF membranes have smaller pore diameters, typically ranging between 0.001 to 0.1 µm, which makes them able to retain smaller particles. Second, UF membranes have an asymmetric structure with a denser active layer. This results in higher hydrodynamic resistance, necessitating higher operational pressures, usually between 1 to 10 bar [5].

3. **Nanofiltration (NF):** Nanofiltration occupies a position between ultrafiltration and reverse osmosis in the spectrum of membrane filtration processes. NF membranes are effective in separating small organic molecules, such as glucose and sucrose, as well as certain inorganic salts. These membranes are particularly good at retaining divalent ions, such as Mg^{2+} and CO_2^{2-}, achieving rejections higher than 90% [7]. However, it becomes less selective at salt concentrations above 1000-2000 ppm in the feed water, hence, their primary application lies in purifying water that is relatively low in contaminants. Given its smaller pores ($<$ 2 nm in diameter), operational pressures generally range between 10 and 25 bar [6].

4. **Reverse Osmosis (RO):** Reverse osmosis is capable of extracting low molecular weight solutes from solutions, therefore widely used in desalination. Although sharing similarities with NF, the RO

membrane has a denser composition. This caracteristic makes it excelent at separating monovalent ions, achieving rejections for sodium chloride ions at rates often surpassing 98% [6]. This density also means a heightened resistance, requiring operational pressures ranging from 20 to 100 bar for adequate permeate flux [5].

RO operates in direct opposition to the natural phenomenon of osmosis. While osmosis sees water moving naturally from a less concentrated solution to a more concentrated one through a semi-permeable membrane, RO reverses this by applying hydrostatic pressure on the salt solution side, forcing water back towards the pure side and retaining the salts (see Figure 2.4).

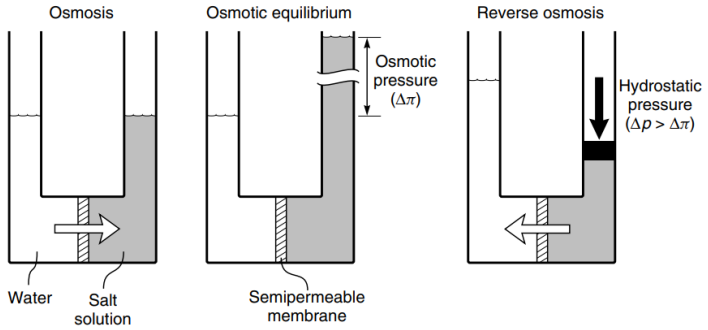

Figure 2.4: Osmotic effects across a semipermeable membrane [6].

While nanofiltration and reverse osmosis share many similarities, particularly in their primary use for water treatment, their distinct characteristics lead to varied applications. When selecting between NF and RO, the key considerations are the specific contaminants to be removed and the required level of retention (Table 2.2).

Table 2.2: Retention distinctions between nanofiltration (NF) and reverse osmosis (RO) [5].

Solute	**RO**	**NF**
Monovalent ions (Na, K, Cl, NO_3)	$>$98%	$<$50%
Bivalent ions (Ca, Mg, SO_4, CO_3)	$>$99%	$>$90%
Microsolutes (Mw $>$100)	$>$90%	$>$50%
Microsolutes (Mw $<$100)	0 - 99%	0 - 50%

For high rejection rates of monovalent ions like $NaCl$, RO is typically favored. On the other hand, for divalent ions such as Mg^{2+} and Ca^{2+} or microsolutes like sugars, and where high rejection of sodium chloride isn't essential, nanofiltration proves more suitable. NF not only effectively separates the previously mentioned salts, but is also more cost-effective due to its lower operational pressure demands for equivalent water flux compared to RO. It's also important to note that NF's selectivity diminishes with feed concentrations exceeding 2000 ppm, making RO a more viable option in such cases [5].

Table 2.3 provides a summary of the key distinctions among the four pressure-driven filtration processes discussed.

Table 2.3: Pore size, operating pressure, compounds removed and retain particles for RO, NF, UF and MF [5, 8].

	RO	**NF**	**UF**	**MF**
Pore Size (µm)	>0.0001	>0.001	>0.01	>0.1
Operating pressure (bar)	20 - 100	10 - 25	1 - 10	<2
Components removed	almost all dissolved compounds and suspended particles	polyvalent anions, cations, uncharged compounds, suspended particles	high molecular weight compounds and suspended particles	ideally only suspended particles are removed
Retain particulars (MW)	<350	>150	1000 - 300000	>300000

2.2 Types of Membranes

Membranes serve as crucial components in various filtration processes, and their classifications arise from their nature and morphology.

Regarding their nature, two primary types of membranes exist: biological and synthetic. Biological membranes, which can be further divided into living and non-living subtypes, are predominantly employed in fields such as medicine and biomedicine. Their composition is integral to processes that necessitate natural filtration mechanisms. On the other hand, synthetic membranes, which are the most widely used in industrial applications and this study's focal point, have broader subdivisions: organic and inorganic [5]. Organic membranes are typically polymeric or are in a liquid form. Common materials in this category include polyethylene, polypropylene, and polytetrafluorethylene [9]. These materials are particularly favored for pressure-driven processes, including microfiltration (MF), ultrafiltration (UL), nanofiltration (NF), and reverse osmosis (RO). In contrast, inorganic membranes enclude those made of metals and ceramics. Ceramic membranes, being inherently microporous, are preferred for MF and UL applications that demand solvent resistance and thermal stability [6]. Metal membranes, especially those made from palladium, have a niche use in separating hydrogen from various gas mixtures. This separation is achieved by the hydrogen's dissociative chemisorption onto the membrane's surface [10]. Another category within synthetic membranes is liquid membranes. Their primary application lies in carrier-facilitated transport processes, where a specific carrier molecule dissolved in the liquid dictates the separation efficiency by reacting with the substance to be separated, rather than the membrane's inherent properties [5, 6].

Moving from the nature to the structure, membranes can be isotropic or anisotropic, also known as symmetric or asymetric, respectively. Symmetric membranes are characterized by a consistent structure throughout their depth. The permeation rate, or the speed at which particles pass through these membranes, is inversely proportional to their thickness. Hence, thinner membranes generally allow for

a faster permeation rate [5]. Within this category, there are porous and non-porous types (Figure 2.5 – A and B). Porous symmetric membranes owe their filtration ability to their pores. The separation mechanism is largely physical. Particles larger than the biggest pores get blocked and are retained, while those smaller than the smallest pores can pass through freely. In this membranes the efficiency is at its peak when there's a significant difference in size between the particles to be separated. Conversely, non-porous symmetric membranes are dense, continuous films without distinct pores. They don't rely on pore size for separation. Instead, they separate molecules based on differences in solubility and diffusivity within the membrane material. Even molecules of similar sizes can be differentiated, making these membranes especially suited for applications like gas separation, pervaporation, and reverse osmosis. The selectivity is rooted in the membrane's material properties rather than physical sieving [6].

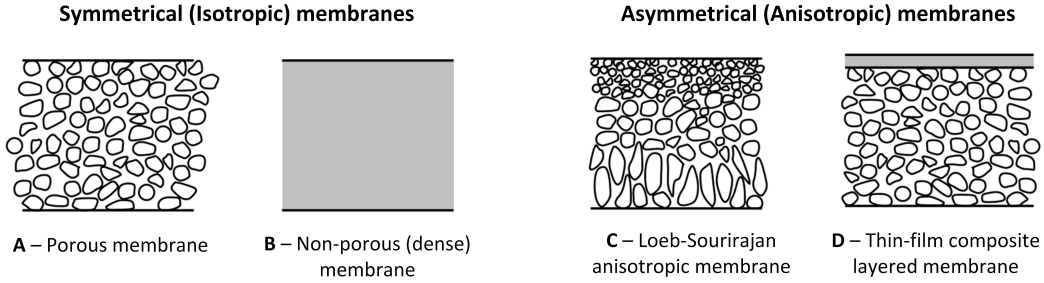

Figure 2.5: Types of membranes based on morphologic structure. Adapted from Baker.

As previously noted, the permeate flux and membrane thickness share an inverse relationship; hence, a thinner membrane is more cost-effective in filtration processes. However, producing a mechanically robust membrane with a thickness under 20 µm poses challenges [6]. This limitation gives rise to the significance of asymmetric or anisotropic membranes. These membranes are characterized by a thin, dense top layer, with thicknesses ranging between 0.1 to 0.5 µm [5], supported by a much thicker porous layer, as illustrated in Figure 2.5 - D. This design combines the dense membrane's selective advantages with the enhanced permeate flux of a thinner membrane. The thicker sublayer, while not significantly contributing to the separation process, acts as a crucial mechanical support for the delicate top layer. Figure 2.6 provides a detailed cross-sectional view of a thin-film asymmetric membrane, highlighting the distinct contrast between its layers. Some membranes, exemplified by the Loeb–Sourirajan type, achieve varied layers not by using different materials, but by presenting variations in porosity and pore size between layers (Figure 2.5 - C).

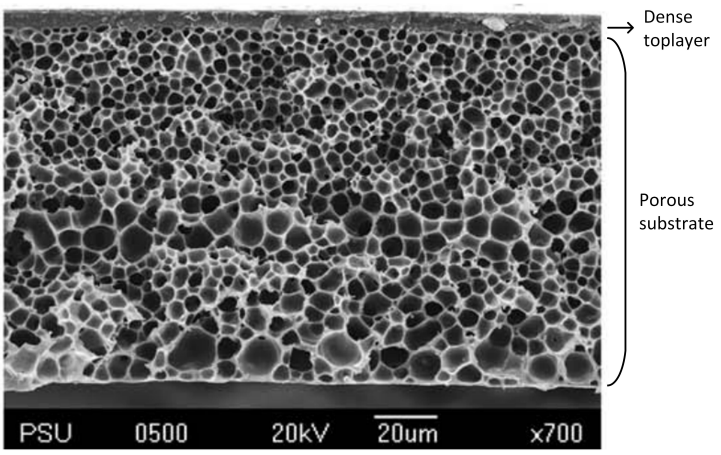

Figure 2.6: Cross-section of asymmetric membrane (image adapted from Yuenyao et al. [11])

2.3 Membrane Characterization

To evaluate a membrane's performance, two primary parameters are typically employed: rejection and hydraulic permeability.

The rejection coefficient measures the membrane's capability to separate the solute from the feed solution. Often denoted as observed rejection (R_obs), it's defined as [12]:

$$R_{obs} = \frac{C_f - C_p}{C_f} = 1 - \frac{C_p}{C_f} \tag{2.2}$$

Where C_p is the solute concentration in the permeate and C_f is the solute concentration in the feed solution. However, due to a phenomenon called concentration polarization, the solute concentration right at the membrane's surface, C_m, can sometimes exceed that in the bulk feed (C_f). In such cases, the real rejection coefficient is given as:

$$R_r = \frac{C_m - C_p}{C_m} = 1 - \frac{C_p}{C_m} \tag{2.3}$$

Turning our attention to hydraulic permeability, it represents the ability of a membrane to transfer water across it, providing insights into the relationship between the pure water flux and the transmembrane pressure. The water volumetric flux, represented as J_w, is given by the ratio of the volumetric water flow rate (Q_w) to the membrane area (A_m):

$$J_w = \frac{Q_w}{A_m} \tag{2.4}$$

This volumetric flux responds to changes in the transmembrane pressure gradient, Δp_m. A direct proportionality exists here: as the gradient Δp_m rises, so does the volumetric flux, a relationship captured by the hydraulic permeability (L_p) [5]:

$$J_w = L_p \cdot \Delta p_m = L_p \cdot (\Delta p - \Delta \pi) \tag{2.5}$$

If a membrane is permeable to a solute, the gradient is predominantly influenced by the pressure applied to the feed side of the membrane (Δp). The osmotic pressure difference ($\Delta \pi$) becomes negligible in this context. Consequently, the hydraulic permeability coefficient can be determined by conducting experiments with pure water at diverse feed pressures and subsequently plotting the resulting water flux against the applied pressure, as depicted in Figure 2.7, adapted from Mulder's work.

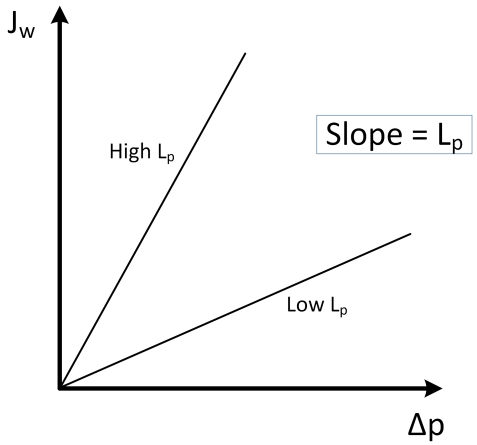

Figure 2.7: Water flux as a function of the applied pressure (adapted from Mulder [5]).

2.4 Membrane Transport Theory

The movement of permeate through a membrane primarily depends on the gradient of its chemical potential. This relationship between the chemical potential gradient and the flux is represented by the following equation:

$$J_i = -L_i \frac{d\mu_i}{dx} \tag{2.6}$$

Where $d\mu_i/dx$ is the chemical potential gradient for component i, and L_i acts as the coefficient of proportionality.

In processes like reverse osmosis, this chemical gradient arises from the differences in concentration (or activity) and pressure across the membrane. The corresponding chemical potential for such driving forces is expressed as [13]:

$$d\mu_i = RT \cdot \ln(\gamma_i c_i) + \upsilon_i \cdot d_p \tag{2.7}$$

Where c_i represents the molar concentration of component i, γ_i is the activity coefficient (with activity α_i defined as $\alpha_i = c_i \gamma_i$), υ_i is the molar volume and p is the pressure.

Given the unique characteristics of nanofiltration membranes, which fall between those of ultrafiltration and reverse osmosis, the mass transport through them is best described by two prominent models: the pore-flow model and the solution-diffusion model. These are visually represented in Figure 2.8.

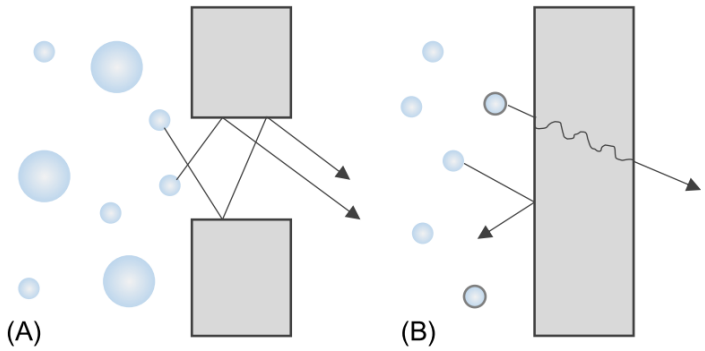

Figure 2.8: Schematic representation of mass transport through the membrane according to A) pore-flow model and B) solution-diffusion model [14].

A key difference between these two models lies in their interpretation of the chemical potential gradient. Specifically, the solution-diffusion model is based purely on a concentration gradient, while the pore-flow model emphasizes only a pressure gradient. The next sections provide a detailed description of these two models.

2.4.1 Solution-diffusion Model

The solution-diffusion model is applicable to dense, non-porous membranes, where salt separations stem from variations in the solubility and diffusivity of permeates through the membrane. This model is frequently utilized to predict the performance of membranes in Nanofiltration (NF) and Reverse Osmosis (RO) processes, given the dense nature of the membranes and the high pressures involved.

According to the solution-diffusion model, permeation occurs in several stages: solutes first partition into the membrane from the feed side, then diffuse through the membrane's bulk before finally partitioning into the permeate stream [12]. This separation stems from the varying solubility and diffusion rates of different species as they pass through the membrane. Figure 2.9 illustrates the evolution of chemical potential, pressure, and solvent activity gradients across the membrane as per the solution-diffusion model.

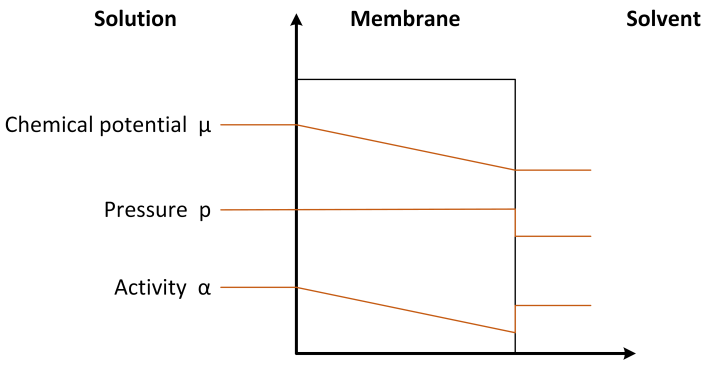

Figure 2.9: Schematic representation of chemical potential, pressure, and solvent activity gradients across the membrane, according to the solution-diffusion model [12].

A key assumption of the solution-diffusion model is that the pressure remains constant throughout the membrane, as can be observed in Figure 2.9. As such, the resultant chemical potential gradient is solely a function of the concentration gradient.

Permeate flux in this model is derived from Fick's law of diffusion, expressed as:

$$J_i = -D_i \frac{dC_i}{dx} \tag{2.8}$$

Where i represents a single permeating species and D_i represents its diffusion coefficient. The water volumetric flux (J_w) is therefore described by:

$$J_w = L_p \cdot (\Delta p - \Delta \pi) = \frac{K_w D_w^m}{\Delta x} \frac{V_w}{RT} (\Delta p - \Delta \pi) \tag{2.9}$$

With K_w being the water-membrane partition coefficient, D_w^m the water diffusion coefficient, V_w the molar volume of water and Δx the thickness of the membrane. From Equation 2.9, the water flux (J_w) directly and linearly correlates with the applied pressure, meaning as pressure increases, water permeation rises proportionately.

For the solute's flux permeating the membrane, it's assumed that the chemical potential gradient is purely a result of concentration differences, with pressure differences being negligible. The solute flux, thus, depends on its concentration and its permeability coefficient (B):

$$J_s = J_w \cdot C_p = B \cdot (C_m - C_p) = \frac{K_s D_s^m}{\Delta x} (C_m - C_p) \tag{2.10}$$

Where K_s is the solute-membrane partition coefficient and D_s^m is the solute diffusion coefficient.

From equations 2.3 and 2.10, the actual rejection for the solution-diffusion model, determined by the solute permeability coefficient (B) and water flux, can be deduced as:

$$R = \frac{J_w}{J_w + B} \tag{2.11}$$

This indicates that rejection raises with an increase in water flux. Given that B remains unaffected by pressure and the water flux is influenced by it, it's inferred that solute rejection increases with the pressure applied [12].

It's worth noting that, despite its widespread use in predicting the performance of NF and RO over the years, the solution-diffusion model does have recognized limitations. Wang et al. [12] has outlined several limitations of the solution-diffusion model. For instance, it is restricted to membranes with minimal water content and neglecting pore flow, and it is unable to accurately describe solute and solvent flux due to imperfections in the membrane barrier layer, pore flow, and solute-solvent-membrane interactions (which are not addressed by the model).

2.4.2 Pore-flow Model

The pore-flow model describes mass transport mechanisms specifically for microporous membranes. Such membranes are widely utilizaed in Microfiltration (MF) and Ultrafiltration (UF) processes. Contrary to the solution-diffusion model which focuses on diffusion-driven transport, the pore-flow model attributes solute rejection purely to size exclusion. In this model, there's no diffusion of solute species through the membrane.

A distinguishing feature of the pore-flow model is its assumption that solute concentration remains consistent across the membrane. As such, the chemical potential gradient is predominantly governed by a pressure gradient, rather than concentration differences [13]. This concept is represented in Figure 2.10.

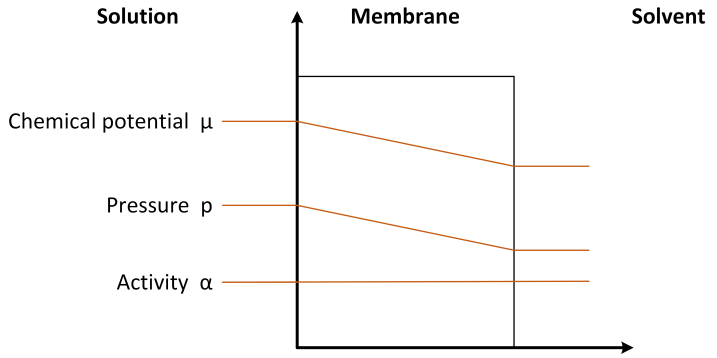

Figure 2.10: Schematic representation of chemical potential, pressure, and solvent activity gradients across the membrane, according to the pore-flow model [12].

A fundamental aspect of this model is its representation of the membrane as a collection of straight, cylindrical pores that span the full depth of its structure [12]. This is a simplification and might not represent the complexity of real-world membranes.

In this model, the fluid movement is described by Darcy's law. Thus:

$$J_w = \frac{A}{l} \cdot (p_f - p_p) \tag{2.12}$$

$$J_s = \frac{B}{l} \cdot (p_f^2 - p_p^2) \tag{2.13}$$

Where A is the water phase transport parameter, B is the solute phase transport parameter, p_f and p_p are, respectively, the pressures in the feed and permeate side of the membrane and l is the pore length.

While the pore-flow model offers valuable insights, it still presents some limitations. For instance, it overlooks the complexities brought about by pores of varying shapes and the influence of tortuosity on solute rejection. Thus, while it provides a basic understanding, relying solely on it to predict membrane performance could be an oversimplification [12].

2.5 Mass Transport Limitations

When choosing a membrane for a particular separation, it's essential to recognize that the membrane's active layer isn't the sole resistance encountered during the filtration process. In practice, multiple phenomena can impact mass transport, thereby influencing filtration performance. Two of the most significant challenges that arise during the actual filtration process are fouling and concentration polarization. These phenomena can introduce resistances that, if not adequately addressed, can adversely affect filtration efficiency and operational costs. This section will focus on these limitations, describing their implications and strategies employed to mitigate their effects.

2.5.1 Fouling

Membrane fouling represents one of the most significant challenges in membrane technologies, primarily because it leads to reduced filtration performance over time [15]. This phenomenon arises when suspended particles and dissolved compounds accumulate either on the membrane surface or within its pores. Such accumulation obstructs the regular flow of the solution through the membrane, consequently diminishing the permeate flux and reducing the membrane's rejection capabilities. Therefore, a higher operational pressure is necessitated to maintain expected performance, leading to increased energy consumption and reduced filtration efficiency.

Fouling is diverse in its nature and can be categorized based on its reversibility and the type of foulant. Reversible fouling occurs when particles form a 'cake layer' on the membrane that can be removed. This type of fouling can either be backwashable, where the fouling is removed by reversing the flow direction to lift off the deposited particles, or non-backwashable, where fouling isn't removed by backwashing but can be cleared chemically. On the contrary, irreversible fouling, primarily resulting from the blockage of membrane pores by colloidal suspensions and dissolved materials, resists both physical and chemical cleaning efforts [9].

Fouling is also categorized based on the type of substances causing the blockage. Inorganic fouling, often referred to as scaling, is caused by the deposition of inorganic salts on the membrane. Organic fouling, on the other hand, is attributed to the accumulation of organic compounds that lodge themselves on the membrane's surface and infiltrate its pores. Particle or colloidal fouling is another category, driven by various particles, whether organic, inorganic, or composite, that gather and stick to the membrane material over time. Lastly, the growth and attachment of microbial cells on the membrane surface, resulting in a biofilm layer, is known as biological or microbial fouling, commonly termed biofouling [9, 15].

Given the inherent nature of membrane processes, with their primary function being the exclusion of certain compounds, the occurrence of fouling is somewhat inevitable. However, the industry has explored several techniques to counteract its effects, including boundary layer control, turbulence inducers, membrane modification, and the implementation of combined external fields [16].

2.5.2 Concentration Polarization

Concentration polarization (CP) is a phenomenon inherent in all pressure-driven membrane filtration processes, characterized by an elevated concentration of specific components adjacent to the membrane surface compared to the bulk solution. This accumulation emerges as the permeate crosses the membrane, while the rejected solute accumulates near the membrane surface, generating a boundary layer with a solute concentration surpassing that of the feed solution [14]. Figure 2.11 illustrates the concentration profile associated with CP.

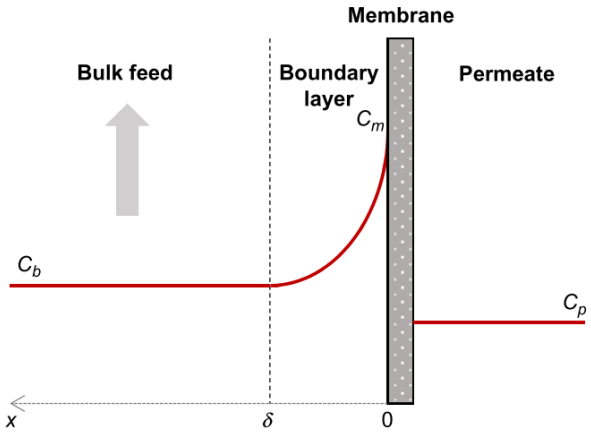

Figure 2.11: Concentration profile in membranes experiencing concentration polarization. (C_m – feed solution concentration at the membrane surface; C_b – bulk solution concentration; C_p – permeate concentration; δ – thickness of the boundary layer) [14].

CP doesn't merely disrupt the usual solvent movement, leading to a reduction in permeate flux. It can also compromise the membrane's separation efficiency. With a higher concentration at the membrane surface, the likelihood of solute molecules permeating the membrane can increase, potentially degrading the quality of the permeate.

Consequently, the membrane's efficacy and lifespan are critically impacted, inflating the costs of the filtration process. Additionally, the heightened concentration within this boundary layer can act as a precursor to fouling.

Various strategies have been adopted to mitigate concentration polarization in membrane processes, broadly categorized into four domains: membrane pretreatment, membrane modification, fluid management, and effective cleaning. In pressure-driven processes, the predominant methods to reduce CP are those under fluid management. These approaches primarily tweak the dynamics of fluid flow, promoting mixing between the feed solution and the boundary-layered solution. Examples of these methods include establishing turbulent flow regimes, implementing flow within curved channels, introducing vibrations to membrane modules, and employing pulsatile flow techniques [9].

This research focuses on centrifugal filtration, recognized for its efficacy in tempering the impact of concentration polarization. Centrifugal force propels heavier fluid elements away from the membrane surface, thereby introducing a natural self-cleaning mechanism [1].

2.6 Nanofiltration

Nanofiltration (NF) emerged in the 1980s as a pressure-driven membrane process, derived from the principles of reverse osmosis. These membranes typically feature pore sizes of about 1 nm and a molecular weight cut-off (MWCO) ranging from 300–500 Da [8].

As previously discussed, the attributes of nanofiltration membranes bridge the gap between porous ultrafiltration membranes, which primarily operate on size exclusion, and non-porous reverse osmosis membranes, where separation is steered by the solution-diffusion mechanism. A distinctive feature of NF membranes is the slight charge they carry due to the dissociation of groups, such as sulphonated or carboxyl acids, on their surface [17]. This charge significantly influences their exclusion properties, allowing them to exhibit high rejection rates for divalent ions such as calcium and magnesium, while offering lower rejection to monovalent ions like sodium. Additionally, they provide a more substantial flux in comparison to RO membranes. These distinguishing features have led to the adoption of NF membranes in specialized applications across various domains, including water and wastewater treatment, pharmaceuticals and biotechnology, and food engineering [18].

Over the years, NF membranes have garnered increased attention due to their notable advantages like simplicity, compactness, resilience, efficacy in impurity removal, alongside low energy and operational costs [19]. However, they are not without challenges, with fouling and concentration polarization being the predominant limitations.

Table 2.12 presents a selection of commercially available nanofiltration membranes, accompanied by their respective properties, as documented by Mohammad et al..

Membrane	Manufacturer	MWCO (Da)	Maximum temperature (°C)	pH range	Stabilized salt rejection (%)	Composition on top layer
NF270	Dow Filmtec[a]	200–400	45	2–11	>97%	Polyamide thin-film composite
NF200	Dow Filmtec[a]	200–400	45	3–10	50–65% $CaCl_2$ 3% $MgSO_4$ 5% Altrazine	Polyamide thin-film composite
NF90	Dow Filmtec[a]	200–400	45	3–10	85–95% NaCl >97% $CaCl_2$	Polyamide thin-film composite
TS80	TriSep[b]	150	45	2–11	99%	Polyamide
TS40	TriSep[b]	200	50	3–10	99%	Polypiperazineamide
XN45	TriSep[b]	500	45	2–11	95%	Polyamide
UTC20	Toray[c]	180	35	3–10	60%	Polypiperazineamide
TR60	Toray[c]	400	35	3–8	55%	Cross-linked polyamide composite
CK	GE Osmonics[d]	2000	30	5–6.5	94% $MgSO_4$	Cellulose acetate
DK	GE Osmonics[d]	200	50	3–9	98% $MgSO_4$	Polyamide
DL	GE Osmonics[d]	150–300	90	1–11	96% $MgSO_4$	Cross-linked aromatic polyamide
HL	GE Osmonics[d]	150–300	50	3–9	98% $MgSO_4$	Cross-linked aromatic polyamide
NFX	Synder[e]	150–300	50	3–10.5	99% $MgSO_4$ 40% NaCl	Proprietary polyamide thin-film composite
NFW	Synder[e]	300–500	50	3–10.5	97% $MgSO_4$40% 20% NaCl	Proprietary polyamide thin-film composite
NFG	Synder[e]	600–800	50	4–10	50% $MgSO_4$ 10% NaCl	Proprietary polyamide thin-film composite
TFC SR100	Koch[f]	200	50	4–10	>99%	Proprietary thin-film composite polyamide
SR3D	Koch[f]	200	50	4–10	>99%	Proprietary thin-film composite polyamide
SPIRAPRO	Koch[f]	200	50	3–10	99%	Proprietary thin-film composite polyamide
ESNA1	Nitto-Denko[g]	100–300	45	2–10	89%	Composite polyamide
NTR7450	Nitto–Denko[g]	600–800	40	2–14	50%	Sulfonated polyethersulfone

[a] Midland, Michigan, USA.
[b] Goleta, CA, USA.
[c] Tokyo, Japan.
[d] Le Mee sur Seine.
[e] Vacaville, CA, USA.
[f] Wilmington, Massachusetts, USA.
[g] Somicon AG, Basel, Switzerland.

Figure 2.12: Commercial nanofiltration membranes and their properties [18].

2.6.1 Nanofiltration Exclusion Mechanisms

Nanofiltration (NF) membranes utilize a unique rejection mechanism, which is an combination of various rejection methods. These include both sieving (size-based) and non-sieving processes, such as steric hindrance, electric exclusion (Donnan exclusion), dielectric effect, and the hydration mechanism. Each of these mechanisms will be described in the subsequent sections.

Sieving Mechanism - Steric Exclusion

Sieving functions as a size-discriminatory separation mechanism, where particles are sorted based on their dimensions. In essence, particles larger than a given pore are obstructed from passing through. This mechanism predominantly dictates the separation of neutral or uncharged solutes. Additionally, steric or size-based separation has been noted when the membrane filters ions whose hydrated ionic diameter surpasses the pore size [8, 18]. Figure 2.13 offers a visual representation of the size exclusion mechanism.

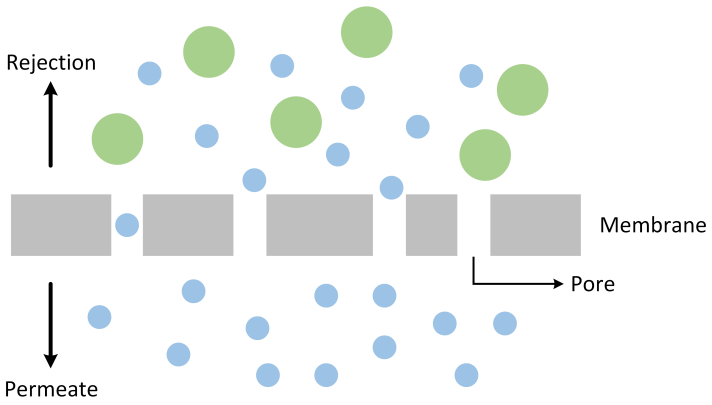

Figure 2.13: Schematic representation of the steric or size exclusion mechanism. (Adapted from Suhalim et al.).

When predicting rejection due to steric hindrance, solely relying on molecular weight doesn't provide a comprehensive understanding of the molecule's geometry. Therefore, it's essential to factor in other size-related parameters, including molecular length, Stokes radii, and average molecular size.

Solely relying on the sieving mechanism doesn't paint the full picture of rejection dynamics within NF membranes. It's evident that particles with a hydrated ionic diameter larger than the pore size predominantly face rejection due to the steric exclusion mechanism. However, particles with a smaller hydrated ionic diameter might also be rejected, an effect attributed to the membrane's surface charge. This charge plays a crucial role in the separation of ionic species. Consequently, to make accurate predictions regarding an NF membrane's rejection behavior, it's essential to consider both sieving and non-sieving mechanisms.

Non-sieving Mechanism

Non-sieving refers to a separation mechanism in which particles smaller than the membrane's pore size are captured by the membrane surface. As detailed by Suhalim et al., three primary rejection mechanisms are recognized: Donnan exclusion, dielectric exclusion, and the hydration mechanism. Figure 2.14 illustrates both sieving (steric exclusion) and non-sieving (Donnan exclusion and dielectric exclusion) mechanisms.

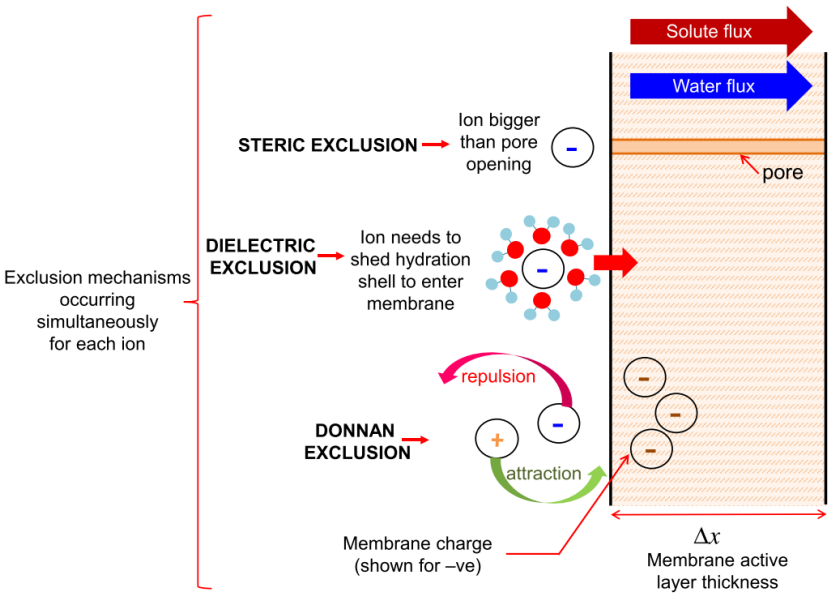

Figure 2.14: Schematic representation of solute exclusion mechanisms [20].

Donnan Exclusion

The Donnan effect pertains to the repulsion or attraction stemming from the electrostatic interactions between charged species and the charged membrane interface [18].

Figure 2.15 shows the Donnan effect in both negatively and positively charged membranes. As can be observed, positively charged membranes tend to reject negatively charged ions, allowing only positively charged ions through. Contrarily, negatively charged membranes repel positively charged ions, permitting the passage of negatively charged ions.

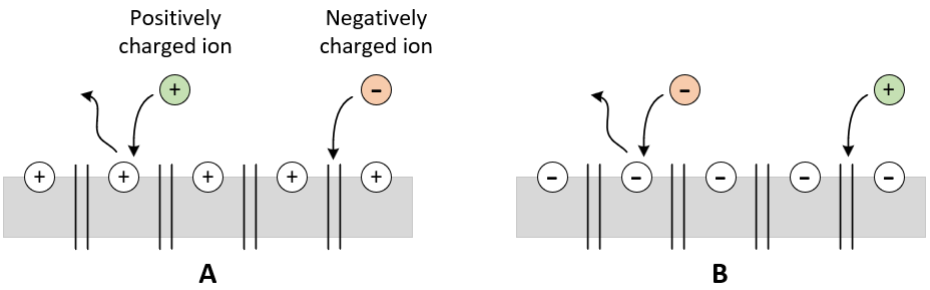

Figure 2.15: Schematic representation of Donnan effect. A) Positively charged membrane. B) Negatively charged membrane. Adapted from Suhalim et al..

The fundamental principle of Donnan exclusion suggests that salts with a higher charge of co-ions and a smaller charge of counter-ions experience increased rejection. Mohammad et al. conducted an experiment aligning with this principle. Using a negatively charged membrane, they examined the rejection behavior for three salt solutions: sodium chloride (NaCl), calcium chloride ($CaCl_2$), and sodium sulfate (Na_2SO_4). The findings revealed a rejection rate sequence of $Na_2SO_4 > NaCl > CaCl_2$. Notably, this order does not align with the size of the hydrated ions, indicating that size exclusion alone does not determine the rejection mechanism. Among the tested species, Na_2SO_4 faced the highest rejection, attributed to its highest charged co-ion (SO_4^{2-}), while $CaCl_2$ was least rejected due to its highly charged counter-ion (Ca^{2+}).

To predict the rejection behavior of NF membranes, the necessity for a model became apparent. Bowen et al. proposed the Donnan-Steric-Pore-Model (DSPM) in 1997, grounded on the Nernst-Planck equation, and encompassing both steric and Donnan exclusions. However, discrepancies arose when comparing DSPM predictions with experimental results, especially when using divalent cations (counter-ions) in the feed solution. Such inconsistencies suggest that for a comprehensive understanding and accurate prediction of NF membrane performance, other phenomena must be considered [8].

Concluding their extensive review of numerous studies on the NF membrane, Suhalim et al. determined the Donnan exclusion as the predominant non-sieving rejection mechanism.

Dielectric Exclusion

As mentioned before, it was identified that the Donnan exclusion alone might not fully capture the nuances of the non-sieving exclusion mechanism. This led to the introduction of dielectric exclusion. Yaroshchuk proposed that dielectric exclusion arises from the interaction of a hydrated ion with polarization charges it forms at the boundary of two mediums with distinct dielectric constants, the membrane matrix and the feed solvent within the pore. This interplay with the polarized boundary is responsible for what is termed the ”production of image forces”. This term is derived from a conceptualization of the interaction as if it were with an imaginary charge, positioned on the opposite side of the boundary at an equal distance from the real ion. If the solvent’s dielectric constant surpasses the membrane’s, then this image force repels both anions and cations. Figure 2.16 presents an illustration of this phenomenon.

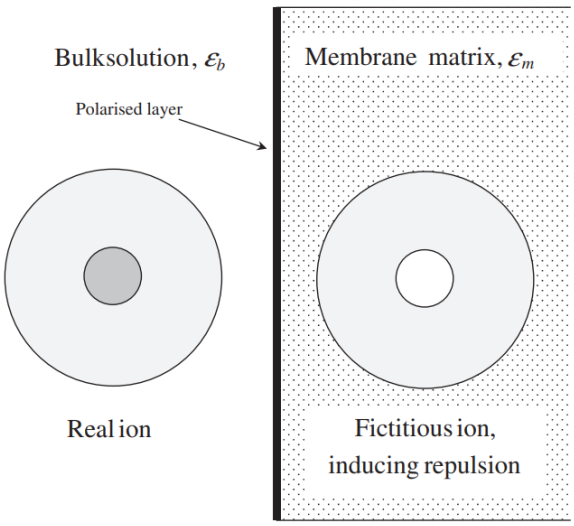

Figure 2.16: Schematic representation of how an ionic species nearing the NF membrane surface generates a repulsive image force [23].

Another theory explaining dielectric exclusion is known as the ”energy barrier” or ”Born effect.” This concept hinges on the notion that when a solvent is restricted within a atomic scale pore, typical of NF membranes, it interacts with the membrane's charge. This leads to a heightened spatial orientation of the solvent molecules, which subsequently impacts its physical and electrical attributes. This interaction diminishes the dielectric constant of the solvent. As an ion transitions from the bulk solution to the solvent in the pore, a shift in dielectric constant establishes a solvation energy barrier, which generates dielectric exclusion [23].

Bowen and Welfoot [17] integrated the dielectric effect into the DSPM, considering the Born effect. This integration not only brought down the charge density to a more realistic level but also enhanced the accuracy in predicting the behavior of NF membranes concerning divalent ions. The extended model was titled the Donnan-Steric-Pore Model with Dielectric Exclusion (DSPM-DE). Later, Szymczyk and Fievet presented the Steric, Electric, and Dielectric Exclusion model (SEDE), which included both the Born effect and the image force theory. However, it became apparent that the simultaneous consideration of both effects would lead to an amplification of the dielectric exclusion, resulting in inaccurate predictions [25].

Nowadays, the DSPM-DE remains the predominant model, given its reliable predictions in a majority of scenarios and the mathematical simplicity of the Born effect [25].

Dehydration Mechanism

Dehydration is a phenomenon intricately linked with dielectric exclusion. It occurs when a hydrated ion traverses an atomic-sized pore, resulting in the loss of some water molecules from its hydration shell [25].

Divalent ions possess a unique structure characterized by a dual-layer hydration shell surrounding the ions. The inner shell is dense and fixed, whereas the outer shell is more relaxed, with its water

molecules weakly bonded to the central ion. When the hydration radius surpasses the size of the pore, water molecules from the outer hydration layer are stripped away, allowing the compact inner layer to navigate through the pore. Upon passage, the outer shell replenishes its water molecules from the permeate zone, reverting to its initial configuration [8]. The phenomenon is illustrated in Figure 2.17.

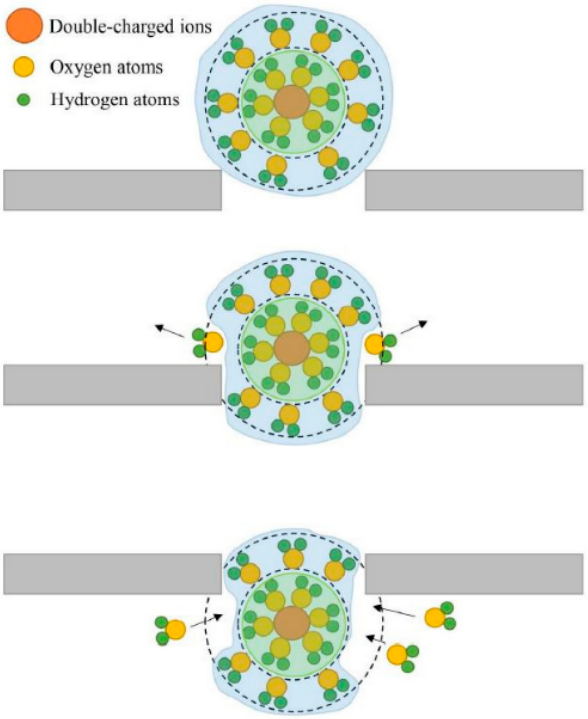

Figure 2.17: Schematic diagram of ions with hydration radius greater than the pore passing through [26].

Presently, the Born effect quantifies the energy consumption required for an ion to shed certain water molecules to facilitate its entry into the pore. However, this mechanism isn't expressly incorporated into the DSPM-DE model, which indicates potential for improving the accuracy of the DSPM-DE model [25].

2.7 Centrifugal Nanofiltration

The defining characteristic of centrifugal filtration is the rotation of the filtration device around an axis. This rotation creates pressure on the liquid through centrifugal force. Unlike traditional pressure-driven filtration, which requires high-pressure pumps to generate the necessary force, centrifugal filtration derives this high pressure from the spinning of the centrifuge rotor, eliminating the need for an external pump [27].

The centrifugal pressure is determined by taking into account a fluid element with mass m, which rotates around an axis at a distance r:

$$dp = \rho\omega^2 r \cdot dr \tag{2.14}$$

Given that the fluid mass is positioned between distances r_1 and r_2 relative to the rotation axis, the pressure difference can be determined by integrating Equation 2.14 across these radial positions:

$$\Delta p = \int_{r_1}^{r_2} dp = \int_{r_1}^{r_2} \rho\omega^2 r \cdot dr = \frac{1}{2}\rho\omega^2(r_2^2 - r_1^2) \tag{2.15}$$

Equation 2.15 is derived under the assumption that the fluid is incompressible (having a constant density ρ) and rotates around the axis at a steady angular velocity ω [1].

One of the notable successes of centrifugal filtration lies in its ability to counteract mass transport limitations like concentration polarization and fouling. This is largely attributed to its inherent self-cleaning mechanism propelled by the centrifugal and Coriolis forces. The centrifugal force, acting away from the rotation axis, is directly tied to the fluid's mass. This implies that denser fluid elements undergo a more pronounced centrifugal force. By positioning the membrane to face the rotation axis at a specific angle, fluid elements are pulled along the membrane in the direction of the centrifugal force. This movement results in the unique self-cleaning mechanism [1]. On the other hand, the Coriolis forces induce deviations in the fluid element's flow, fostering improved mixing [28]. When combined, these forces augment the filtration process's overall efficiency. Figure 2.18 illustrates the forces acting on a fluid element during rotation.

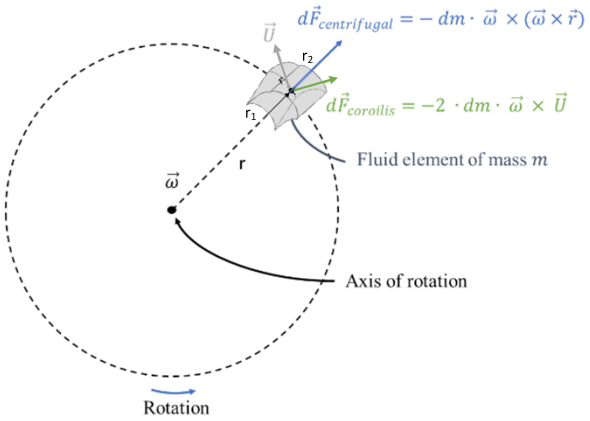

Figure 2.18: Top-down perspective of a fluid element rotating about an axis. The centrifugal force is represented by the blue vector, pointing radially outward from the rotation axis. The Coriolis force, shown by the green vector, is influenced by the fluid's velocity vector U, depicted by the grey vector. The direction of rotation and the fluid element's mass m are also highlighted. [2].

Centrifugal nanofiltration has proven beneficial in several sectors, especially where rapid filtration and minimal fouling are essential. For example, in the pharmaceutical industry, it aids in the efficient separation of nanoscale particles, ensuring product purity. Although it offers many benefits, centrifugal filtration also comes with its own set of challenges, including high initial equipment costs, the possibility of mechanical wear from constant rotation, and high energy consumption during its operation. This filtration process will be the one employed for the purposes of this research.

2.7.1 CNF Device

The centrifugal nanofiltration (CNF) device is an innovative solution in the field of nanofiltration, designed specifically to concentrate small volume samples of low molecular weight with heightened efficiency. The device studied in this research has seen several significant iterations, each aiming to advance its efficiency and adaptability. The prototype of the CNF device explored in this research traces its origins to the work of Completo et al. [1].

The goal of Completo et al. [1] was to create an innovative laboratory-scale CNF device that could concentrate small volume samples of low molecular weight more efficiently than traditional methods. This device, illustrated in Figure 2.19, was inspired by centrifugal filtration devices used for microfiltration and ultrafiltration. Crafted primarily from aluminum, its core components included a main body, a permeate chamber, and a membrane support part. A teflon internal block was essential to create a filtration chamber, situated between the membrane and the block's bottom surface, and a sample chamber on top. This block also creates two connecting channels, termed the neck and the auxiliary. An important design feature was the orientation of the membrane, which was angled in alignment with the centrifugal force, ensuring that the solution flowed tangentially across it.

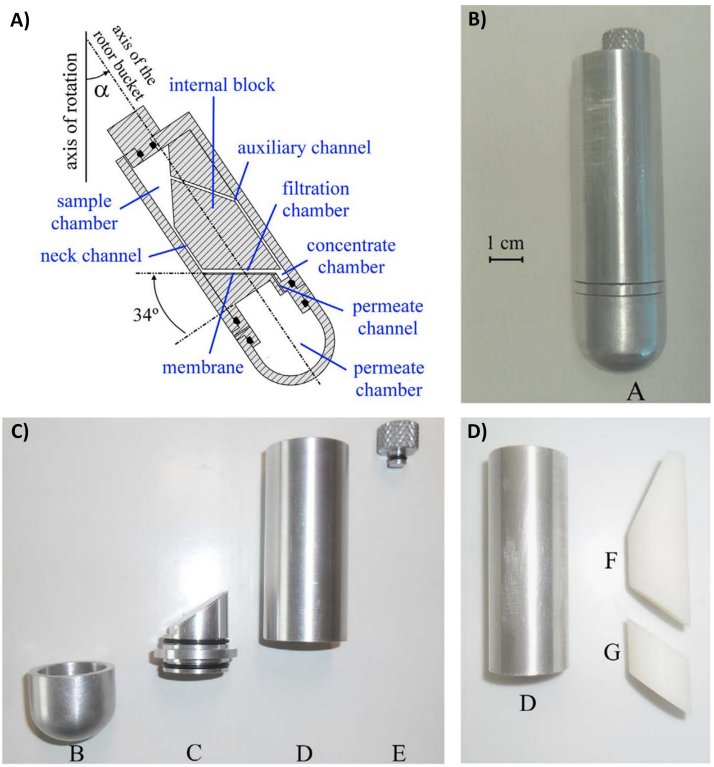

Figure 2.19: Detailed overview of the CNF device components developed by Completo et al.. A) Cross-sectional schematic highlighting the internal chambers and channels. B) Assembled CNF device. C) A deconstructed view of the CNF device showing the bottom part B, the membrane support part C, the top part D and the cap E. D) Internal block part F and small internal block part G, used to create the chambers and channels. [1]

Completo's prototype proved its efficiency, registering an impressive concentration factor (CF) of up to 23. However, the researchers also recognized that the device's design had room for improvements, particularly in facilitating the concentrate recovery process and in the effectiveness of the device sealing.

Building upon Completo's foundation, Hams attempted to adapt the CNF device for commercial scalability, prioritizing cost-effective production. To this end, Hams' version, depicted in Figure 2.20, featured a disposable design, exchanging aluminum for a combination of polycarbonate centrifugation tubes and 3D-printed polylactic acid (PLA) for the internal components. Silicone sealing was introduced to mitigate leakage issues.

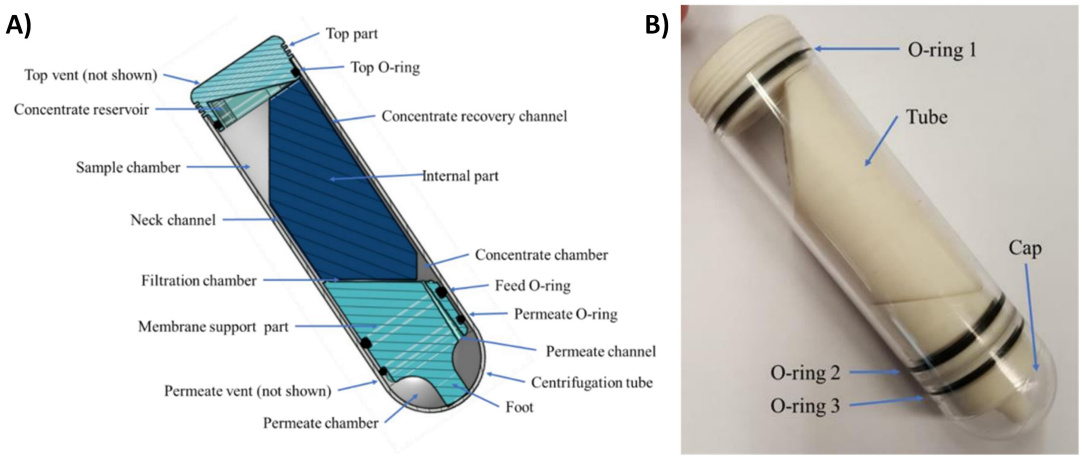

Figure 2.20: CNF device, by Hams. A) Cross-sectional schematic highlighting the internal chambers and channels. B) Assembled device. [2]

Though successful in sample concentration, Hams [2] iteration reached a maximum concentration factor of approximately 5. Two areas of potential improvement were identified: a more effective sealing technique to prevent permeate chamber leakage and the potential elevation of filtration pressure to achieve a higher CF.

Correia's [3] subsequent iteration aimed at design optimization. While achieving promising results, the issue of effective sealing remained an obstacle in the successful operation of the device. In light of these developments and challenges, the present research delves into further advancing the CNF device design, aspiring to overcome some of its limitations.

Given the history of the CNF device's development and the persistent challenges, this research sets out to further explore the design and functionality of the CNF device. Building on the solid foundations laid by Completo et al. [1], Hams [2], and Correia [3], this study will address some of the previously identified limitations.

Chapter 3

Materials and Methods

This chapter first presents the materials used in this research, then delves into the experimental testing, detailing the setup, equipment, and testing methodology employed. It describes the design and functioning of the Centrifuge Nanofiltration (CNF) device, highlighting its components and the process of membrane installation. The chapter also provides an overview of the methods used to determine experimental conditions in centrifugal filtration, specifically through the use of a Computational Fluid Dynamics (CFD) simulation. It concludes by discussing the analytic methods adopted to measure substance concentrations.

3.1 Materials

The nanofiltration membrane utilized in all experiments throughout this research was the NFS (TFC 100-250Da) - Sanitary NF Membrane, supplied by *Synder Filtration (California, USA)*. Detailed properties of this membrane can be found in Appendix A.1.

In this research several filtration experiments were conducted using various aqueous solutions. These solutions were prepared with three solutes: magnesium sulfate ($MgSO_4$) and lactose, both provided by *Merck (New Jersey, USA)*, as well as sodium chloride (NaCl) supplied by *PanReac (Barcelona, Spain)*. Deionized water served as the solvent for all the solutions prepared.

To ensure the membrane's longevity and prevent biofilm formation, it was conserved using a 1% potassium metabisulfite ($K_2S_2O_5$) solution from *SAI* whenever it remained unused for more than two consecutive days.

3.2 Methods

3.2.1 SEPA

The initial phase of this research was to characterize the nanofiltration membrane. For this purpose, preliminary experiments, mirroring those to be executed later in the CNF device, were conducted in a

SEPA CF Cell by *Sterlitech Corporation (Washington, USA)*. This is a crossflow filtration unit designed for laboratory-scale experiments to assess the efficacy of flat sheet membranes [29], with a membrane active area of 140 cm^2 (additional details available in Appendix A.2). The components of the SEPA cell include a stainless steel body (consisting of a top and a bottom section), an anodized aluminum cell holder complemented by a high-pressure gauge, a feed spacer, a concentrate control valve equipped with another high-pressure gauge, and a pair of o-rings. Alongside the primary unit, auxiliary equipment such as a feed tank and pump are required for the experiment.

The assembly procedure starts by positioning a pre-cut membrane into the bottom section of the cell body (shown in Figure 3.1 - C), identifiable by its four alignment pins. This section is where the membrane is fixed, with its active side facing down because the concentrate feed inlet is located at the bottom of cell's body. As shown in Figure 3.1 - B, the feed spacer is first placed in the chamber, followed by the membrane. Following this, the top section of the cell is fitted onto the bottom, via the alignment pins. The entire assembly process is illustrated in Figure 3.1.

Once the cell body is assembled, it's then inserted within the cell holder. This will later be pressurized via a hydraulic hand pump supplied by *ENERPAC (Wisconsin, USA)* to ensure that the cell body is completely sealed. The holder incorporates a pressure gauge (Figure 3.1 - D), which facilitates real-time pressure monitoring. It's essential that the exerted pressure doesn't surpass maximum limit recommended by the manufacturer (69 bar).

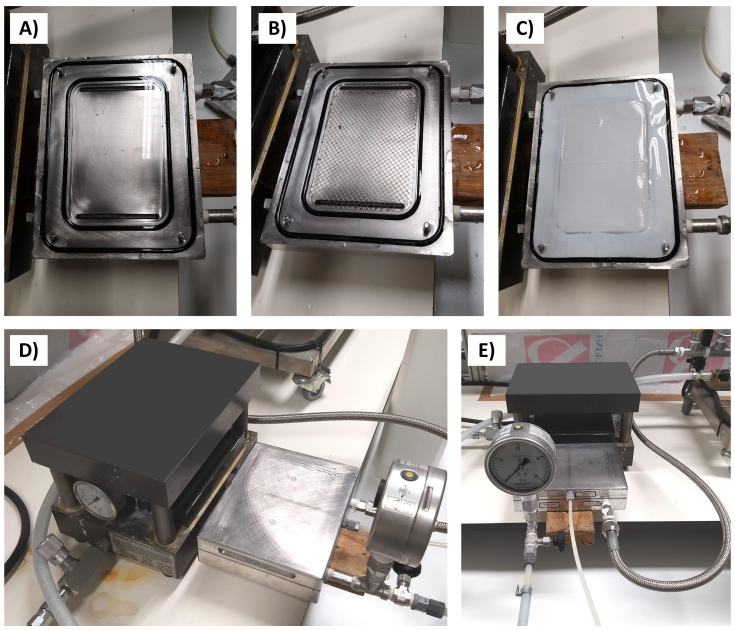

Figure 3.1: Assembly of the SEPA CF Cell unit. A) Empty cell chamber. B) Cell chamber with a mesh spacer. C) Cell chamber with a membrane in place. D) Overview of the SEPA nanofiltration cell. E) Side view highlighting the nanofiltration cell's connection points and pressure gauge.

The SEPA unit releases two different streams: the concentrate stream, which retains the solution's components, and the permeate stream, which is the solution that has successfully permeated the membrane. The concentrate stream's outlet is located at the cell body's base and its flow is controlled via

a flow control valve and a pressure gauge. The operational pressure is adjusted by manipulating the control valve and it can be read on the pressure gauge. This stream is then redirected to the feed tank for reuse. The feed tank used can hold up to two liters and is kept cool by a circulating water stream.

As for the permeate stream, it passes through the membrane and exits the unit from the top section of the cell body. A simplified diagram of the SEPA unit's operating circuit can be observed in Figure 3.2.

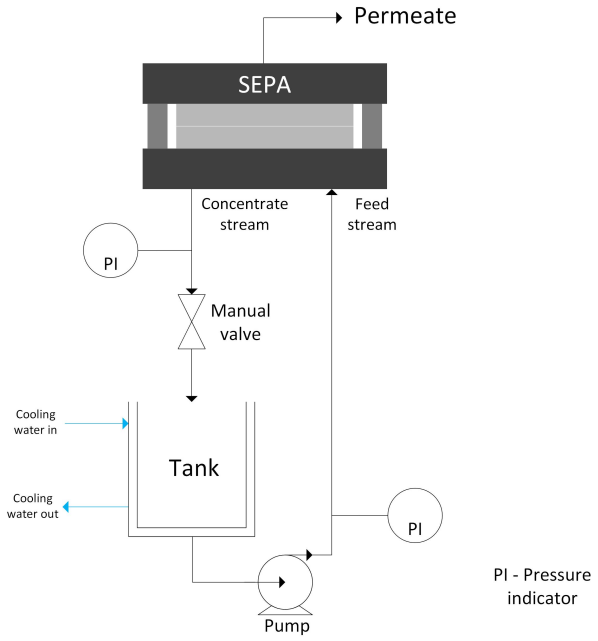

Figure 3.2: Schematic diagram of the SEPA crossflow filtration system showing the flow path of feed stream, concentrate stream, and permeate, along with the associated equipment and control elements.

To control the feed stream flow, a plunger pump (3CP1221 model by *Cat Pumps*) coupled with a three-phase electric motor by *MEB Maquinaria Eléctrica Bilbao (Bilbao, Spain)* was used. The pump outlet stream has a pressure gauge incorporated, which should consistently mirror the pressure read in the concentrate stream. A variable-frequency drive (VFD) is employed to manipulate the motor's speed by adjusting the frequency of its power input [30]. As such, the selected frequency on this device directly impacts the motor's speed, and consequently, the feed flow rate. To determine the exact frequency corresponding to the desired flow rate, a calibration curve was derived by measuring flow rates at various frequencies (5, 10, 15, and 20 Hz) using a timer and a graduated cylinder. Plotting these measured flow rates against their specific frequencies and applying linear regression generated the calibration line (see Appendix A.3).

Figure 3.3 presents the fully assembled setup.

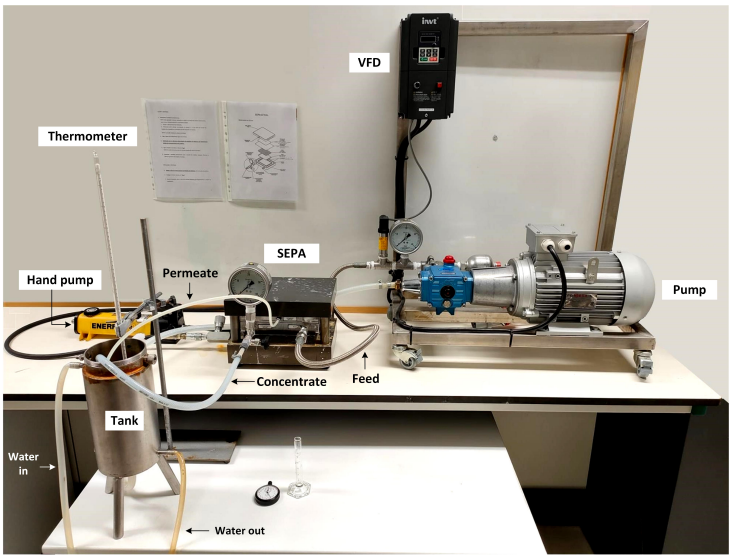

Figure 3.3: Laboratory setup showcasing the SEPA filtration system, equipped with various components including a variable-frequency drive (VFD), plunger pump, hand pump, tank for feed solution, and instrumentation like the thermometer and pressure gauges.

Each experiment started with two liters of the solution being prepared and loaded into the feed tank. This volume of solution ensures that even after accounting for dead volume and permeate, there's no risk of the tank running dry, which would introduce air into the system and potentially damage it.

After each experiment, it's important to rigorously clean the membrane. This is achieved by cycling several liters of deionized water through the SEPA unit in an open circuit until the permeate flux returns to its original value and the concentrate stream's conductivity matches that of pure water (1-3 µS/cm).

While the unit is not in operation, the residual water within the chamber maintains the membrane's moisture, preserving it. However, if the membrane remains unused for over two consecutive days, it is preserved in a 1% potassium metabisulfite ($K_2S_2O_5$) solution to prevent biofilm formation and prolongue its longevity.

3.2.2 CNF Device

Device Design and Prototyping

The design of the CNF device is essential to achieve the functionality and efficiency desired. This section describes its components and unique design features.

The device studied in this thesis has a simpler design than the previous iterations, consisting of just two chambers: one for the concentrate and another for the permeate. One of its significant innovations is the sealing mechanism for the membrane. Unlike previous designs that relied on glue, this design ensures secure membrane placement without the need for adhesives. Another distinctive characteristic of this device is the membrane's orientation relative to the centrifugal force. Instead of a parallel placement that allows tangential flow, the membrane is tilted at an angle of 34.0°. This innovation aims to simplify the sealing mechanism without compromising the membrane's self-cleaning capability.

The device is composed of two primary parts: a cylindrical body and a lid. Both are 3D printed using acrylonitrile butadiene styrene (ABS) on an Ultimaker 2+ printer from *Ultimaker (Utrecht, Netherlands)*. The computer-aided design (CAD) was created using *Onshape*, an online software, and was then converted into a Standard Triangle Language (STL) file. This file was processed using *Cura*, a slicing software that translates the design into printable layers. The *Onshape* model and the final printed device are presented in Figure 3.4.

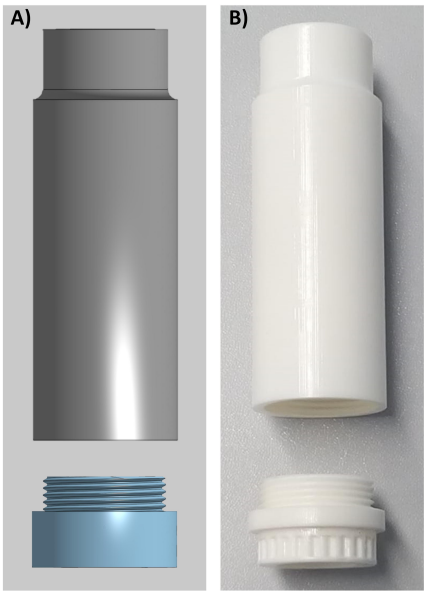

Figure 3.4: Design of the cylindrical body and lid as seen in the *Onshape* CAD (A) and after 3D printing (B).

Given that the design must be compatible with the SS-34 high-speed rotor used for the experiments, it must match the specific rotor's tube dimensions, measuring 29 mm in diameter and 108 mm in length. Observing the cross-sectional view of the design (seen in Figure 3.5), the body is primarily a hollow cylinder with an indentation serving as a support for the membrane. An o-ring is positioned in this indentation, which completely seals the membrane and ensures that all the permeate collected crossed the membrane. The cavity within the tube forms the concentrate chamber.

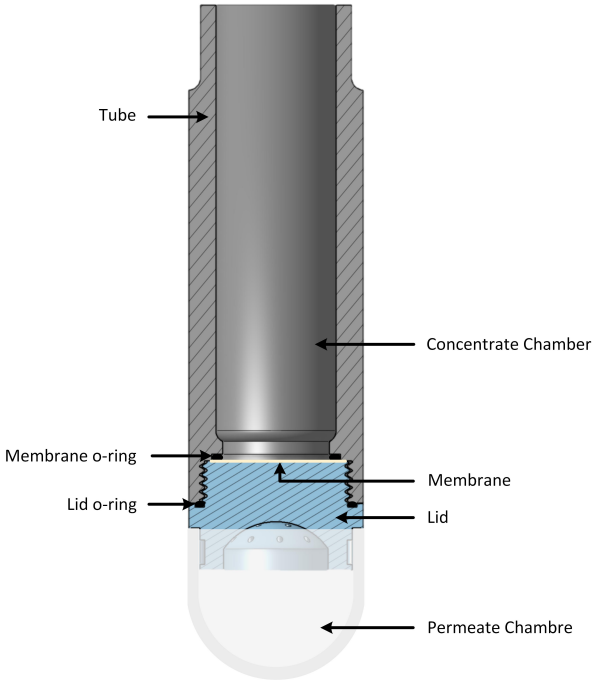

Figure 3.5: Cross-section schematic representation of the CNF device.

The lid screws onto the body over the membrane, sealing it in place. This innovative sealing mechanism eliminates the necessity for adhesives like glue to hold the membrane, which proved to be an issue in past studies.

The perforations in the lid guide the liquid crossing the membrane into the permeate chamber. Another o-ring is placed within the lid's screw mechanism to ensure a leak-proof seal. Figure 3.6 shows the described attachment mechanisms and the positioning of both o-rings, along with the respective CAD.

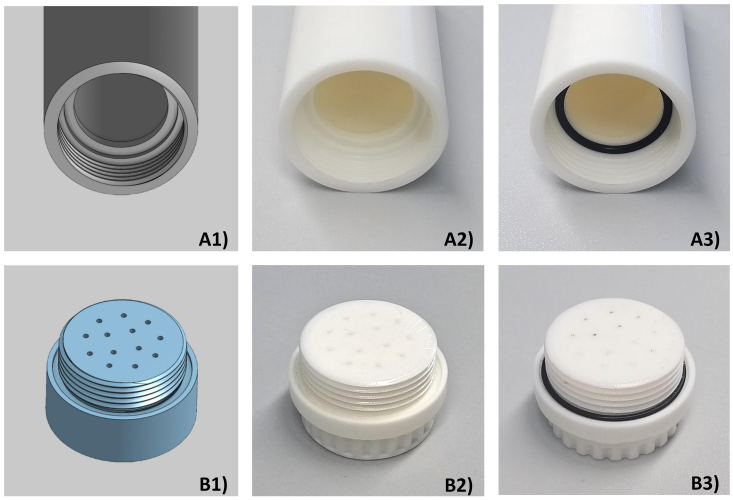

Figure 3.6: Attachment mechanisms of the lid (B) and cylindrical body (A) with (A2 and B2) and without (A3 and B3) the o-ring, along with the respective CAD (A1 and B1).

After the filtration, the permeate is collected in a polycarbonate cap fitted into the device's lid. This cap, functioning as the permeate chamber, is created by cutting about 3 cm from a Nalgene™

High-Speed Polycarbonate Round Bottom Centrifuge Tube by *Thermo Scientific (Massachusetts, USA)*. These standard centrifuge tubes are tailored to fit the high-speed rotor in use.

When assembled, the individual components (Figure 3.7 - A) form the finalized device set for experimental operation, shown in Figure 3.7 - B.

Figure 3.7: A) Disassembled components of the CNF device: cylindrical body, screw-on lid, and permeate chamber. B) Fully assembled CNF device, showing how the individual components integrate.

The membranes required for the device were cut from the original membrane sheet into circles, each with approximately 24 mm in diameter. While the membrane active area in the device measures 2.4 cm^2 (17.4 mm diameter), the extra millimeters ensure an adequate margin for the o-ring grip. The membrane is positioned within the tube with its active side facing the concentrate chamber, so that it comes into direct contact with the concentrate. Figure 3.8 illustrates the membrane's internal placement and external appearance.

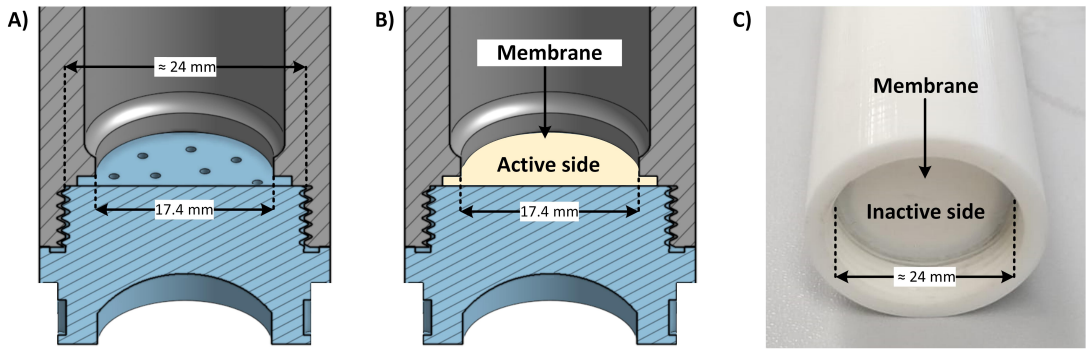

Figure 3.8: A) & B) Cross-sectional schematics of the CNF device, emphasizing membrane positioning. C) The 3D printed body with the membrane installed.

In summary, the redesigned CNF device integrates innovative features such as a new sealing mechanism and the membrane orientation, with the goal of optimizing its performance while eliminating past challenges.

Experimental Setup

To study the performance and capabilities of the CNF device, a rigorous experimental setup was used. This section describes the experimental procedure utilized to test the CNF device, including equipment, setup, and operational parameters.

All testing was performed in a Sorvall™ RC 6 Plus Centrifuge by *Thermo Scientific* (Figure 3.10 - A), a superspeed centrifuge that allows for high-pressure centrifugal filtration. It is paired with a SS-34 Fixed Angle Rotor by *Thermo Scientific* (Figure 3.10 - B), for which the device's design has been developed. The rotor has a characteristic angle of 34.0° and eight buckets, enabling testing of eight devices simultaneously. The maximum speed this combination allows is 20000 rpm. With the equipment ready, the next phase involves preparing the CNF device for the testing.

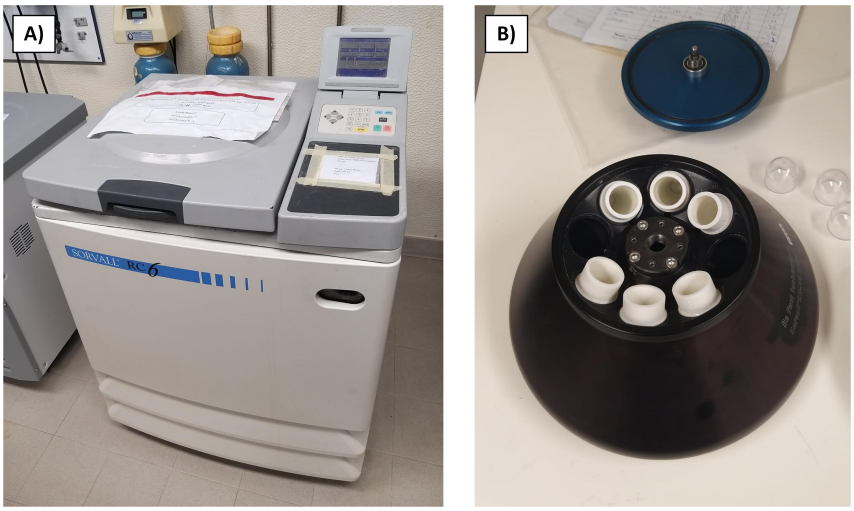

Figure 3.9: A) Sorvall™ RC 6 Plus Centrifuge, by *Thermo Scientific*. B) SS-34 Fixed Angle Rotor, by *Thermo Scientific*.

To prepare the device for testing, the membrane is properly installed and the solution is loaded inside the tube, in direct contact the active side of the membrane. Before starting the experiment, the eight devices must be weighed to ensure counterbalancing, which is crucial for the rotor to be balanced. The difference in weight of each pair of devices, positioned on opposite sides of the rotor, must not exceed 0.3 g. Figure 3.10 provides a visual representation of the device's placement inside the rotor, including the position the solution takes inside the device before the test begins.

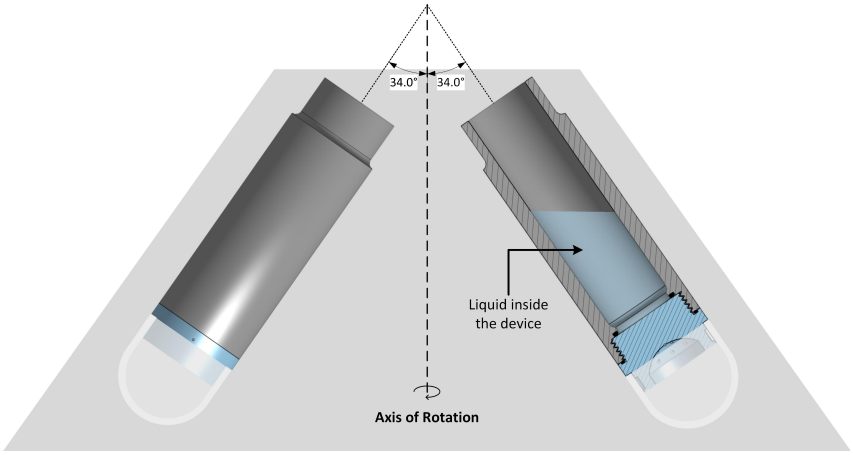

Figure 3.10: Schematic representation of the device inside the rotor and the solution within the device before centrifugation. The gray trapezoid represents the rotor.

After securely attaching the rotor to the centrifuge, the next step is to configure the desired operational settings. These settings include selecting the rotor type, rotational speed, duration, acceleration and deceleration rates, and test temperature. All experimental tests utilized the SS-34 rotor, operated at 20℃, and were set with acceleration and deceleration rates of 7 and 8, respectively.

The pressure exerted during a test is dictated by the selected rotational speed, which varies for each test. A fluid dynamics simulation, discussed in subsequent sections, established the relationship between rotational speed and pressure applied on the membrane.

Centrifugation duration is adjusted based on the chosen speed, whith the aim being to achieve a consistent permeate volume across all tests. As such, higher-speed tests, which result in increased membrane pressure, need shorter centrifugation periods to achieve the desired permeate volume compared to tests conducted at lower speed.

It's important to note that the actual time used to calculate permeate flux isn't the direct setting from the centrifuge. Instead, the effective time begins when the centrifuge hits 80% of the target speed during acceleration and ends when it decelerates to the same 80% speed. The goal of this approach is to exclude the acceleration and deceleration phases. Following several tests, it was determined that the combined acceleration and deceleration durations consistently total approximately one minute. Thus, when analyzing results, the experiment duration is adjusted by subtracting this one minute.

In conclusion, this experimental setup offers a standardized, accurate testing environment for the CNF device. The procedures adopted ensure consistent results across a plethora of testing parameters.

3.2.3 Simulation of experimental conditions

The pressure experienced inside the device is defined by both the volume of the feed solution and the centrifuge speed. Thus, to accurately set the centrifuge speed so that the experiment operates at a specific pressure, it's crucial to establish a correlation between these two parameters. To achieve this, we employed Computational Fluid Dynamics (CFD) via the *simFlow* software. Through this simulation, we can predict the how fluid will behave inside the device under various centrifugation speeds.

Geometry

To simulate the fluid dynamics during centrifugation, it was firstly necessary to create a Computer Aided Design (CAD) representation of the liquid volume inside the device. This CAD model defines the maximum possible volume of liquid the device can hold when in operation. As illustrated in Figure 3.11, this volume is determined according with the device's position inside the rotor (at an angle of 34.0°) and the impact of centrifugal force, which pushes the liquid in the direction opposite to the axis of rotation.

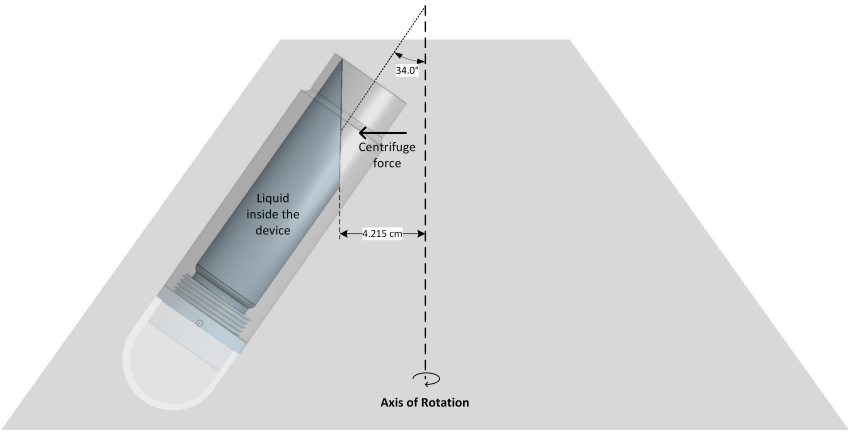

Figure 3.11: A detailed schematic illustrating the orientation and positioning of the liquid inside the device during centrifugation. The angle of 34.0° represents the device's placement within the rotor, while the centrifuge force acts on the liquid in a direction opposite to the axis of rotation. The gray trapezoid represents the rotor.

This CAD design was subsequently converted into an STL (Stereolithography) file format, a digital file type used to represent three-dimensional geometries. It was then uploaded to *simFlow*, a Computational Fluid Dynamics (CFD) software, to construct the simulation. However, the uploaded geometry wasn't positioned as shown in Figure 3.11. Therefore, prior to starting the simulation, the model was adjusted by tilting it 34.0° and translating it to maintain a distance of 4.215 cm from the z-axis (the gap between the rotor's axis and the furthest side of the bucket). Figure 3.12 illustrates the geometry used for the simulation, shown in two different views.

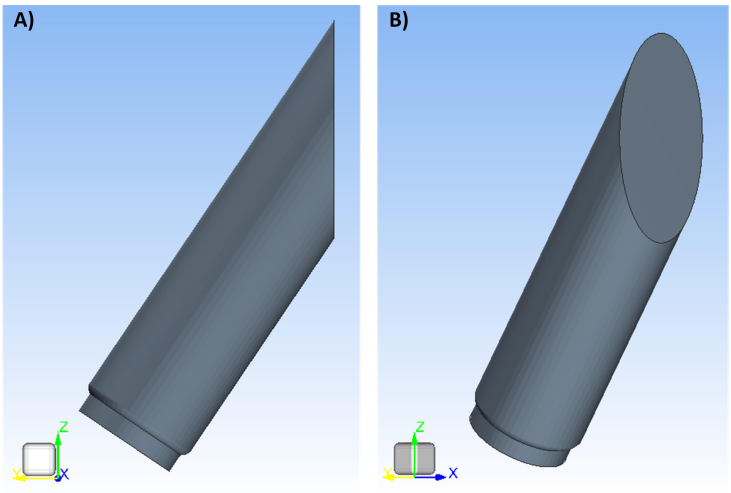

Figure 3.12: Fluid geometry used for the *simFlow* simulation in two different views (A and B).

Mesh

Meshing plays an essential role in Computational Fluid Dynamics (CFD). It involves the subdivision of the geometric model into smaller, manageable pieces known as elements or cells. This gridwork not only reflects the physical form of the fluid being studied but also serves as the base upon which the equations of the fluid flow are solved.

A finer mesh can lead to enhanced precision in results, but it also increases the computational load, which largely increases the processing time. So, when creating a mesh, it is important to find an optimal balance between mesh resolution and computational efficiency.

Figure 3.13 shows the mesh used in this simulation. The fluid surface was defined as the inlet (shown in red in Figure 3.13 - B), while the interface with the membrane served as the outlet (highlighted in yellow in Figure 3.13 - C). The other faces were categorized as walls. In an effort to improve the mesh resolution near these walls, five boundary layers were incorporated. These layers were set with an expansion rate of 1.25 and a first layer thickness of 0.2.

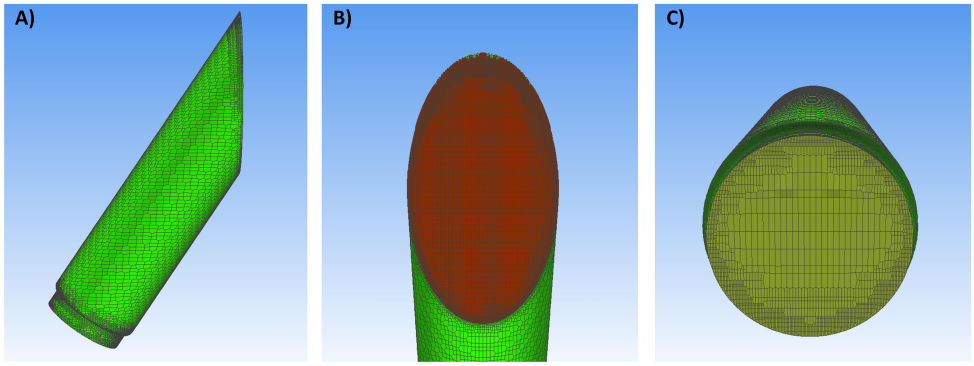

Figure 3.13: Mesh developed in *simFlow*. The inlet is indicated by the red plane (B), the outlet by the yellow plane (C), and the remaining green faces are defined as walls (A).

Setup simulation data

Now that the mesh is created, the focus moves to setting up the simulation, beginning with the solver selection. A solver is a set of predefined models that can be used to simulate the behavior of the fluid under specific conditions. For this simulation, the SRF PIMPLE (Single Rotation Frame) solver was chosen, given that it is the most suitable for modeling a rotating flow within a singular rotation domain [31].

The key inputs for this solver include the reference point, the axis of rotation, and the angular velocity (measured in revolutions-per-minute or rpm). For this simulation, the origin is the reference point, with the z-axis serving as the rotation axis.

After ensuring the simulation has run enough time to stabilize, post-processing was carried out using the *ParaView* software. *ParaView* is a data analysis tool offering interactive 3D visualizations. This tool allows the visualization of pressure fluctuations within the device.

The simulation was executed across various velocities, ranging from 3000 to 16000 rpm. Each velocity was individually analyzed, allowing to build a correlation between the centrifugal speed set in the centrifuge and the internal device pressure.

3.2.4 Analytic methods

In the context of this study, specific techniques and equipment were chosen to determine concentrations of the chosen substances. This section describes the analytical methods adopted to evaluate salt and lactose concentrations, detailing the instrumentation, calibration procedures, and calculation approaches.

Salt concentrations, namely sodium chloride and magnesium sulfate, were determined by measuring their conductivity. A *Crison (Barcelona, Spain)* GLP 31 electrical conductometer was utilized for this purpose. The conductivity measurements were then converted into salt concentrations using calibration curves, one specific to each salt. The calibration curves were determined by measuring the conductivity of both salts across a range of known concentrations. These values were then plotted against their corresponding concentrations, and a calibration curve was derived using linear regression. Details for these calibration curves can be found in Appendices A.4.2 and A.4.1.

The conductivity measured by the device is referenced to 25ºC, which means that it automatically corrects the conductivity value according to the following equation [32]:

$$\kappa_{25} = \frac{\kappa_\theta}{(1 + \alpha_{\theta,25}/100)(\theta - 25)} \tag{3.1}$$

Where k_T and k_{25} are the conductivities measured at temperatures T and 25ºC, respectively, and $\alpha_{\theta,25}$ is the temperature coefficient of variation.

Most conductivity measurements were performed keeping the solutions at 25ºC while measuring, so there was no need to correct the conductivity value. However, a small number of measurements were performed at room temperature, and for those a temperature coefficient of variation of 1.95% was used, calculated via Equation 3.1.

Lactose concentration was measured by high-performance liquid chromatography (HPLC). The resulting chromatograms were processed using *Origin* software. By assessing the peak area in a chromatogram, lactose concentration was derived in similar manner to the salts, that is, by converting peak area to concentration using a calibration line found in Appendix A.4.3.

All weighing was performed using a *Sartorius* analytical scale, model Basic and a *COBOS precision* technical scale, model CB-Junior.

Chapter 4

SEPA

4.1 Introduction

As previously noted, the first step is to characterize the membrane under study, so that it is possible to validate the results obtained from the CNF device in subsquent testing. To this end, multiple filtrations were performed in the SEPA unit using three distinct solutes: sodium chloride, magnesium sulfate, and lactose. For each of these filtrations, the permeate flux and concentration were measured, enabling us to determine both the hydraulic permeability and solute rejection.

Membrane Preparation and Installation

The membrane employed in the SEPA unit was extracted from a nanofiltration membrane sheet (NFS TFC 100-250Da) measuring approximately 93 cm by 34 cm. To fit the installation, a rectangle measuring 19.3 cm by 14.2 cm was cut out and perforated at the corners to enable fixation in the SEPA unit (Figure 4.1 - B). To prevent any leakage, it was crucial to ensure the membrane's perimeter fit between the inner and outer o-rings, as shown in Figure 4.1 - C.

Figure 4.1 - A provides a scaled representation of the membrane sheet, highlighting the specific area from which the membrane sample was extracted. Recognizing the exact origin of the membrane section is essential since one of the objectives of this research is to evaluate potential variability in membrane characteristics within the same sheet. After the extraction, the membrane was installed in the SEPA unit following the setup procedures described in Chapter 3 - Materials and Methods.

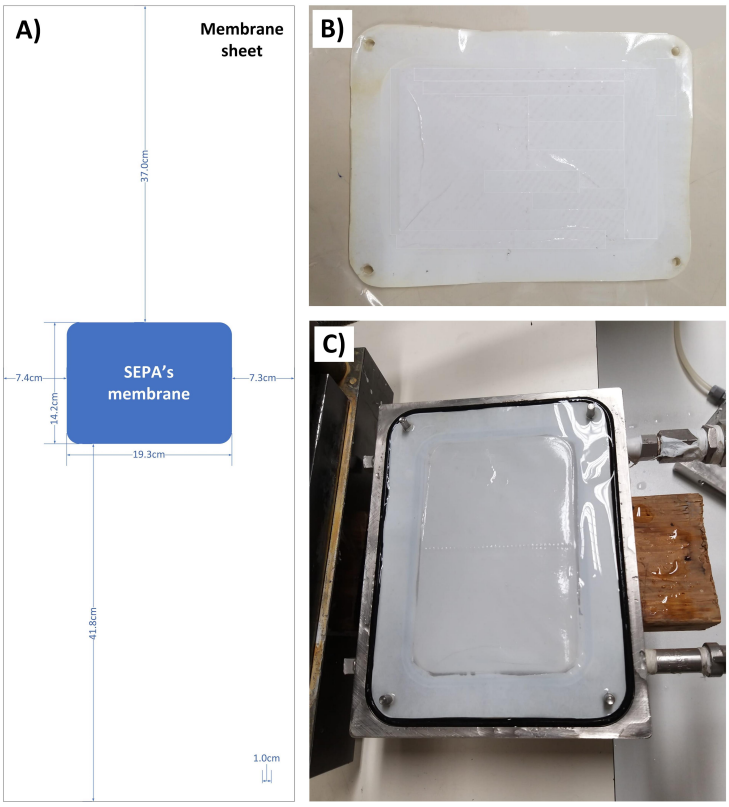

Figure 4.1: A) Schematic representation of the membrane sheet highlighting the area from which the membrane section was cut out, with specific dimensions provided. B) Membrane section tested. C) Membrane section installed in the SEPA unit.

Flow rate calibration

As previously stated, the feed pump operates under the control of a variable-frequency drive (VFD). Thus, the selected frequency on the VFD determines the feed flow rate. Using the calibration line established earlier (Appendix A.3), the frequency that corresponds to the desired flow rate (3 L/min) was identified as being 11 Hz. This was the frequency set for all SEPA unit tests.

Dead volume

Dead volume is the residual solution volume that is retained in the SEPA unit pipes following each operation. Before starting each filtration process, the unit is thoroughly washed with water to eliminate any remaining solution within the pipes and on the membrane surface. However, even after this cleaning process, water remains within the unit. The residue of water inside the unit is what is called 'dead volume'. This residual water needs to be removed to prevent dilution of the succeeding solution tested. The dead volume was quantified to be approximately 400 mL. Therefore, at the beginning of each test, the initial 450 mL exiting the unit is collected and extracted from the circuit to ensure complete removal of the dead volume.

4.2 Hydraulic Permeability

As noted in Section 2.4, hydraulic permeability represents the ability of the membrane to allow the passage of water. To determine this parameter, filtrations using deionized water were conducted at five different feed pressures (detailed results can be found in Appendix B.1).

Figure 4.2 displays the permeate flux plotted against the applied pressure. As expected from Equation 2.5, the permeate flux exhibits a linear relationship with the transmembrane pressure.

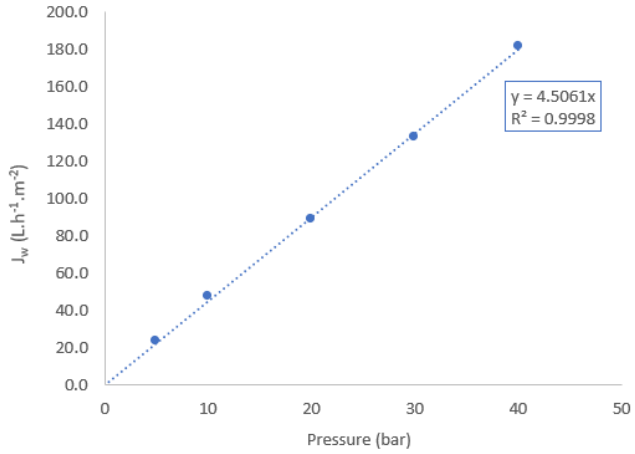

Pressure (bar)	Permeate flux L/(m2.h)
40	181.6
30	133.1
20	89.0
10	47.4
5	23.5

Figure 4.2: Water flux results in the SEPA unit.

The hydraulic permeability is obtained from the slope of the linear regression. The determined value is presented in Table 4.1:

Table 4.1: Equation for the linear regression and its corresponding hydraulic permeability value, obtained from the slope.

$J_w = f(\Delta p_m)$	$L_p(\frac{L}{m^2 \cdot h \cdot bar})$	$L_p(\frac{m}{s \cdot Pa})$
$J_w = 4.5061 \Delta p_m$ $R^2 = 0.9998$	4.51	1.25 x 10^{-11}

4.3 Solute Rejection

The study of the NF membrane solute rejection was carried out using three reference solutes specified in the membrane's data sheet (Appendix A.1): sodium chloride (NaCl), magnesium sulfate ($MgSO_4$), and lactose. The first goal was to replicate the manufacturer's test conditions to verify whether the membrane section installed in the SEPA unit achieves the expected rejections. Secondly, multiple tests were conducted at different transmembrane pressures and with varying solute concentrations to evaluate how the membrane responds to these changes in terms of permeate flux and rejection. These results will later be compared with the results obtained in the CNF device, so that conclusions can be drawn as to the feasibility of the centrifugation process. The solute concentrations tested were:

- Lactose at 5, 10 and 20 g/L.
- NaCl at 1, 2, 5 and 10 g/L.
- $MgSO_4$ at 1, 2, 5 and 10 g/L.

Table 4.2 presents the average rejections expected by the manufacturer, using Synder's NFS (TFC 100-250Da) membrane, and respective test conditions.

Table 4.2: NFS (TFC 100-250Da) membrane rejection specifications (Appendix A.1).

Solute	Average rejection	Test conditions	
		Concentration (g/L)	Pressure (bar)
NaCl	50.0 %	2	7.6
$MgSO_4$	99.5 %	2	7.6
Lactose	99.5 %	20	7.6

Before analysing the rejection results, it is important to contextualize the expectations based on our understanding of nanofiltration mechanisms detailed in Section 2.6. Nanofiltration membranes' exclusion mechanism is a combination of steric exclusion, which is a size-based separation, and non-sieving mechanisms, prominently the Donnan exclusion, attributed to the electrostatic interactions between charged solutes and the membrane's charged interface. Starting with lactose, given its significant molecular weight (342.3 g/mol), it's reasonable to attribute its high rejection rate (99.5 %) to the steric exclusion mechanism. This is because its size is likely larger than the effective pore size of the membrane, leading to its high rejection. As for the salts, NaCl and $MgSO_4$, they are believed to be primarily influenced by the Donnan exclusion mechanism, as described in Section 2.6.1. This mechanism suggests that charged ions are attracted to and retained by the oppositely charged membrane. According to the principles of Donnan exclusion, ions with greater charges face higher retention. Consequently, $MgSO_4$, with its divalent ions, is anticipated to exhibit greater rejection compared to NaCl, which consists of monovalent ions. $MgSO_4$, being a larger molecule (120,4 g/mol), could also have steric exclusion contributing to its high rejection.

Now that we have established the theoretical expectations based on the membrane's exclusion mechanisms, the next step is to analyze the actual rejection results obtained during the experiments.

Figure 4.3 compares the rejections achieved in the SEPA unit for the three solutes against the manufacturer's reference values (50.0% for NaCl and 99.5% for $MgSO_4$ and lactose). These experiments were conducted under the same conditions as those specified in Table 4.2. The values in Figure 4.3 represent the arithmetic average of three tests. The detailed results are available in Appendix B.2.

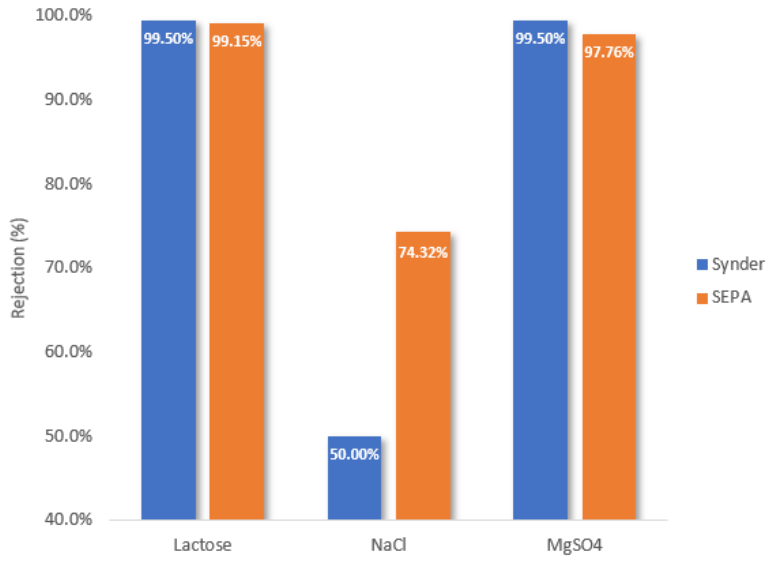

Figure 4.3: Comparison of experimental solute rejection in the SEPA unit with manufacturer specifications (Synder) for different solutes: NaCl, $MgSO_4$, and lactose. The experiments were performed at 7.6 bar. Detailed results are available in Appendix B.1.

The average lactose rejection was 99.15%, making it the closest to the expected value, with a deviation of less than 0.5%. For the magnesium sulfate solution, a rejection of 97.76% was obtained, representing a deviation of almost 2% from the expected 99.5%. The lower rejection of $MgSO_4$ compared to lactose could be due to physical structure of the membrane section used in the SEPA unit, such as having a larger pore size than expected. This would allow the smaller $MgSO_4$ molecule easier passage when compared to the larger lactose molecule. Another factor could be the different methods used for solute analysis, since HPLC provides more accurate results than the conductometer. In contrast, the results for NaCl were significantly higher than the manufacturer's reference value of 50.0%, with a rejection of 74.3%. This could suggest that the specific membrane section used in the SEPA unit may have a particularly charged surface, which serves as the primary rejection mechanism for small salts such as NaCl. This results are shown in Table 4.3.

Table 4.3: Average rejection results obtained in the SEPA unit with the feed pressure of 7.6 bar, and comparison with the reference values.

Solute	SEPA	Synder	Deviation
NaCl (2 g/L)	74.30 %	50.00 %	48.60 %
MgSO4 (2 g/L)	97.76 %	99.50 %	1.75 %
Lactose (20 g/L)	99.15 %	99.50 %	0.35 %

To investigate the behavior of rejection regarding variations in concentration and pressure, each of the solutions mentioned above were filtered five times in the SEPA unit at different applied feed pressures: 7.6, 10, 20, 30, and 40 bar. It's worth noting that 40 bar represents the maximum pressure the pressure gauge can withstand, which led to some instability in the filtrations performed at that pressure.

Figure 4.4 provides an overview of all experimental results in the SEPA unit. Figure 4.4 - A, C and D illustrate the variation in permeate flux as a function of the applied pressure, for different concentrations of lactose, NaCl and $MgSO_4$, respectively. Figure 4.4 - B, D and E present rejection results as a function of permeate flux for the same solutions. Detailed experimental results can be found in Appendix B.2.

Analyzing the permeate flux results, it is evident that higher feed pressures consistently lead to increased permeate flux, aligning with the predictions of Equation 2.5. Notably, the results reveal that permeate flux decreases as the solution becomes more concentrated, which holds true for all three solutes, as clearly depicted in Figure 4.4 – A, C, and E. This might indicate the occurrence of concentration polarization, described in Section 2.5.2.

Regarding rejection results, examining NaCl (Figure 4.4 - D), the rejection rate increases with rising permeate flux, until it stabilizes at around 100 $L.h^{-1}.m^{-2}$, aligning with the principles of the solution-diffusion model (as described in Section 2.4.1). When comparing results for different NaCl concentrations, it becomes evident that higher concentration solutions consistently exhibit lower rejection. This phenomenon is a clear sign of concentration polarization, since higher concentrations result in the formation of a boundary layer adjacent to the membrane with high concentration of solute, leading to a decrease in both rejection and permeate flux.

In contrast, for lactose and $MgSO_4$ (the solutes with the highest rejection rates), solute concentration does not significantly impact rejection results. Error bars in the graphs (Figure 4.4 - B and F) represent variations between triplicate tests conducted for the lactose solution at 20 g/L and the $MgSO_4$ solution at 2 g/L. This comparison highlights that the variation in rejection values for identical experiments nearly reaches that of solutions with different solute concentrations. This indicates that, unlike NaCl, the rejection of lactose and $MgSO_4$ is not significantly affected by concentration polarization.

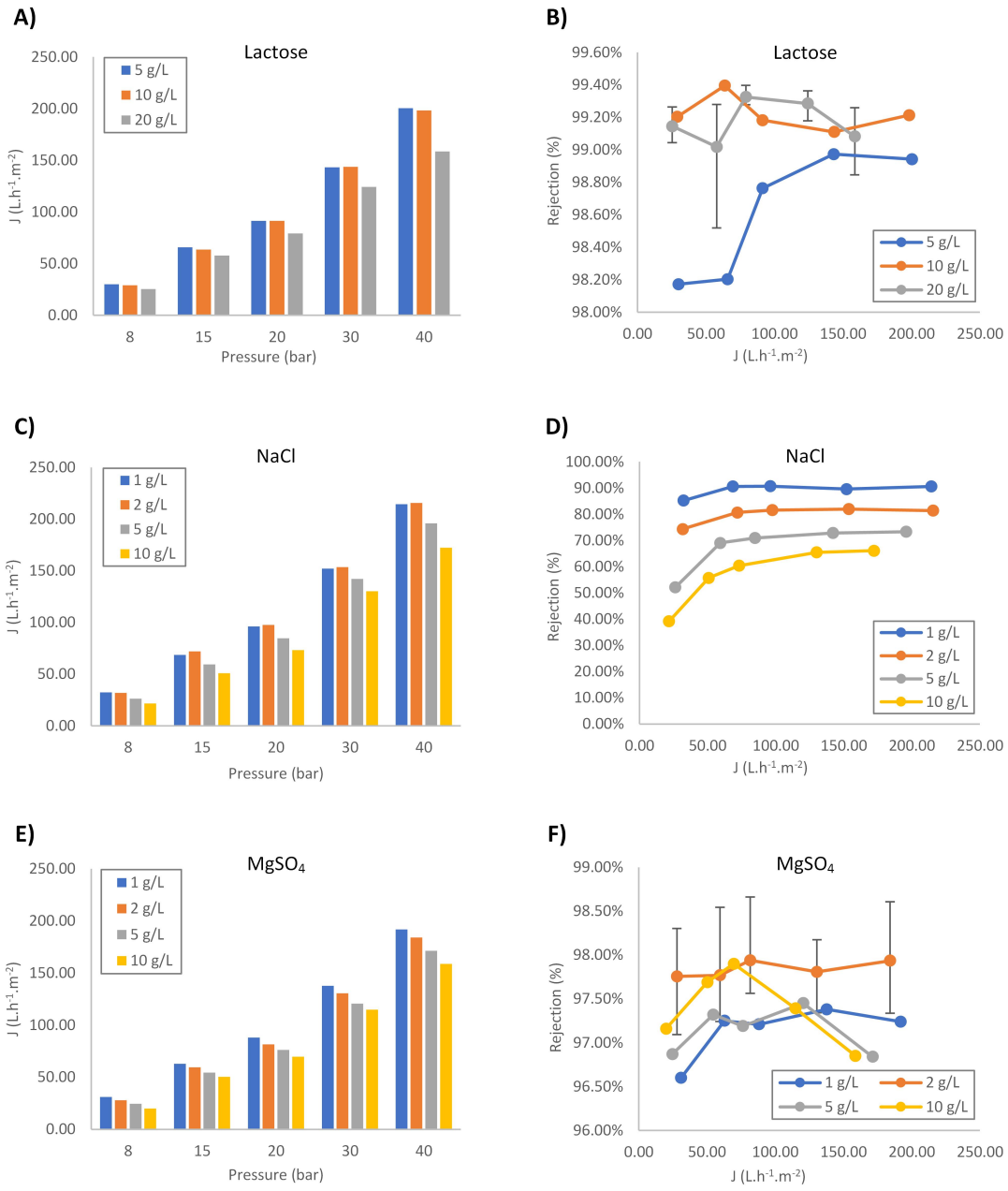

Figure 4.4: SEPA unit permeate flux and rejection results. A) and B) Lactose permeate flux and rejection results, respectively, for three different concentration solutions (5, 10 and 20 g/L). C) and D) NaCl permeate flux and rejection results, respectively, for four different concentration solutions (1, 2, 5 and 10 g/L). E) and F) $MgSO_4$ permeate flux and rejection results, respectively, for four different concentration solutions (1, 2, 5 and 10 g/L).

Finally, Figure 4.5 illustrates the permeate flux obtained for solutions with identical concentrations (5 and 10 g/L) of lactose, NaCl, and $MgSO_4$. This comparison allows us to investigate how the solute type impacts permeate flux, revealing that the salts exhibit overall lower permeate flux, possibly indicating that those polarize more than lactose.

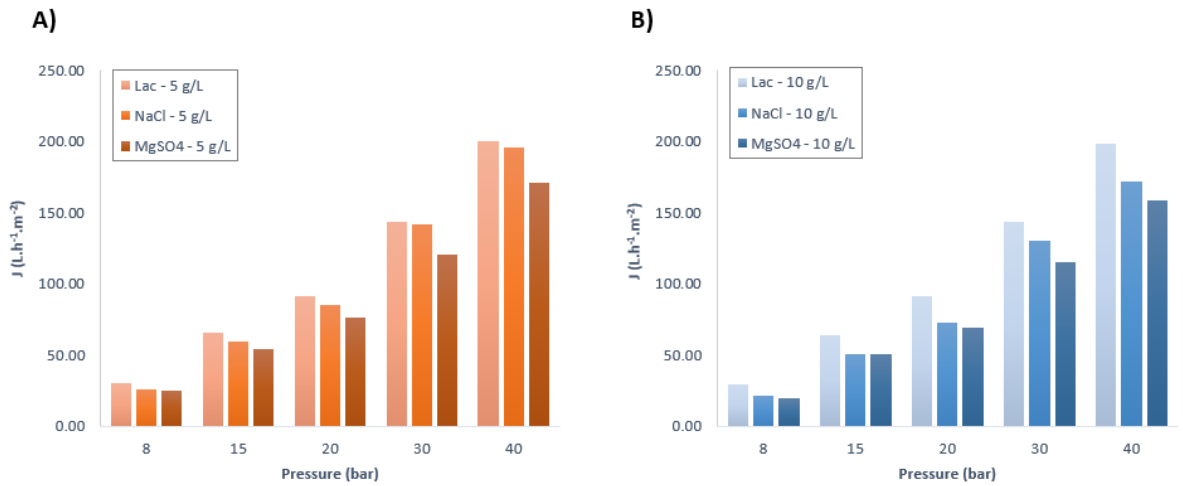

Figure 4.5: Comparison of the permeate fluxes obtained for solutions with the same concentration but different solutes (Lactose, NaCl and $MgSO_4$). A) 5 g/L solutions. B) 10 g/L solutions.

Chapter 5

Centrifugal Nanofiltration Device

5.1 Introduction

This chapter delves into the filtration study using the centrifugal nanofiltration (CNF) devices. The study was conducted using two different sets of membranes: one derived from the membrane used in the SEPA unit and another extracted from a distinct section of the original membrane sheet.

The primary objective is to assess the performance of the CNF device by repeating the membrane characterization process using the same solutions as those tested in the SEPA unit. This comparison aims to determine whether the CNF devices are able to replicate the results achieved in SEPA, when using the same membrane. Additionally, the new set of membranes is examined to investigate potential variations in membrane characteristics based on different sheet areas.

The initial part of this chapter focuses on describing the procedure used to establish the relationship between rotational speed and pressure within the device, which is an essential step in this research. This investigation utilizes a Computational Fluid Dynamics (CFD) software to analyze and identify the correspondence between these parameters.

5.2 Simulation postprocessing

As described in Section 3.2.3, *SimFlow*, a Computational Fluid Dynamics (CFD) software, was employed to estimate the pressure applied to the membrane inside the CNF device. The simulation built in Section 3.2.3 was conducted at rotational speeds ranging from 3000 to 16000 rpm until reaching a stabilized state. After completing each simulation, post-processing was necessary in order to determine the pressure distribution within the device. This post-processing was executed with the assistance of *ParaView*, a data analysis tool offering interactive 3D visualizations. Figure 5.1 illustrates the simulation imported into *ParaView*.

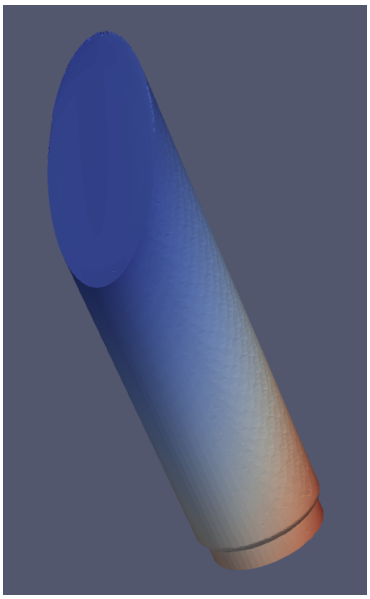

Figure 5.1: 3D fluid volume simulation imported into *ParaView*, depicting the pressure distribution within the CNF device during the computational fluid dynamics (CFD) analysis.

To illustrate the data processing in *ParaView*, this section will utilize the simulation run at 7000 rpm as an example. The same procedure was applied for other rotational speeds. It should be noted that every simulation carried out in *SimFlow* run until it reached a stabilized state, after which post-processing was always performed at time step 1000.

To determine the pressure applied to the membrane, the focus was on the plane representing the membrane's surface (shown in Figure 5.2). From the image, it is evident that the pressure applied to the surface of the membrane is not uniform, which is a result of the membrane's angled position regarding the centrifugal force direction. Therefore, the pressure applied to the membrane was considered to be the average pressure in this plane.

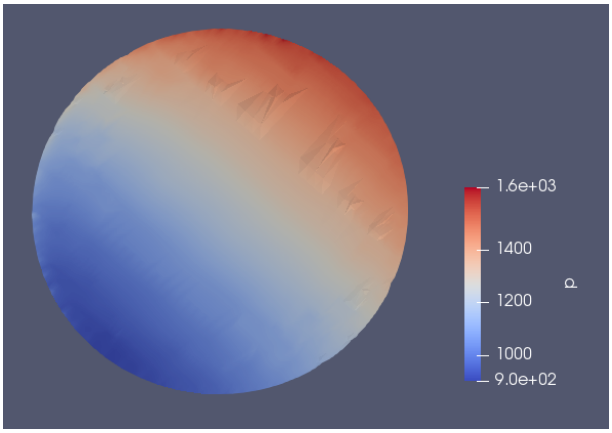

Figure 5.2: Visualization of pressure variation across the membrane surface inside the CNF device, showing non-uniform pressure distribution due to the membrane's angled position relative to the centrifugal force.

To calculate the average pressure exerted by the fluid on the membrane, the ”Integrate Variables” tool was applied. This tool's primary function is to perform the integration of relevant variables across a surface, in our case, the membrane surface. The results are presented in Figure 5.3.

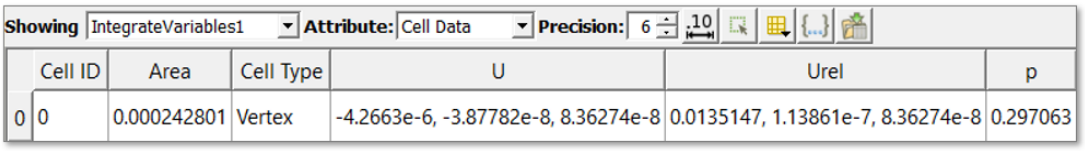

	Cell ID	Area	Cell Type	U	Urel	p
0	0	0.000242801	Vertex	-4.2663e-6, -3.87782e-8, 8.36274e-8	0.0135147, 1.13861e-7, 8.36274e-8	0.297063

Figure 5.3: Results obtained from the application of the ”Integrate Variables” tool, showing the integrated pressure within the selected section of the CNF device membrane surface.

The pressure value obtained represents the integrated pressure across the selected region, but this isn't the value we are seeking. To acquire the desired value, the integrated pressure needs to be divided by the membrane's area (2.4 cm^2). It's worth noting that the *openFOAM* solver operates with pressure divided by density, measured in units of m^2/s^2. Therefore, to express the pressure in Pascals, the pressure value must be multiplied by the fluid's density, which is assumed to be approximately that of water ($\approx$1000 kg/m^3).

Table 5.1 displays the pressure results obtained at a rotational speed of 7000 rpm.

Table 5.1: Integrated pressure in the membrane surface, at a rotational speed of 7000 rpm, and conversion to values in both Pascals (Pa) and bars (bar).

Integrated pressure	**p/rho (m^2/s^2)**	**Pressure (Pa)**	**Pressure (bar)**
0.297063	1222.6	1222637.5	12.2

It's important to acknowledge that the calculated pressure corresponds to a scenario where the device is filled to its maximum capacity, approximately 18.1 mL. This condition is not practical for experimental testing due it being difficult to measure and the risk of spillage during the centrifuge's acceleration and deceleration phases. In all experimental tests, the device was loaded with 10 mL of fluid, which results in a comparatively lower pressure applied to the membrane than if it was fully loaded.

As previously explained, the centrifugal force pushes the fluid away from the axis of rotation, resulting in the fluid's surface being oriented perpendicular to this force. This implies that, as depicted in Figure 5.4, the pressure is uniformly applied to this surface. Furthermore, if the fluid module is sliced in various planes parallel to the surface, the pressure in those ”slices” remains uniform, as indicated by the pressure contours in Figure 5.4.

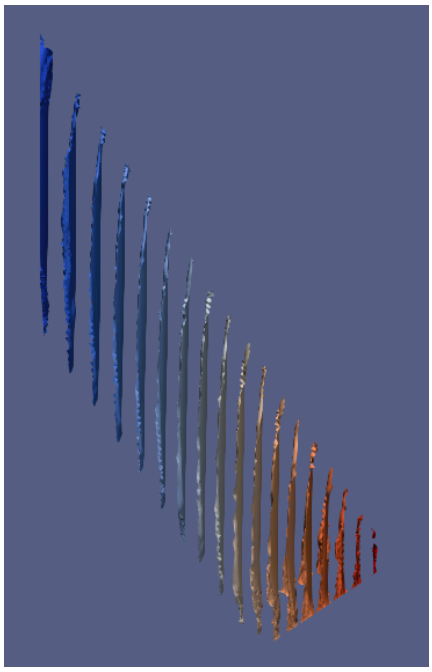

Figure 5.4: Pressure contours illustrating the uniform pressure applied to the surface of the fluid.

Right at the fluid's surface, the pressure registers as zero. Therefore, we can assume that the pressure exerted on the membrane by 10 mL of fluid corresponds to the pressure at which the surface of a 10 mL volume of fluid also measures zero. To avoid the necessity of creating a new geometry and conducting another simulation, we derived the pressure applied by 10 mL of fluid through subtraction. This involved deducting the pressure on the section representing the fluid's surface for the desired 10 mL volume (p_2) from the previously determined membrane surface pressure for the maximum fluid volume (p_1), as visually explained in Figure 5.5.

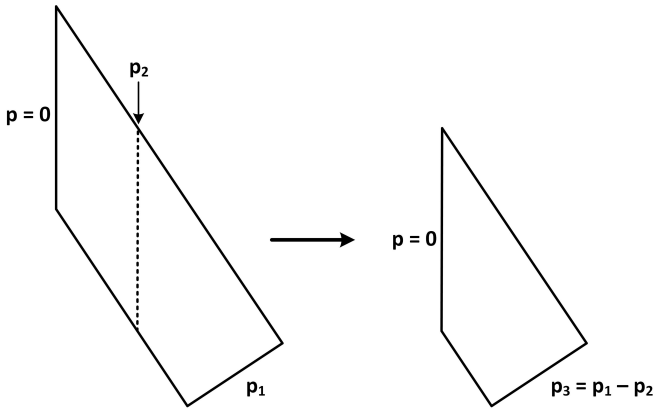

Figure 5.5: Visual representation of the process used to calculate pressure for volumes less than the maximum.

In order to calculate the pressure on the slice representing a 10 mL volume of fluid (p_2), we needed to slice the geometry along a plane parallel to the fluid's surface. This operation was accomplished using the "Clip" tool, which allows the removal of sections from any dataset by employing a plane, sphere, or

box. The ”Integrate Variables” tool was employed again, as it provides the geometry’s volume, guiding the location for cutting to achieve the desired volume. Figure 5.6 shows the new volume of fluid cut from the original geometry.

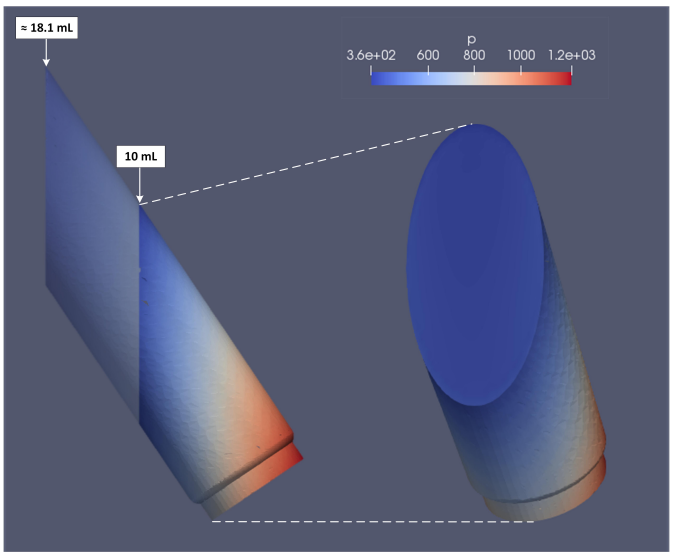

Figure 5.6: Illustration of the 10 mL fluid volume obtained by clipping the original geometry, in the CNF device simulation.

The pressure at the fluid’s surface was then measured and is presented in Table 5.2, along with the pressure exerted on the membrane by 10 mL of fluid, for an experiment conducted at 7000 rpm, calculated as explained in Figure 5.5.

Table 5.2: Pressure values on the membrane surface for the simulation at 7000 rpm. It includes the pressure applied by a 10 mL volume of fluid (p_3), the pressure at maximum fluid volume (p_1), and the pressure at the surface of a 10 mL volume (p_2).

Surface (10 mL) - p_2			**Membrane (max volume) - p_1**	**Membrane (10 mL) - p_3**
p/rho (m2/s2)	**p (Pa)**	**p (bar)**	**p (bar)**	**p (bar)**
432	432000	4.32	12.23	7.9

This process was repeated for all simulations conducted at rotational speeds other than 7000 rpm. By plotting the obtained pressure as a function of the speed, we established a correlation between these two variables (as shown in Figure 5.7). As previously mentioned, the volume of feed solution loaded into the CNF devices was 10 mL for every experiment. However, correlations were also established for feed volumes of 5, 7, 12, and 15 mL, and these are all presented in Table 5.3. Detailed results can be found in Appendix C.1.

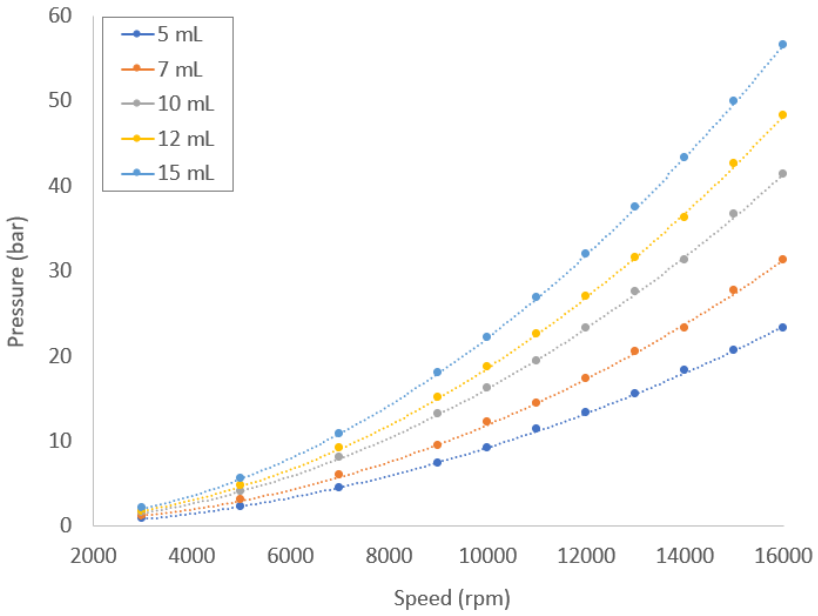

Figure 5.7: Correlation between rotational speed and pressure applied to the membrane, for various fluid volumes.

Table 5.3: Correlations between pressure (bar) as a function of rotational speed (rpm), various fluid volumes.

Volume (mL)	**Pressure = f(speed)**
5.0	$p = 8.97x10^{-8}\ rpm^2 + 3.94\times10^{-5}\ rpm - 1.89x10^{-1}$ $R^2 = 1$
7.0	$p = 1.30x10^{-7}\ rpm^2 + 1.66\times10^{-4}\ rpm - 5.10x10^{-1}$ $R^2 = 0.99$
10.0	$p = 1.62x10^{-7}\ rpm^2 + 9.46\times10^{-6}\ rpm - 5.12x10^{-2}$ $R^2 = 1$
12.0	$p = 1.95x10^{-7}\ rpm^2 + 1.38\times10^{-4}\ rpm - 4.25x10^{-1}$ $R^2 = 1$
15.0	$p = 2.20x10^{-7}\ rpm^2 + 2.52\times10^{-5}\ rpm - 9.72x10^{-2}$ $R^2 = 1$

The equations presented in Table 5.3 enable us to calculate the rotational speed required in the centrifuge to achieve the desired pressure. Building upon the correlation established for the 10 mL volume, the pressures at which the experimental tests will be carried out, along with the corresponding rotational speed values, can be found in Table 5.4. The centrifuge only accommodates speed values rounded to the nearest hundred, as indicated in the table.

Table 5.4: Relationship between desired pressure levels (expressed in bar) and their corresponding speed settings (in rpm) for the centrifuge. The ”Speed set in centrifuge” column indicates the rounded speed values set in the centrifuge.

Pressure (bar)	Speed (rpm)	Speed set in centrifuge (rpm)
5.0	5561	5600
7.6	6861	6900
10.0	7872	7900
15.0	9643	9600
20.0	11135	11100
30.0	13636	13600
40.0	15745	15700

5.3 Membrane Preparation for CNF Device Testing

As previously discussed in Chapter 4, the SEPA unit experiments were conducted to characterize the membrane that would later be tested in the CNF device. The objective was to assess whether the CNF device could consistently replicate the results obtained using the identical membrane in a commercially available equipment.

Once the SEPA unit experiments were completed, the membrane section was carefully extracted and prepared to be installed into the CNF devices. This involved the precise cutting of multiple circular pieces, each measuring 24 mm in diameter, as shown in Figure 5.8. Notably, this relatively small membrane segment from the bench-scale unit yielded a total of twenty-two individual membranes. This outcome highlights the potential efficiency of the CNF device, as it significantly reduces resource requirements in comparison to traditional laboratory-scale methods.

Figure 5.8: Membrane section from the SEPA unit with the twenty-two individual membranes marked. The circular membranes in yellow were utilized in the subsequent CNF testing.

Out of this collection of circular membranes, only the fourteen highlighted in yellow in Figure 5.8 were utilized in testing. These membranes were employed in two sets of CNF devices: one with eight tubes (the rotor's maximum capacity) and another with six tubes.

5.4 Evaluation of SEPA Membrane in CNF Devices

5.4.1 Preparation

To conduct the centrifugal nanofiltration, a total of 16 devices, organized into two sets of 8, were manufactured and assembled following the procedures detailed in Chapter 3. Before initiating the experimental operation in the CNF devices, it was crucial to ensure their integrity and leak-proof performance during high-speed centrifugation. To achieve this, circles of an impermeable material with dimensions matching those of the membranes (24 mm in diameter) were meticulously cut and placed onto the devices. Then, the devices were filled with water, weighed, and subjected to centrifugation at 14,000 rpm, for 10 minutes each. The weight of the device after centrifugation was then compared to the initial weight. If the device is viable, weight after the centrifugation will match the initial weight, indicating there was no leakage during the operation.

Additionally, the permeate chamber was also inspected to ensure that no water was collected. The presence of water would suggest a potential leak in the sealing component of the device. Such leaks are undesirable as they could compromise the accuracy of the results in the real testing, since all collected permeate must cross the membrane without any bypass. Out of the devices tested, two displayed leaks, resulting in their exclusion from further testing.

The remaining 14 viable devices were individually numbered from 1 to 14. Each device was then paired with one of the membranes highlighted in Figure 5.8. Table 5.5 illustrates the allocation of specific membranes to their corresponding devices.

Table 5.5: Allocation of membranes to their respective devices.

	Membrane		**Membrane**
Device 1	1	Device 8	18
Device 2	22	Device 9	2
Device 3	6	Device 10	5
Device 4	8	Device 11	9
Device 5	10	Device 12	12
Device 6	14	Device 13	17
Device 7	16	Device 14	20

5.4.2 Pressure Correction Methodology

In Section 5.2, the correlation between pressure and rotational speed was established. However, it's important to note that the pressure values obtained are only accurate at the beginning of the filtration operation. As the fluid permeates the membrane and the concentrate volume decreases during centrifugation, the transmembrane pressure decreases, but not linearly. This non-linear variation hinders the calculation and comparison of permeate flux. To simplify the calculations and ensure more reliable comparisons, the test pressure will be approximated as the average between the initial and final pressure.

Each test is conducted at a constant rotational speed. Therefore, the final pressure corresponds to the pressure exerted on the membrane by the remaining concentrate volume under the specified centrifuge speed.

Since the correlation between pressure and rotational speed was previously established for different volumes (see Figure 5.7), it is possible to determine how the pressure varies with the concentrate volume loaded into the device for different experimental test speeds. This variation follows a linear relationship, as shown in Figure 5.9.

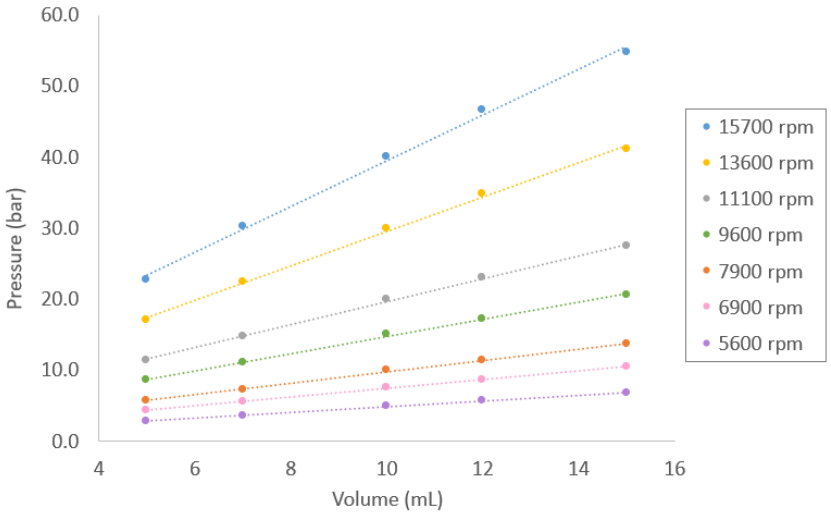

Figure 5.9: Relationship between pressure (bar) and volume (mL) at varying centrifuge speeds ranging from 5600 rpm to 15700 rpm. Each line represents the trend for a specific rpm.

Table 5.6: Correlation between rotational speed (expressed in rpm), volume (in mL), and the corresponding pressure values in the centrifuge.

Rotational speed (rpm)	$p = f(V)$
5600	p = 0.4038 × V + 0.8381 R^2 = 0.9978
6900	p = 0.6139 × V + 1.2864 R^2 = 0.9981
7900	p = 0.8074 × V + 1.7123 R^2 = 0.9983
9600	p = 1.2098 × V + 2.6211 R^2 = 0.9984
11100	p = 1.6116 × V + 3.5478 R^2 = 0.9983
13600	p = 2.4136 × V + 5.4310 R^2 = 0.9976
15700	p = 3.2152 × V + 7.3405 R^2 = 0.9969

To determine the final pressure, it is essential to measure the remaining volume of concentrate in the device after centrifugation. Prior to each test, the device, concentrate, and permeate chamber are weighed to determine the initial volume. By subtracting the permeate volume from the initial volume, the final concentrate volume in the device is determined.

The final pressure is calculated by substituting the measured volume in the linear regression equation for the speed at which the test was conducted (Table 5.6). The corrected pressure is then obtained as the average between this calculated pressure and the initial pressure. Table 5.7 presents the final volume, final pressure, and corrected pressure for filtrations with water, performed at different speeds.

Table 5.7: Final volume, final pressure, and corrected pressure values for different test conditions at varying rotational speeds.

Test	**Final volume (mL)**	**Final pressure (bar)**	**Corrected pressure (bar)**
5 bar - 5600 rpm	8.48	4.3	4.6
10 bar - 7900 rpm	8.54	8.6	9.2
20 bar - 11100 rpm	8.12	16.6	18.2
30 bar - 13600 rpm	8.11	25.0	27.3
40 bar - 15700 rpm	7.65	31.9	35.8

The experimental testing performed with water was repeated twice for each rotational speed, and the reported final volume represents the average of these two tests. Similarly, the pressure values for the tests conducted with the other solutions under study were also corrected. The results are provided

in Table 5.8. Additional data can be found in Appendix C.2.

Table 5.8: Corrected pressure values for different solution concentrations at various test conditions and rotational speed.

	Corrected pressure (bar)			
Test	**Lactose - 20 g/L**	**MgSO4 - 2 g/L**	**MgSO4 - 1 g/L**	**NaCl - 2 g/L**
7.6 bar - 6900 rpm	6.9	6.8	6.7	6.6
15 bar - 9600 rpm	13.4	13.3	13.2	13.2
20 bar - 11100 rpm	17.9	17.7	17.8	17.5
30 bar - 13600 rpm	27.0	27.1	27.0	26.7
40 bar - 15700 rpm	36.3	35.6	35.4	35.8

5.4.3 Hydraulic Permeability

The hydraulic permeability testing was performed using deionized water at pressures of 5, 10, 20, 30, and 40 bar, allowing for a direct comparison with the SEPA unit results. However, as previously mentioned, these pressures had to be adjusted to account for the pressure reduction due to the decrease in concentrate volume as the fluid permeates the membrane.

Regarding permeate flux, unlike the SEPA unit, it's not possible to measure it during the operation. Therefore, permeate flux was calculated by weighing the collected permeate in the permeate chamber. Given that the permeate is water, its weight in grams was assumed to be equivalent to the volume in milliliters. The measured permeate volume was then divided by the membrane area and duration of centrifugation to determine the permeate flux. This process was repeated for all subsequent experimental tests using the device.

For comparison with the SEPA unit, the permeate flux of the CNF device was considered to be the average across the 14 studied membranes. It's worth mentioning that due to the rotor's maximum capacity being limited to 8 devices, two consecutive centrifugations were performed.

Each test was replicated, and the reported results represent the average of the two experimental tests. Figure 5.10 compares the water permeation in the centrifuge with that previously obtained in the SEPA unit. More detailed data can be found in Appendix C.6. The similarities in the behavior of the membrane indicate that, in terms of water permeation, the CNF devices successfully replicated the conditions in the SEPA unit.

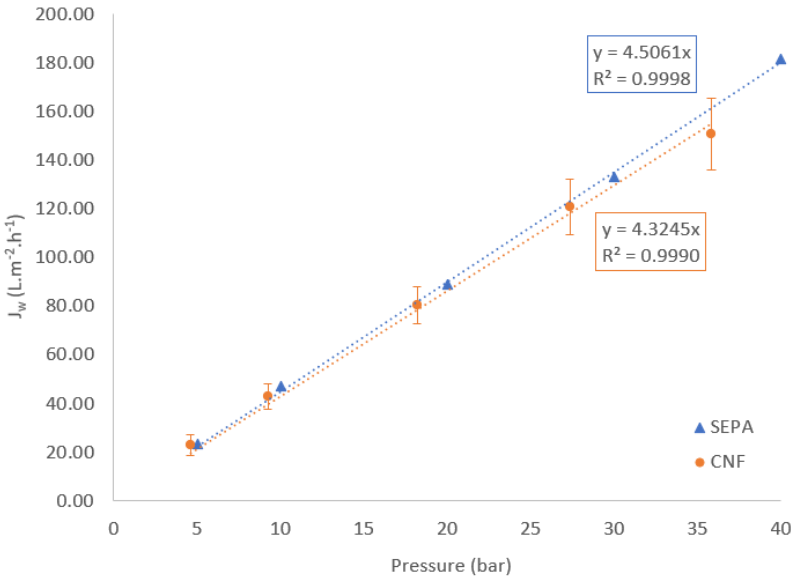

Figure 5.10: Relationship between permeate flux (J_w) and applied pressure for SEPA and CNF membranes. Linear regression finds the hydraulic permeability, which is represented by the slope.

Table 5.9 presents the hydraulic permeability values for both filtration methods, showing that they are within 4% of each other.

Table 5.9: Comparison of hydraulic permeability values obtained in the SEPA and in the CNF devices.

Device	$J_w = f(\Delta p_m)$	$L_p(\frac{L}{m^2 \cdot h \cdot bar})$	$L_p(\frac{m}{s \cdot Pa})$
SEPA	$J_w = 4.5061 \Delta p_m$ R^2 = 0.9998	4.51	1.25×10^{-11}
CNF	$J_w = 4.3245 \Delta p_m$ R^2 = 0.9990	4.32	1.20x10^{-11}

5.4.4 Selection of Membranes for Rejection Testing

In the hydraulic permeability study, all 14 available membrane sections were employed in 14 individual devices. However, for the subsequent rejection experimental tests, practical considerations and time constraints imposed the use of only eight membranes (maximum rotor capacity). The specific membranes selected for this purpose are indicated in Figure 5.11.

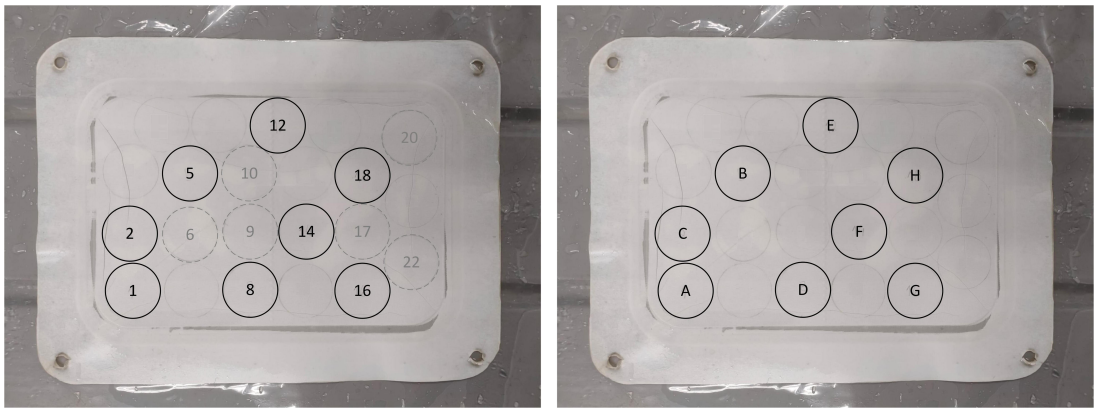

Figure 5.11: Selection of eight membranes for CNF testing. The left panel shows the chosen membranes from the original 14. The right panel shows the chosen membranes with the new labeling (A to H).

The selection of membranes was based on three criteria: membrane condition, position within the section, and its ability to represent the overall results. The first criterion concerns to the physical state of the membranes. Since these membranes were cut from a section previously tested at high pressures, some regions may have been creased, which could potentially affect the correct sealing of the device. The position of the membranes within the section was also considered to ensure a representative sample of the SEPA section. Membranes were chosen from different positions across the section, aiming to capture its overall characteristics.

Furthermore, the eight chosen membranes needed to accurately mirror the results achieved by the 14 originally studied membranes in terms of water permeation. This was evaluated by examining the hydraulic permeability values achieved by each individual membrane. Figure 5.12 presents the hydraulic permeability values for all 14 membranes, highlighting those corresponding to the eight selected membranes (A to H). The horizontal lines indicate the average hydraulic permeability values for both the entire set of membranes and the chosen ones.

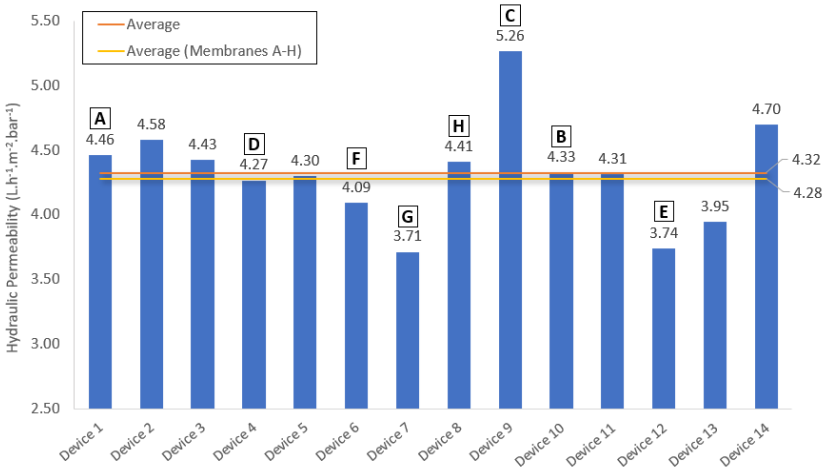

Figure 5.12: Hydraulic permeability values for all 14 membranes, with membranes A to H representing the selected ones. The horizontal lines represent the average permeability for both the entire set of membranes and the chosen ones.

The average permeability of membranes A to H stands at 4.28, whereas for all 14 membranes, it reaches 4.32, which corresponds to a variations of less than 1%.

Hydraulic permeability is the constant that governs the relationship between water permeate flux and pressure. Therefore, if this value is identical for both sets, the average permeate flux is expected to be the same, as depicted in Figure 5.13. Based on the analysis considering the three criteria, it was determined that using fewer membranes in the remaining experimental tests would not compromise the validity of the future conclusions.

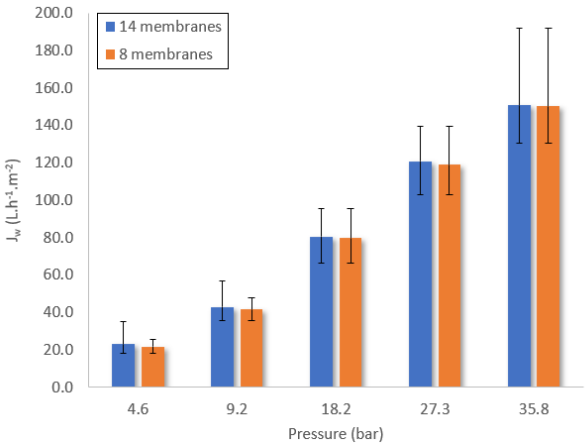

	Pressure (bar)				
	4.6	**9.2**	**18.2**	**27.3**	**35.8**
Average flux 14 membranes	23.0	43.0	80.5	120.8	150.8
Average flux 8 membranes	21.7	41.8	79.8	118.9	150.4
Difference	5.8%	2.8%	0.9%	1.5%	0.3%

Figure 5.13: Comparison of permeate flux between the set of 14 membranes and the 8 selected membranes.

When analyzing the individual permeate fluxes within the selected membranes, as depicted in Figure 5.14, it becomes apparent that membrane C achieves the highest water permeation, registering at L_p = 5.26 L.h^{-1}.m^{-2}.bar^{-1}. On the other hand, membranes E and G exhibit the lowest values, recording L_p = 3.74 L.h^{-1}.m^{-2}.bar^{-1} and L_p = 3.71 L.h^{-1}.m^{-2}.bar^{-1}, respectively. The difference between the highest and lowest permeability values amounts to approximately 30%.

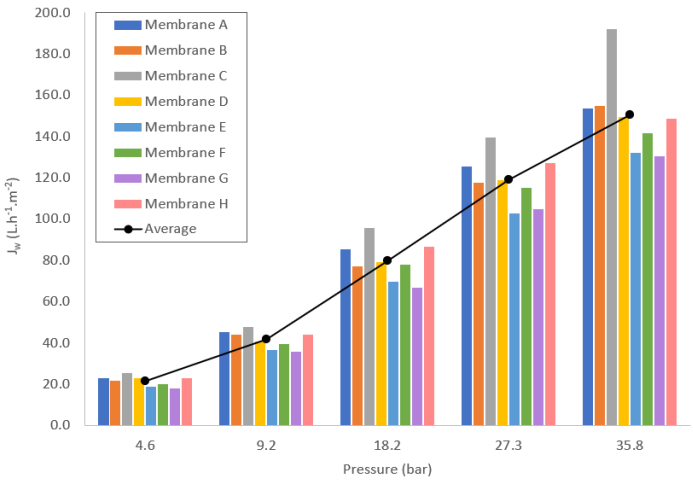

Figure 5.14: Water permeate flux (J_w) of membranes A through H under varying pressure conditions. The black line represents the average permeability across all membranes at each pressure point.

5.4.5 Solute Rejection in CNF Device

Having established that the CNF devices reproduces the water permeability results from the SEPA unit, the next step is to assess their performance regarding solute rejection. The following solutions were studied:

- Lactose at 20 g/L.
- NaCl at 2 g/L;
- $MgSO_4$ at 2 g/L;

These solutions were filtered in the centrifuge at pressures listed in Table 5.8, utilizing the eight selected membranes. Detailed measurements for permeate fluxes and rejections across each device can be found in Appendix C.5.

Figure 5.15 shows the average permeate flux achieved in the CNF devices plotted against the pressure applied, and compares it against the SEPA unit results for the same solutions.

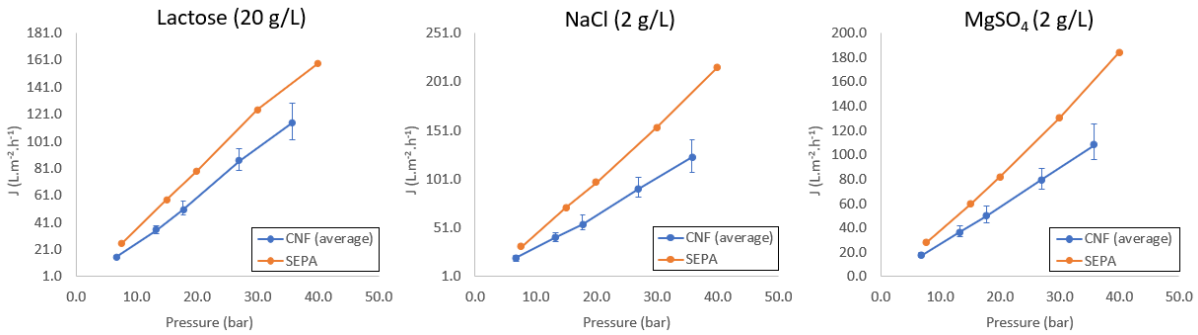

Figure 5.15: Comparison of average permeate flux as a function of applied pressure for the solutes Lactose, NaCl, and $MgSO_4$ between CNF devices and the SEPA unit. Error bars represent the standard deviation for the CNF measurements.

Upon evaluating the results, it's evident that the CNF device consistently achieves a lower permeate flux for all tested solutions in contrast to the SEPA unit. This discrepancy is a clear indication of the phenomenon of concentration polarization. As previously mentioned, concentration polarization arises when solute concentration at the membrane surface increases due to permeation, thus hindering the permeate flux. Similarly to what happened in the SEPA unit, this phenomenon is particularly noticeable for the salts, NaCl and $MgSO_4$, while lactose seemed more resistant to its effects. The difference can be attributed to the solute's nature.

Turning our attention to the solute rejection results, Figure 5.16 shows the rejections observed for the three studied solutions in the CNF device. This graphs provide information on the performance of each of the eight individual membranes, along with the average rejection.

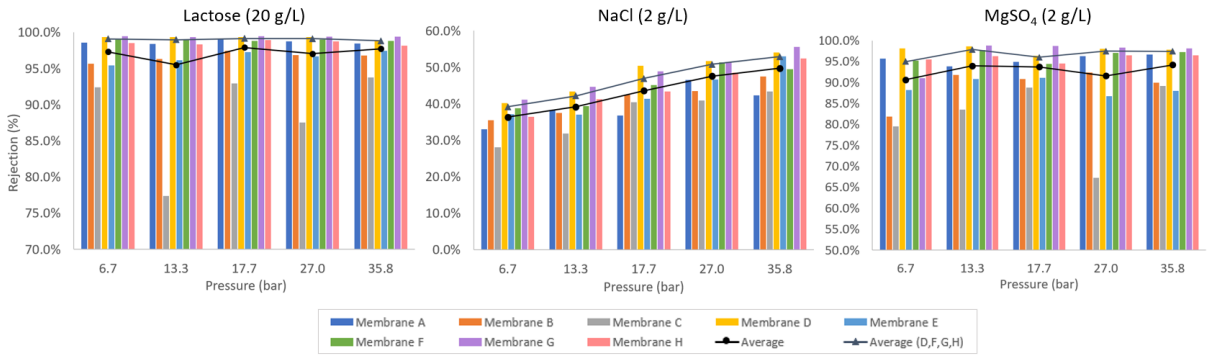

Figure 5.16: Solute rejection rates of the three tested solutes – Lactose, NaCl, and $MgSO_4$ – across different applied pressures for each of the eight membrane devices (A-H). The average rejection trendlines for all membranes and for the membranes with superior rejection are highlighted in black and grey, respectively.

Despite the variability in rejection rates, each membrane's behavior remains consistent across different solutes. For instance, if a membrane exhibits a high rejection for lactose, it likely shows a high rejection for $MgSO_4$ and NaCl. This consistency shows the ability of the devices to maintain stable conditions across all experiments, suggesting that different results are probably a result of membrane proprieties variations.

A closer inspection of individual membranes reveals a notable distinction in solute rejection performances. Membranes D, F, G, and H consistently demonstrated superior rejection rates for all tested solutes. Consequently, it was interesting to analyze from which regions of the SEPA membrane these samples originated. Figure 5.17 illustrates the placement of each of the eight membranes.

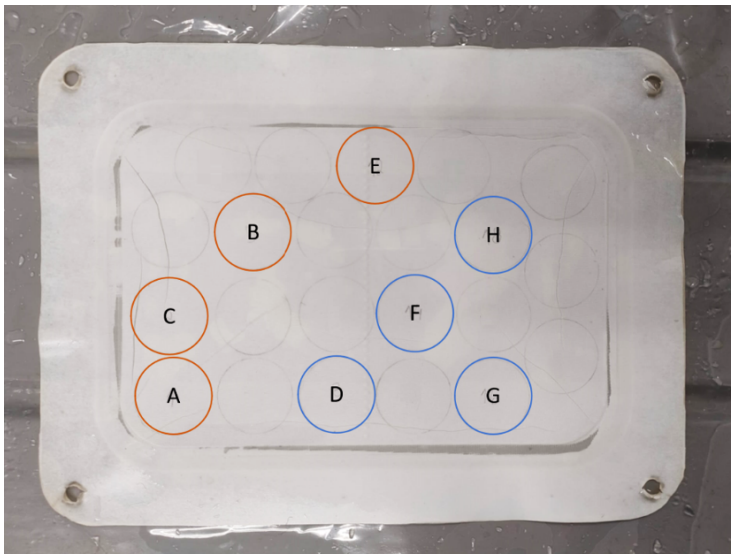

Figure 5.17: Spatial positioning of individual membranes (A-H) in the SEPA section. Membranes highlighted in blue (D, F, G, H) consistently demonstrated the highest solute rejection rates, whereas those in orange (A, B, C, E) exhibited the lowest.

The spatial configuration within the SEPA section indicates a trend in rejection performance, with those showing higher results (D, F, G, H) situated close to one another. These findings suggest an inherent variability in the membrane's properties, likely attributed to variations in the production process. Research indicates that membrane characteristics, particularly solute rejection rates, maintain consistency on a larger scale, typically around 1 m^2. Below this scale, variability from area to area becomes more pronounced, which explains why these smaller membranes do not show consistent performance from one section to the another.

Therefore, if one intends to represent the membrane's performance accurately based on a smaller sample, it would be necessary to do extensive testing across numerous samples to identify those that most closely align with the average characteristics of a 1 m^2 membrane segment. This method accounts for the heterogeneity resulting from the production process and ensures a more representative evaluation of the membrane's overall performance.

Given this performance difference, the results from membranes D, F, G, and H are considered more representative of the SEPA unit membrane characteristics. Therefore, the average performance from these four membranes will be the one utilized in subsequent analyses.

Figure 5.18 shows the rejection rates of the three solutes (Lactose, NaCl, and MgSO4) obtained as a function of the permeate flux. The analysis compares the average rejection rates of membranes D, F, G, H with those of the SEPA unit.

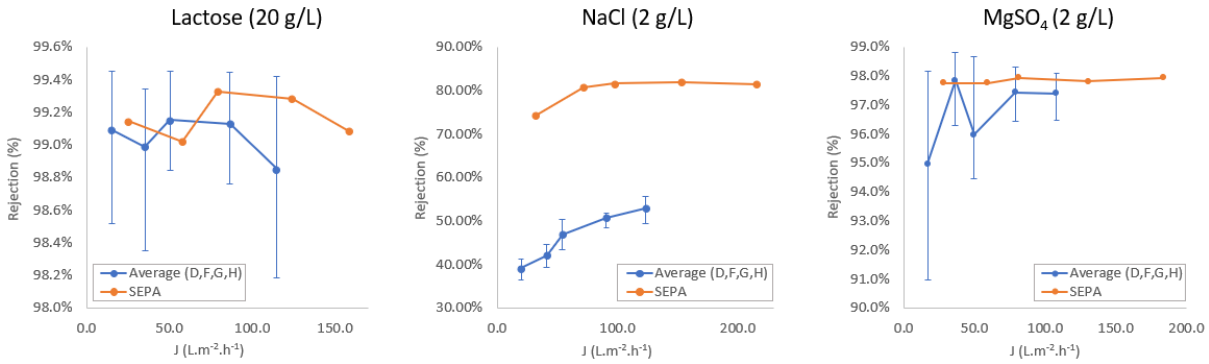

Figure 5.18: Solute rejection rates of Lactose, NaCl, and $MgSO_4$ at varying flux rates. The graph compares the average rejection performance of membranes D, F, G, H against that of the SEPA unit.

For Lactose and $MgSO_4$, the average performance of membranes D, F, G, H closely replicates that of the SEPA unit. In contrast, for NaCl, a pronounced difference is evident; the SEPA unit notably exceeds the average performance of the CNF membranes. This accentuated difference highlights the impact of concentration polarization on NaCl rejection results. It's also worth to note that there is a considerable variation in solute rejection among membranes D, F, G, H, as indicated by the error bars), particularly for $MgSO_4$ and lactose. This once again highlights the importance of selecting a representative sample of the larger membrane, as was the case for this four membranes, that, on average, match the SEPA unit's performance.

Additionally, a more diluted solution of $MgSO_4$ (1 g/L) was tested to evaluate if the membrane behavior of the CNF device towards a more diluted solution is similar to that of the SEPA unit. Figure 5.19 compares the permeate fluxes and rejection rates of both $MgSO_4$ solutions in the CNF devices and the SEPA unit.

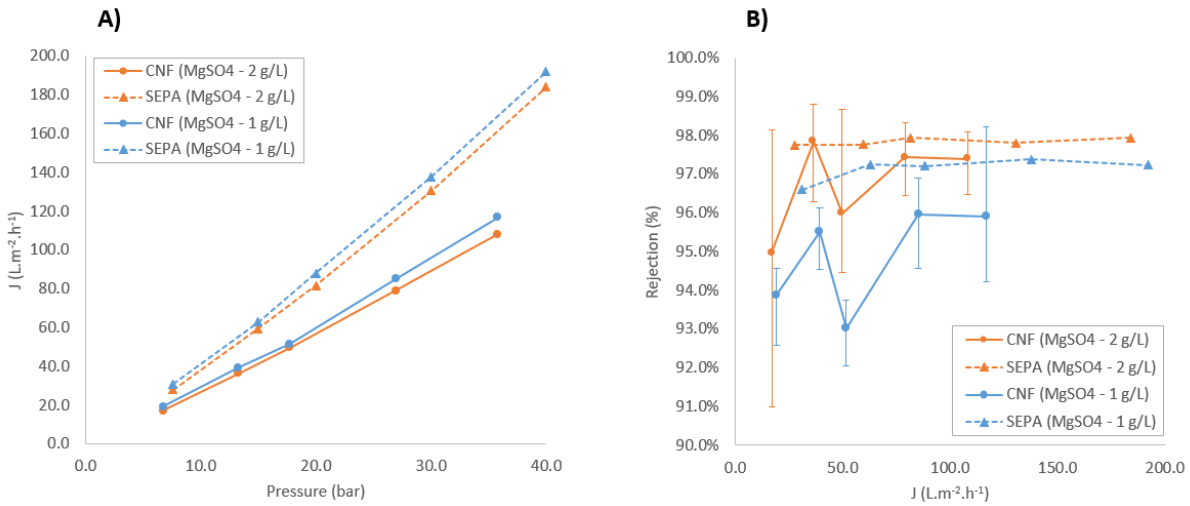

Figure 5.19: Comparative analysis of permeate flux (A) and solute rejection rates (B) for $MgSO_4$ solutions of two different concentrations (1 g/L and 2 g/L). The CNF device's performance is compared with the SEPA unit's results.

At both 1 g/L and 2 g/L $MgSO_4$ concentrations, the SEPA unit consistently outperforms the CNF device in terms of permeate flux across the entire pressure spectrum. This is consistent with previous observations (as seen in Figure 5.15), highlighting that the CNF device's permeate flux is notably influenced by concentration polarization for all solutes. In terms of the impact of concentration on permeate flux, both filtration methods exhibit a very similar behavior; a higher solute concentration leads to a slightly reduction in permeate flux. Regarding solute rejection, both equipment tend to exhibit a decrease in rejection rates for solutions with a lower concentration. However, it is evident that the rejection results for the more diluted solution (1 g/L) in the CNF device deviate more from the SEPA results than the solution with 2 g/L, suggesting that the device might perform better for higher concentrations. To confirm this, solutions with concentrations higher than 2 g/L should also be tested.

In summary, the CNF device presents a valuable tool for membrane sample testing, showing reliable results for lactose and $MgSO_4$. However, it's evident that steps need to be taken to optimize its design, particularly to eliminate or at least reduce the effects of concentration polarization.

5.5 Introduction of a New Membrane Set

In the final phase of this research, we extracted eight new membrane circles from a different section of the primary NFS (TFC 100-250Da) membrane sheet. The objective was to ascertain potential performance variability of membranes extracted from entirely different regions of the original sheet. Figure 5.20 illustrates the specific region on the membrane sheet from which these new membranes were extracted.

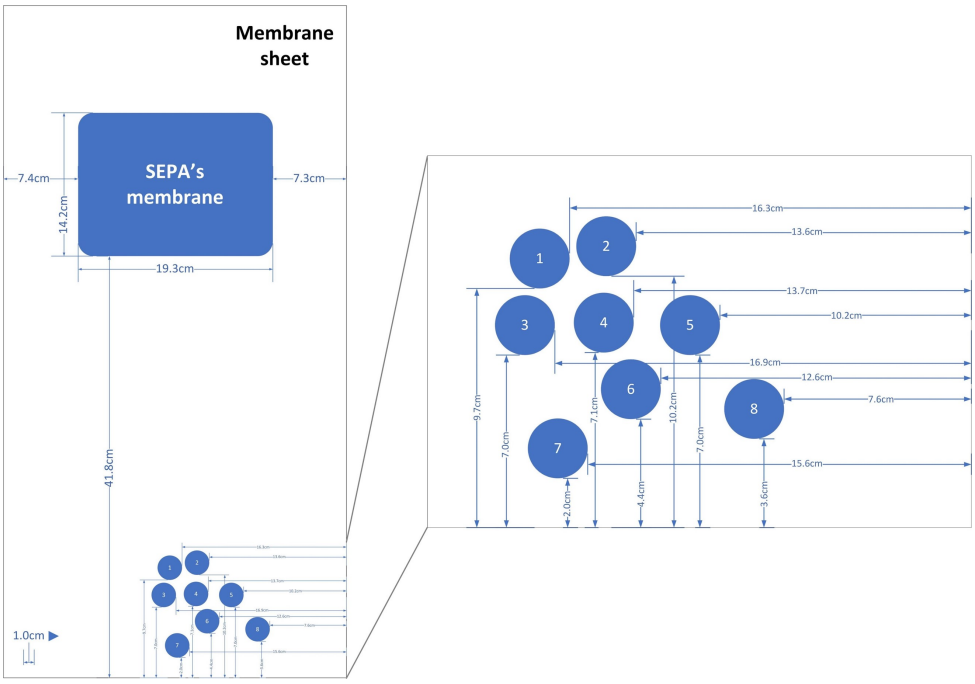

Figure 5.20: Schematic representation of the membrane sheet, illustrating both the SEPA's membrane and the locations from which the new set of membranes (numbered 1 through 8) were extracted.

The experimental procedures were similar to previous tests. Both hydraulic permeability and solute rejection rates, using the same three solutions, were evaluated, enabling a direct performance comparison between the two membrane sets. Within this section, 'CNF1' represents the set derived from the SEPA membrane, and 'CNF2' refers to the new membrane set.

As with CNF1, the pressures used in the experiments required adjustment to accommodate the volume decrease as the fluid permeates, employing the same methodology detailed in Section 5.4.2. The adjusted pressures can be found in Appendix C.3.

Prior to initiating the tests with the new membrane set, the eight membranes were subjected to compaction tests to replicate the conditions of the CNF2 membranes post-SEPA processing. These tests involved four 15 minute centrifuge runs at 40 bar.

Examining the hydraulic permeability depicted in Figure 5.21, the newly introduced membrane set showed a lower value (3.77) than CNF2 (4.32). This indicates distinctive inherent properties in the extraction location of the new membranes, suggesting a possible denser structure that restricts water passage.

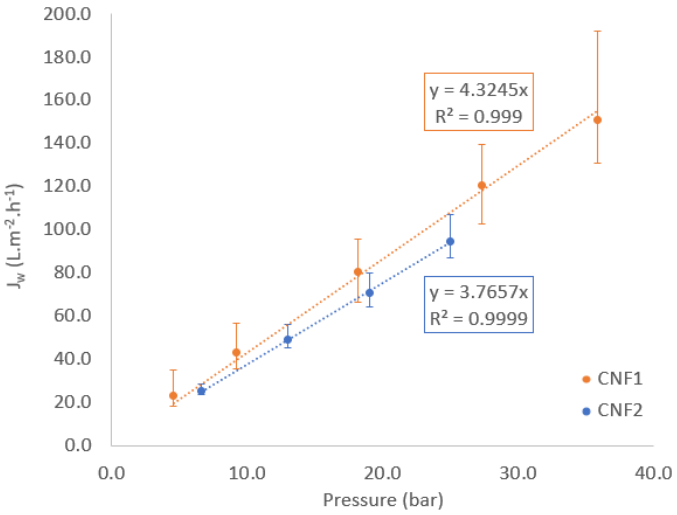

Figure 5.21: Comparison of average hydraulic permeability as a function of pressure for two sets of membranes, CNF1 and CNF2 (Detailed data in Appendix C.6).

For solute filtration tests, the same three solute solutions were used: Lactose at 20 g/L, NaCl at 2 g/L, and $MgSO_4$ at 2 g/L. Detailed data from the CNF2 tests are presented in Appendix C.7. Figure 5.22 shows the average permeate flux obtained for each of the solutions, against applied pressure, comparing CNF1 and CNF2 results.

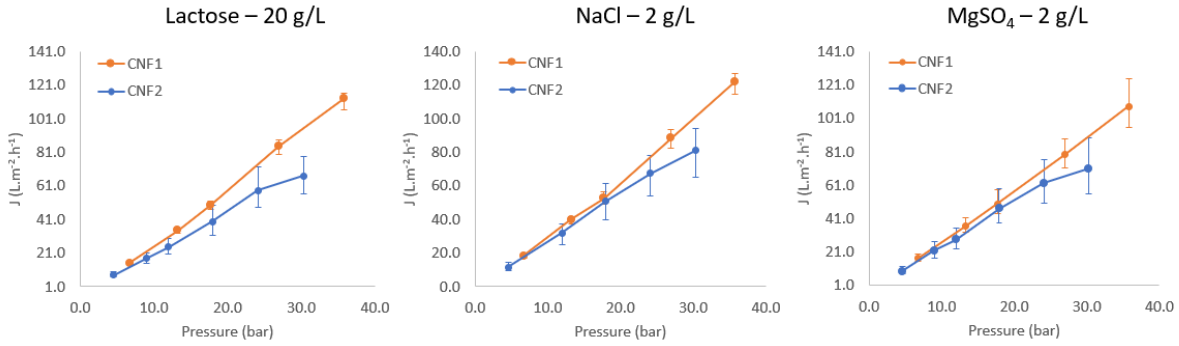

Figure 5.22: Comparison of average permeate flux for CNF1 and CNF2 membranes with varying pressures using three solutes: Lactose, NaCl, and $MgSO_4$.

Generally, CNF2 exhibited superior permeate flux compared to CNF1, particularly at elevated permeate fluxes. This aligns with the hydraulic permeability findings, suggesting that the CNF2 source regions might possess lower permeability properties than those for CNF1.

Finally, Figure 5.23 presents the average rejection results for the CNF2 membrane set in comparison to CNF1. Detailed data is accessible in Appendix C.7.

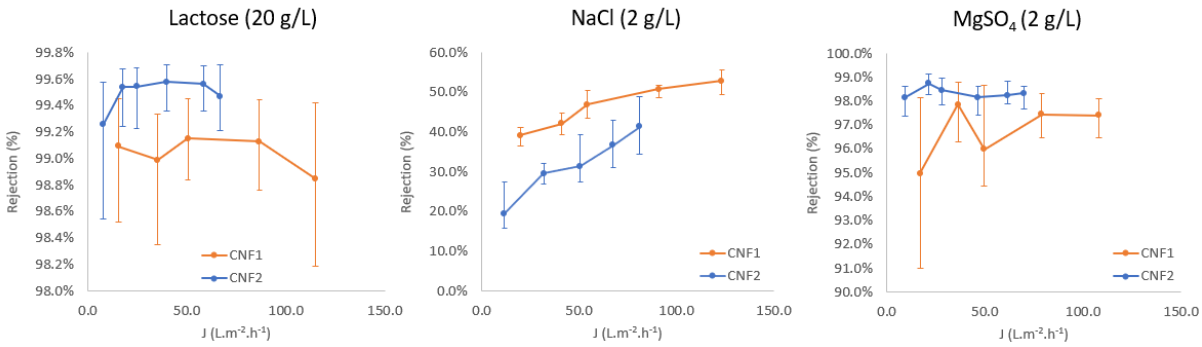

Figure 5.23: Comparison of average rejection rates for CNF1 and CNF2 membranes with varying values of permeate flux, using three solutes: Lactose, NaCl, and $MgSO_4$.

For both Lactose and $MgSO_4$, CNF2 consistently displayed higher rejection rates across all flux ranges. However, in the case of NaCl, CNF1 surpasses CNF2 in rejection. The pronounced lactose rejection aligns with the notion of a denser membrane structure, given that lactose rejection primarily hinges on size-exclusion. Even though $MgSO_4$ and NaCl are both salts, $MgSO_4$'s has a larger ionic radius, which could lead to increased rejection if the membrane's pore size is smaller. Conversely, the significantly smaller size of NaCl implies its rejection predominantly relies on the membrane's surface charge. Given that CNF2's average rejection rates for NaCl were lower, it could be suggested that this particular membrane region might possess a reduced surface charge.

Upon analyzing the error bars, for both rejection and permeate flux, particularly for lactose and $MgSO_4$, it is evident that there is at least one membrane from the new set that reaches the results obtained by the CNF1 set. This indicates that, even though the average results from CNF2 don't exactly mirror those of CNF1, it is still possible to select membranes from the new set that are representative of the CNF2 set.

Considering all the different testing performed within the membrane sheet studied, the research revealed some variations in the inherent properties of membranes depending on their location within the sheet. These variations showed implications for both hydraulic permeability and solute rejection rates. The conducted tests emphasize the importance of thorough testing across multiple samples to choose a truly representative one, especially proven for $MgSO_4$ and lactose. Regarding NaCl, the tests showed potential greater alterations in membrane properties from one sample to another, which for now lacks explanation.

Chapter 6

Conclusions

This study represents an important step in the path of optimizing membrane testing methodologies, particularly in industries that deal with high-value compounds, such as pharmaceutical research. The centrifugal nanofiltration (CNF) device studied in this thesis presents a more sustainable solution in both economic and ecological terms when compared with traditional methods, as it requires fewer resources to achieve the same results.

The design tested in this research proved capable of overcoming some of the challenges faced by previous iterations, handling high-pressure testing without any material damage. Furthermore, the new sealing mechanism effectively prevents leaks, which had been a critical issue in previous designs.

The membrane was tested in the SEPA unit, a commercially available bench-scale unit used to evaluate industrial installations. Even in this certified setup, the typical mass transport limitations were observed, such as solute concentration polarization.

The CNF device demonstrated the ability to replicate the water permeability observed in SEPA unit. However, regarding solute filtration, the device failed to reproduce the permeate fluxes, likely due to the concentration polarization phenomenon. The main reason for the occurrence of this phenomenon is probably the membrane's angle inside the rotor, which introduces heterogeneous pressure across the membrane surface. This uneven pressure likely intensifies concentration polarization, particularly at the membrane's high-flux extremities, as the concentrated solution is pushed towards these regions. These findings highlight the need for a redesigned device that applies a more homogeneous pressure across the membrane.

Another important finding was the inherent variability in membrane characteristics, within the same membrane sheet. This finding accentuated the importance of extensive testing to select a truly representative membrane sample before starting any laboratory tests. This was particularly evident in our tests with $MgSO_4$ and lactose, where some of the membranes perfectly replicated the SEPA results while others did not. Notably, the NaCl tests hinted at possible alterations in membrane properties, a phenomenon that presently lacks a clear explanation but opens a path for future investigative work.

In light of these insights, future research should prioritize the development of a variant of the CNF device with an optimized membrane orientation to minimize concentration polarization. This develop-

ment, along with a deeper investigation into the unexplained membrane behavior with NaCl, will solidify the device's reliability as a membrane testing methodology.

Despite these technical obstacles, the potential of the CNF device cannot be underestimated. It demonstrated significant capability in replicating the results of the SEPA unit, particularly with regard to water permeability and solute rejection rates for $MgSO_4$ and lactose, achieving comparable results while consuming only a fraction of the resources used by the SEPA unit. This performance proves that the device is a promising alternative for sustainable, economical and accurate membrane testing.

In conclusion, the CNF device stands out as a solution for industries wishing to incorporate a more environmentally and economically sustainable option for preliminary membrane testing. Although further research and development are still needed, the progress made establishes a solid foundation for future research and shows the potential of the device.

Bibliography

[1] C. Completo, V. Geraldes, V. Semião, M. Mateus, and M. Rodrigues. Centrifugal nanofiltration for small-volume samples. *Journal of Membrane Science*, 540:411–421, Mar. 2017. doi:10.1016/j.memsci.2017.06.069.

[2] S. A. Hams. Development and optimization of a centrifugal nanofiltration device for small volume samples master-thesis. *Lisboa: Technische Universität Dortmund & Instituto Superior Técnico*, 2018.

[3] M. Correia. Development and optimization of a centrifugal filtration device for small samples master-thesis. *Lisboa: Technische Universität Dortmund & Instituto Superior Técnico*, 2019.

[4] M. C. Porter. *Handbook of Industrial Membrane Technology*. Noyes Publications, reprint edition edition, 1990. ISBN: 0-8155-1205-8.

[5] M. Mulder. *Basic Principles of Membrane Technology*. Kluwer Academic Publishers, 2^{nd} edition, 1996. ISBN: 978-0-7923-4248-9.

[6] R. W. Baker. *Membrane Technology and Applications*. John Wiley & Sons, Ltd, 2^{nd} edition, 2004. ISBN:: 0-470-85445-6.

[7] K. Scott. *Handbook of Industrial Membranes*. Elsevier Science Publishers Ltd, 1^{nd} edition, 1995. ISBN: 1-85617-233-3.

[8] N. Suhalim, N. Kasim, and E. M. et al. Rejection mechanism of ionic solute removal by nanofiltration membranes: An overview. *Nanomaterials*, 12(3), Jan. 2022. doi:10.3390/nano12030437.

[9] E. Ezugbe and S. Rathilal. Membrane technologies in wastewater treatment: A review. *Membranes*, 10(5), Apr. 2020. doi:10.3390/membranes10050089.

[10] S. Kaldis, G. Pantoleontos, and D. Koutsonikolas. Membrane technology in igcc processes for precombustion co2 capture. *Current Trends and Future Developments on (Bio-) Membranes: Carbon Dioxide Separation/Capture by Using Membrane*, (1):329–357, 2018. doi:10.1016/B978-0-12-813645-4.00012-X.

[11] C. Yuenyao, Y. Tirawanichakul, and T. Chittrakarn. Asymmetric polysulfone gas separation membranes treated by low pressure dc glow discharge plasmas. *Journal of Applied Polymer Science*, 132(24), Feb. 2015. doi:10.1002/app.42116.

[12] J. Wang, D. Dlamini, and A. Mishra. A critical review of transport through osmotic membranes. *Journal of Membrane Science*, 454:516–537, Dec. 2014. doi:10.1016/j.memsci.2013.12.034.

[13] J. Wijmans and R. Baker. The solution-diffusion model: a review. *Journal of Membrane Science*, 96(C):16–46, Apr. 1995. doi:10.1016/S0166-4115(08)60038-2.

[14] P. Luis. Introduction. *Fundamental Modeling of Membrane Systems: Membrane and Process Performance*, pages 1–23, 2018. doi:10.1016/B978-0-12-813483-2.00001-0.

[15] A. Abdelrasoul, H. Doan, and A. Lohi. Fouling in membrane filtration and remediation methods. *Mass Transfer - Advances in Sustainable Energy and Environment Oriented Numerical Modeling*, 2013. doi:10.5772/52370.

[16] S. Jagannadh and H. S. Muralidhara. Electrokinetics methods to control membrane fouling. *Industrial and Engineering Chemistry Research*, 35(4):1133–1140, 1996. doi:10.1021/ie9503712.

[17] W. R. Bowen and J. S. Welfoot. Modelling the performance of membrane nanofiltration-critical assessment and model development. *Chemical Engineering Science*, 57(7):1121–1137, 2002. doi:10.1016/S0009-2509(01)00413-4.

[18] A. Mohammad, Y. Teow, and W. A. et al. Nanofiltration membranes review: Recent advances and future prospects. *Desalination*, 356:226–254, Oct. 2015. doi:10.1016/j.desal.2014.10.043.

[19] D. Qadir, H. Mukhtar, and L. Keong. Rejection of divalent ions in commercial tubular membranes: Effect of feed concentration and anion type. *Sustainable Environment Research*, 27(2):103–106, Dec. 2017. doi:10.1016/j.serj.2016.12.002.

[20] Y. Roy, D. M. Warsinger, and J. H. L. V. Effect of temperature on ion transport in nanofiltration membranes: Diffusion, convection and electromigration. *Desalination*, 420:241–257, July 2017. doi:10.1016/j.desal.2017.07.020.

[21] W. R. Bowen, A. W. Mohammad, and N. Hilai. Characterisation of nanofiltration membranes for predictive purposes - use of salts, uncharged solutes and atomic force microscopy. *Journal of Membrane Science*, 126(1):91–105, 1997. doi:10.1016/S0376-7388(96)00276-1.

[22] A. Yaroshchuk. Rejection mechanisms of nf membranes. *Membrane Technology*, (100):9–12, 1998. doi:10.1016/s0958-2118(00)87465-0.

[23] D. Oatley, L. Llenas, R. Pérez, P. Williams, X. Lládo, and M. Rovira. Review of the dielectric properties of nanofiltration membranes and verification of the single oriented layer approximation. *Advances in Colloid and Interface Science*, 173:1–11, Feb. 2012. doi:10.1016/j.cis.2012.02.001.

[24] A. Szymczyk and P. Fievet. Investigating transport properties of nanofiltration membranes by means of a steric, electric and dielectric exclusion model. *Journal of Membrane Science*, 252(1–2):77–88, Jan. 2005. doi:10.1016/j.memsci.2004.12.002.

[25] R. Wang and S. Lin. Pore model for nanofiltration: History, theoretical framework, key predictions, limitations, and prospects. *Journal of Membrane Science*, 620:118809, July 2021. doi:10.1016/j.memsci.2020.118809.

[26] B. Chen, H. Jiang, X. Liu, , and X. Hu. Molecular insight into water desalination across multilayer graphene oxide membranes. *ACS Applied Materials and Interfaces*, 9(27):22826–22836, June 2017. doi:10.1021/acsami.7b05307.

[27] P. M. Wild, G. W. Vickers, and N. Djilali. The fundamental principles and design considerations for the implementation of centrifugal reverse osmosis. *Proceedings of the Institution of Mechanical Engineers, Part E: Journal of Process Mechanical Engineering*, 211(2):67–81, 1997. doi:10.1243/0954408971529566.

[28] J.-L. Auriault, C. Geindreau, and P. Royer. Coriolis effects on filtration law in rotating porous media. *Transport in Porous Media*, 48(3):315–330, 2022. doi:10.1023/A:1015720529464.

[29] *SEPA CF Cell - Assemble & Operation Manual*. Sterlitech Corporation, 2017.

[30] *Operation Manual - Goodrive100-PV Series Solar Pumping VFD*. INVT, v1.1 edition.

[31] D. Wilhelm. Rotating flow simulations with openfoam. *International Journal of Aeronautical Science & Aerospace Research*, 2:1–7, Oct. 2015. doi:10.21256/zhaw-1441.

[32] J. J. Barron and C. Ashton. The effect of temperature on conductivity measurement. *American Journal of Physics and Applications*, 5(1), 2017. doi:10.11648/j.ajpa.20170501.11.

Appendix A

Chapter 3 Appendixes

A.1 Membrane Properties

Table A.1: Properties of membrane used (NFS (TFC 100-250Da) - Sanitary NF Membrane, by *Synder Filtration (California, USA)*. The properties listed were consulted in the pdf downloaded from *Synder*'s website in September 2022.

Property	**Value**
Model	NFS
Polymer	Proprietary PA TFC
Approx. Molecular Weight Cutoff	100-250 Da
Typical Operating Flux	30-40 GDF
Average Lactose Rejection[1] (%)	99.5
Average MgSO4 Rejection[2] (%)	99.5
Average NaCl Rejection[3] (%)	50.0
Max. Operating Pressure if T$<$95ºC (bar)	41.5
Max. Operating Pressure if T$>$95ºC (bar)	30.0
Max. Operating Temperature (ºC)	50.0
pH range at Max. Temperature	3-9.5
pH range at Ambient Temperature	3-10.5

[1]Test Conditions 2% Lactose Solution at 110PSI (7.6 Bar) operating pressure, 77° F (25° C)

[2]Test Conditions 2,000ppm $MgSO_4$ Solution at 110PSI (7.6 Bar) operating pressure, 77° F (25° C)

[3]Test Conditions 2,000ppm $NaCl$ Solution at 110PSI (7.6 Bar) operating pressure, 77° F (25° C)

A.2 SEPA Properties

Table A.2: SEPA unit features and technical specification.

Parameter	**Description**
Membrane Active Area (cm^2)	140
Hold-Up Volume (mL)	70
Maximum Pressure: 316SS Cell Body (bar)	69
Maximum Temperature: 316SS Cell Body (ºC)	177
O-rings	Viton
pH Range	Membrane Dependent
Cross Flow Velocity	Variable
Dimensions	
Slot Depth (mm)	1.09
Slot Width (mm)	146

A.3 Frequency Calibration Line

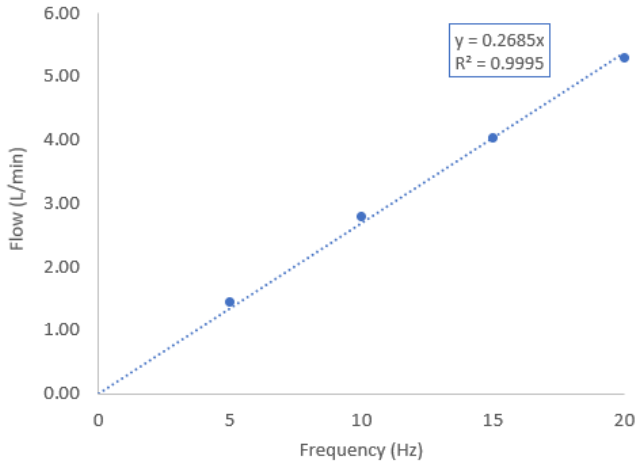

Frequency (Hz)	Flow (L/min)
5.00	1.45
10.00	2.79
15.00	4.03
20.00	5.29

Figure A.1: Linear regression of flow as a function of frequency.

A.4 Calibration Lines

A.4.1 $MgSO_4$

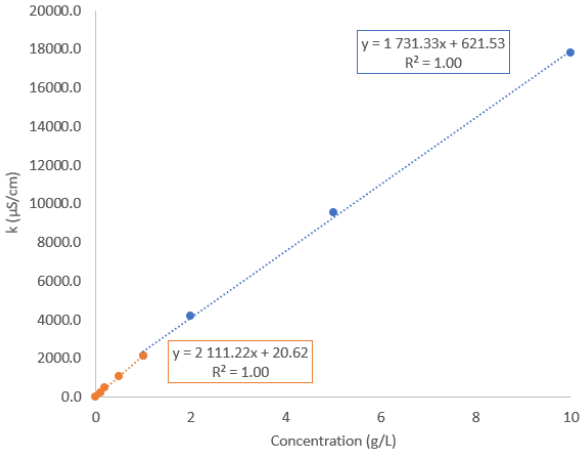

Concentration (g/L)	k (µS/cm)
10.00	17820.0
5.00	9510.0
2.00	4190.0
1.00	2130.0
0.50	1070.0
0.20	466.0
0.10	235.0
0	2.3

Figure A.2: $MgSO_4$ calibration lines, for higher and lower concentrations. The line for lower concentration is used to determine the concentration of the permeate and other is used to determine the concentration of the concentrate.

A.4.2 NaCl

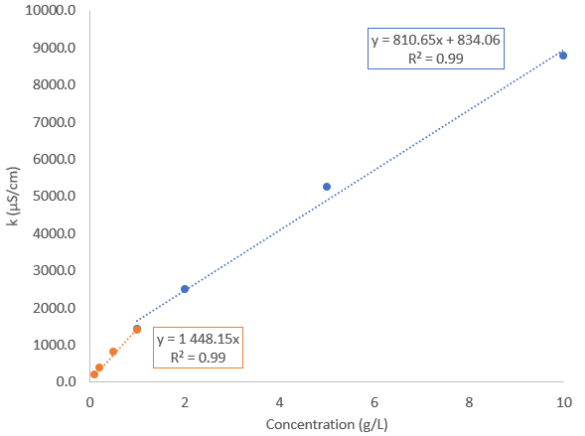

Concentration (g/L)	k (µS/cm)
10.00	8780.0
5.00	5240.0
2.00	2490.0
1.00	1418.0
0.50	799.0
0.20	372.0
0.10	207.0
0	1.3

Figure A.3: NaCl calibration lines, for higher and lower concentrations. The line for lower concentration is used to determine the concentration of the permeate and other is used to determine the concentration of the concentrate.

A.4.3 Lactose

Calibration line for low concentrations, used to determine the concentration of the permeate:

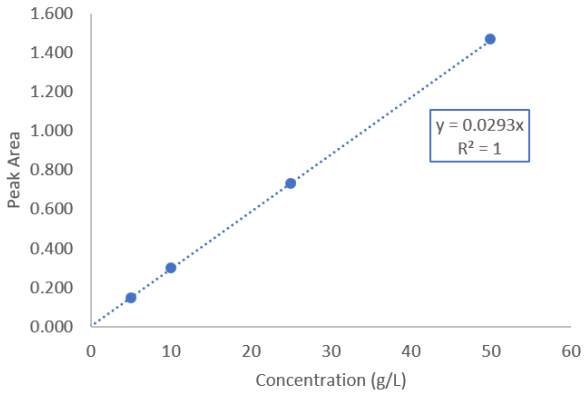

Concentration (g/L)	Peak Area
5.00	0.147
10.00	0.294
25.00	0.729
50.00	1.464

Figure A.4: Lactose calibration line, for low concentrations.

Calibration line for higher concentrations, used to determine the concentration of the concentrate:

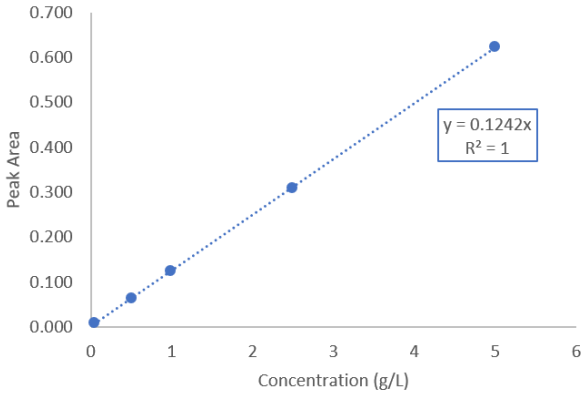

Concentration (g/L)	Peak Area
0.05	0.008
0.50	0.063
1.00	0.125
2.50	0.308
5.00	0.622

Figure A.5: Lactose calibration lines, for higher concentrations.

Appendix B

Chapter 4 Appendixes

B.1 Hydraulic permeability (SEPA)

Water permeate flux ($L.h^{-1}.m^{-2}$):

Área ativa da membrana
0.014 m2

Pressure (bar)	Pressure (Pa)	Volume (mL)	Time (s)	Permeate flow (mL/min)	Permeate flow (L/min)	Permeate flux (L.m-2.h-1)
40.0	4000000	19.0	26.9	42.4	0.0424	181.6
30.0	3000000	19.0	36.7	31.1	0.0311	133.1
20.0	2000000	18.7	54.0	20.8	0.0208	89.0
10.0	1000000	15.1	82.0	11.0	0.0110	47.4
5.0	500000	10.8	118.1	5.5	0.0055	23.5

B.2 Membrane rejection and permeate flux (SEPA)

Rejection (%):

Lactose:

Pressure (bar)	5 g/L	10 g/L	20 g/L			
			I	II	III	Average
7.6	98.17%	99.20%	99.04%	99.13%	99.26%	99.15%
15.0	98.20%	99.40%	99.26%	98.52%	99.28%	99.02%
20.0	98.76%	99.18%	99.30%	99.40%	99.28%	99.33%
30.0	98.97%	99.11%	99.36%	99.18%	99.31%	99.29%
40.0	98.94%	99.21%	99.26%	99.14%	98.85%	99.08%

NaCl:

Pressure (bar)	1 g/L	2 g/L				5 g/L	10 g/L
		I	II	III	Average		
7.6	85.24%	76.59%	73.38%	73.00%	74.32%	52.14%	39.18%
15.0	90.62%	82.92%	80.40%	78.74%	80.69%	69.05%	55.74%
20.0	90.71%	84.21%	81.18%	79.44%	81.61%	70.93%	60.37%
30.0	89.60%	83.57%	82.99%	79.31%	81.96%	72.85%	65.49%
40.0	90.58%	81.09%	83.66%	79.46%	81.40%	73.36%	66.10%

$MgSO_4$:

Pressure (bar)	1 g/L	2 g/L				5 g/L	10 g/L
		I	II	III	Average		
7.6	96.60%	97.09%	97.87%	98.30%	97.76%	96.87%	97.16%
15.0	97.25%	97.24%	97.52%	98.54%	97.77%	97.32%	97.69%
20.0	97.21%	97.56%	97.59%	98.66%	97.94%	97.19%	97.90%
30.0	97.38%	97.34%	97.91%	98.17%	97.81%	97.45%	97.39%
40.0	97.24%	97.34%	97.86%	98.61%	97.94%	96.84%	96.85%

Permeate flux ($L.h^{-1}.m^{-2}$):

Lactose:

Pressure (bar)	5 g/L	10 g/L	20 g/L			
			I	II	III	Average
7.6	30.1	29.0	28.8	23.9	23.5	25.4
15.0	65.8	63.8	62.9	56.6	53.9	57.8
20.0	91.4	91.4	88.7	77.1	71.6	79.1
30.0	143.2	143.6	140.6	119.2	113.2	124.3
40.0	200.4	198.3	164.5	158.4	153.1	158.7

NaCl:

Pressure (bar)	1 g/L	2 g/L				5 g/L	10 g/L
		I	II	III	Average		
7.6	32.4	30.0	34.4	30.9	31.8	26.3	21.7
15.0	68.5	68.5	77.0	70.3	71.9	59.3	50.9
20.0	96.1	92.2	103.5	97.3	97.6	84.8	73.2
30.0	152.1	149.6	158.8	152.5	153.7	142.1	130.1
40.0	214.3	216.7	219.8	210.2	215.6	195.8	172.2

$MgSO_4$:

Pressure (bar)	1 g/L	2 g/L				5 g/L	10 g/L
		I	II	III	Average		
7.6	31.0	27.4	29.9	26.4	27.9	24.6	20.0
15.0	62.8	60.3	60.2	58.2	59.5	54.6	50.3
20.0	88.1	85.6	79.6	79.6	81.6	76.3	69.6
30.0	137.8	139.4	126.5	125.9	130.6	120.5	114.9
40.0	191.9	204.6	172.2	175.7	184.2	171.4	158.7

Appendix C

Chapter 5 Appendixes

C.1 Pressure simulation

Transmembrane pressure (maximum capacity):

Speed (rpm)	Integrated pressure	p/rho (m^2/s^2)	Pressure (Pa)	Pressure (bar)
3000	0.054617	224.8	224787.9	2.25
5000	0.151537	623.7	623688.6	6.24
7000	0.297063	1222.6	1222637.5	12.23
9000	0.494107	2033.6	2033621.6	20.34
10000	0.609541	2508.7	2508719.2	25.09
11000	0.737891	3037.0	3036975.9	30.37
12000	0.879654	3620.4	3620437.2	36.20
13000	1.031250	4244.4	4244368.6	42.44
14000	1.195950	4922.2	4922232.9	49.22
15000	1.375660	5661.9	5661874.6	56.62
16000	1.561080	6425.0	6425017.2	64.25

Transmembrane pressure for different concentrate initial volumes:

5 mL:

Speed (rpm)	Surface			Membrane (Max fluid)	Membrane (10 mL fluid)
	p/rho (m^2/s^2)	Pressure (Pa)	Pressure (bar)	Pressure (bar)	Pressure (bar)
3000	140	140000	1.40	2.25	0.85
5000	400	400000	4.00	6.24	2.24
7000	780	780000	7.80	12.23	4.43
9000	1300	1300000	13.00	20.34	7.34
10000	1600	1600000	16.00	25.09	9.09
11000	1900	1900000	19.00	30.37	11.37
12000	2300	2300000	23.00	36.20	13.20
13000	2700	2700000	27.00	42.44	15.44
14000	3100	3100000	31.00	49.22	18.22
15000	3600	3600000	36.00	56.62	20.62
16000	4100	4100000	41.00	64.25	23.25

7 mL:

Speed (rpm)	Surface			Membrane (Max fluid)	Membrane (10 mL fluid)
	p/rho (m^2/s^2)	Pressure (Pa)	Pressure (bar)	Pressure (bar)	Pressure (bar)
3000	120	120000	1.20	2.25	1.05
5000	320	320000	3.20	6.24	3.04
7000	630	630000	6.30	12.23	5.93
9000	1100	1100000	11.00	20.34	9.34
10000	1300	1300000	13.00	25.09	12.09
11000	1600	1600000	16.00	30.37	14.37
12000	1900	1900000	19.00	36.20	17.20
13000	2200	2200000	22.00	42.44	20.44
14000	2600	2600000	26.00	49.22	23.22
15000	2900	2900000	29.00	56.62	27.62
16000	3300	3300000	33.00	64.25	31.25

10 mL:

Speed (rpm)	Surface			Membrane (Max fluid)	Membrane (10 mL fluid)
	p/rho (m^2/s^2)	Pressure (Pa)	Pressure (bar)	Pressure (bar)	Pressure (bar)
3000	79	79000	0,79	2,25	1,46
5000	220	220000	2,20	6,24	4,04
7000	432	432000	4,32	12,23	7,91
9000	720	720000	7,20	20,34	13,14
10000	890	890000	8,90	25,09	16,19
11000	1100	1100000	11,00	30,37	19,37
12000	1300	1300000	13,00	36,20	23,20
13000	1500	1500000	15,00	42,44	27,44
14000	1800	1800000	18,00	49,22	31,22
15000	2000	2000000	20,00	56,62	36,62
16000	2300	2300000	23,00	64,25	41,25

12 mL:

Speed (rpm)	Surface			Membrane (Max fluid)	Membrane (10 mL fluid)
	p/rho (m^2/s^2)	Pressure (Pa)	Pressure (bar)	Pressure (bar)	Pressure (bar)
3000	57	57000	0.57	2.25	1.68
5000	160	160000	1.60	6.24	4.64
7000	310	310000	3.10	12.23	9.13
9000	530	530000	5.30	20.34	15.04
10000	650	650000	6.50	25.09	18.59
11000	780	780000	7.80	30.37	22.57
12000	930	930000	9.30	36.20	26.90
13000	1100	1100000	11.00	42.44	31.44
14000	1300	1300000	13.00	49.22	36.22
15000	1400	1400000	14.00	56.62	42.62
16000	1600	1600000	16.00	64.25	48.25

15 mL:

Speed (rpm)	Surface			Membrane (Max fluid)	Membrane (10 mL fluid)
	p/rho (m^2/s^2)	Pressure (Pa)	Pressure (bar)	Pressure (bar)	Pressure (bar)
3000	25	25000	0.25	2.25	2.00
5000	72	72000	0.72	6.24	5.52
7000	150	150000	1.50	12.23	10.73
9000	240	240000	2.40	20.34	17.94
10000	300	300000	3.00	25.09	22.09
11000	360	360000	3.60	30.37	26.77
12000	430	430000	4.30	36.20	31.90
13000	500	500000	5.00	42.44	37.44
14000	600	600000	6.00	49.22	43.22
15000	680	680000	6.80	56.62	49.82
16000	780	780000	7.80	64.25	56.45

C.2 Pressure correction (CNF1)

Water:

Test	Initial volume (mL)	Final volume (mL)	Initial pressure (bar)	Final pressure (bar)	Corrected pressure (bar)
5 bar - 5600 rpm	10.08	8.5	4.9	4.3	4.6
10 bar - 7900 rpm	10.09	8.5	9.9	8.6	9.2
20 bar - 11100 rpm	10.05	8.1	19.7	16.6	18.2
30 bar - 13600 rpm	10.04	8.1	29.7	25.0	27.3
40 bar - 15700 rpm	10.07	7.7	39.7	31.9	35.8

Lactose - 20 g/L:

Test	Initial volume (mL)	Final volume (mL)	Initial pressure (bar)	Final pressure (bar)	Corrected pressure (bar)
7.6 bar - 6900 rpm	10.15	8.04	7.5	6.2	6.9
15 bar - 9600 rpm	10.15	7.75	14.9	12.0	13.4
20 bar - 11100 rpm	10.13	7.70	19.9	16.0	17.9
30 bar - 13600 rpm	10.16	7.73	30.0	24.1	27.0
40 bar - 15700 rpm	10.16	7.86	40.0	32.6	36.3

$MgSO_4$ - 2 g/L:

Test	Initial volume (mL)	Final volume (mL)	Initial pressure (bar)	Final pressure (bar)	Corrected pressure (bar)
7.6 bar - 6900 rpm	10.11	7.78	7.5	6.1	6.8
15 bar - 9600 rpm	10.10	7.62	14.8	11.8	13.3
20 bar - 11100 rpm	10.07	7.48	19.8	15.6	17.7
30 bar - 13600 rpm	10.08	7.87	29.8	24.4	27.1
40 bar - 15700 rpm	10.08	7.48	39.8	31.4	35.6

$MgSO_4$ - 1 g/L:

Test	Initial volume (mL)	Final volume (mL)	Initial pressure (bar)	Final pressure (bar)	Corrected pressure (bar)
7.6 bar - 6900 rpm	10.07	7.45	7.5	5.9	6.7
15 bar - 9600 rpm	10.05	7.38	14.8	11.5	13.2
20 bar - 11100 rpm	10.11	7.63	19.8	15.8	17.8
30 bar - 13600 rpm	10.14	7.75	29.9	24.1	27.0
40 bar - 15700 rpm	10.13	7.32	39.9	30.9	35.4

NaCl - 2 g/L:

Test	Initial volume (mL)	Final volume (mL)	Initial pressure (bar)	Final pressure (bar)	Corrected pressure (bar)
7.6 bar - 6900 rpm	10.08	7.37	7.5	5.8	6.6
15 bar - 9600 rpm	10.12	7.31	14.9	11.5	13.2
20 bar - 11100 rpm	10.05	7.22	19.7	15.2	17.5
30 bar - 13600 rpm	10.10	7.55	29.8	23.6	26.7
40 bar - 15700 rpm	10.10	7.63	39.8	31.9	35.8

C.3 Pressure correction (CNF2)

Water:

Test	Initial volume (mL)	Final volume (mL)	Initial pressure (bar)	Final pressure (bar)	Corrected pressure (bar)
7 bar - 6600 rpm	9.99	9.19	6.9	6.4	6.6
13.7 bar - 9200 rpm	9.99	9.27	13.4	12.6	13.0
20.2 bar - 11200 rpm	9.99	9.00	19.9	18.3	19.1
26.8 bar - 12900 rpm	9.99	8.67	26.4	23.6	25.0

Lactose - 20 g/L:

Test	Initial volume (mL)	Final volume (mL)	Initial pressure (bar)	Final pressure (bar)	Corrected pressure (bar)
5.3 bar - 5700 rpm	10.11	9.05	5.1	4.7	4.9
9.8 bar - 7800 rpm	10.05	8.68	9.5	8.5	9.0
12.8 bar - 8900 rpm	10.19	8.81	12.9	11.4	12.1
19.5 bar - 11000 rpm	10.02	8.70	19.1	17.0	18.0
26 bar - 12700 rpm	10.10	8.82	25.6	23.0	24.3
32.1 bar - 14100 rpm	10.14	8.91	32.2	29.0	30.6

$MgSO_4$ - 2 g/L:

Test	Initial volume (mL)	Final volume (mL)	Initial pressure (bar)	Final pressure (bar)	Corrected pressure (bar)
4.9 bar - 5500 rpm	10.07	8.78	4.9	4.4	4.6
9.8 bar - 7800 rpm	10.05	8.58	9.5	8.4	9.0
12.8 bar - 8900 rpm	10.05	8.58	12.7	11.2	12.0
19.5 bar - 11000 rpm	10.01	8.50	19.0	16.7	17.9
26 bar - 12700 rpm	10.04	8.55	25.5	22.4	24.0
32.1 bar - 14100 rpm	10.05	8.63	32.0	28.3	30.1

NaCl - 2 g/L:

Test	Initial volume (mL)	Final volume (mL)	Initial pressure (bar)	Final pressure (bar)	Corrected pressure (bar)
4.5 bar - 5300 rpm	10.09	8.51	4.5	3.9	4.2
12.8 bar - 11100 rpm	10.02	8.37	12.7	11.0	11.8
19.5 bar - 13600 rpm	10.12	8.45	19.2	16.6	17.9
26 bar - 15700 rpm	10.12	8.66	25.7	22.6	24.2
32.1 bar - 14100 rpm	10.13	8.62	32.2	28.3	30.2

C.4 Hydraulic permeability (CNF1)

Water permeate flux ($L.h^{-1}.m^{-2}$):

Pressure (bar)	5.0	10.0	20.0	30.0	40.0
Corrected pressure (bar)	4.6	9.2	18.2	27.3	35.8
Device 1	23.1	45.1	85.2	125.3	153.8
Device 2	25.4	56.7	86.9	135.3	150.3
Device 3	35.1	42.8	83.5	125.9	150.9
Device 4	23.2	40.8	79.2	119.1	149.4
Device 5	25.2	44.2	80.4	118.8	150.0
Device 6	20.2	39.7	78.1	115.3	141.6
Device 7	18.1	35.7	66.7	104.7	130.6
Device 8	23.0	44.2	86.5	127.2	148.4
Device 9	25.4	47.9	95.8	139.4	191.9
Device 10	21.7	44.0	77.3	117.8	155.0
Device 11	20.8	41.0	80.8	118.4	152.5
Device 12	18.8	36.5	69.6	102.8	132.2
Device 13	19.3	36.9	72.7	106.9	141.6
Device 14	23.1	46.1	84.6	134.1	163.4
Average	23.0	43.0	80.5	120.8	150.8
Deviation up	12.1	13.7	15.3	18.6	41.0
Deviation down	4.9	7.3	13.9	18.0	20.2

Average (1 to 8)	24.2	43.6	80.8	121.4	146.9
Deviation up	10.9	13.0	6.1	13.9	6.9
Deviation down	6.0	8.0	14.1	16.8	16.3

C.5 Solute rejection and permeate flux (CNF1)

Rejection (%):

	Lactose (20 g/L)					NaCl (2 g/L)				
Pressure (bar)	7.6	15.0	20.0	30.0	40.0	7.6	15.0	20.0	30.0	40.0
Corrected pressure (bar)	6.7	13.3	17.7	27.0	35.8	6.7	13.3	17.7	27.0	35.8
Device 1	98.60%	98.39%	99.08%	98.75%	98.47%	33.02%	38.20%	36.82%	46.52%	42.34%
Device 2	95.69%	96.32%	97.48%	96.85%	96.79%	35.54%	37.53%	42.43%	43.47%	47.54%
Device 3	92.39%	77.36%	92.96%	87.57%	93.75%	28.12%	31.83%	40.44%	40.91%	43.34%
Device 4	99.33%	99.34%	99.35%	99.33%	98.97%	40.15%	43.38%	50.38%	51.75%	54.03%
Device 5	95.43%	96.15%	97.29%	96.67%	97.46%	37.19%	36.98%	41.34%	46.68%	53.03%
Device 6	99.07%	98.94%	98.84%	98.98%	98.83%	38.83%	39.40%	45.10%	51.39%	49.53%
Device 7	99.45%	99.34%	99.45%	99.45%	99.42%	41.19%	44.68%	48.90%	51.46%	55.60%
Device 8	98.52%	98.35%	98.97%	98.76%	98.19%	36.48%	41.20%	43.38%	48.57%	52.39%
Average	97.31%	95.52%	97.93%	97.05%	97.74%	36.31%	39.15%	43.60%	47.59%	49.72%
Average (4, 6, 7, 8)	99.09%	98.99%	99.15%	99.13%	98.85%	39.16%	42.17%	46.94%	50.79%	52.89%
Deviation up	0.36%	0.35%	0.30%	0.32%	0.57%	2.03%	2.52%	3.44%	0.95%	2.71%
Deviation down	0.57%	0.64%	0.31%	0.37%	0.67%	2.68%	2.76%	3.56%	2.22%	3.35%

	MgSO4 (2 g/L)					MgSO4 (1 g/L)				
Pressure (bar)	7.6	15.0	20.0	30.0	40.0	7.6	15.0	20.0	30.0	40.0
Corrected pressure (bar)	6.7	13.3	17.7	27.0	35.8	6.7	13.3	17.7	27.0	35.8
Device 1	95.69%	93.86%	94.91%	96.26%	96.69%	94.76%	92.88%	96.26%	96.47%	97.54%
Device 2	81.88%	91.78%	90.85%	92.38%	89.96%	92.43%	88.45%	86.85%	91.00%	93.91%
Device 3	79.48%	83.54%	88.76%	67.22%	89.14%	78.40%	90.44%	90.28%	83.39%	89.17%
Device 4	98.15%	98.64%	96.33%	97.99%	97.79%	93.93%	96.12%	93.12%	96.91%	98.23%
Device 5	88.22%	90.85%	91.08%	86.75%	88.02%	88.15%	90.68%	87.38%	91.26%	94.24%
Device 6	95.23%	97.69%	94.45%	97.00%	97.23%	92.58%	95.89%	92.05%	94.57%	94.22%
Device 7	90.99%	98.80%	98.68%	98.33%	98.09%	94.56%	95.50%	93.75%	96.12%	94.33%
Device 8	95.50%	96.28%	94.48%	96.45%	96.48%	94.50%	94.54%	93.18%	96.29%	96.90%
Average	90.64%	93.93%	93.69%	91.55%	94.18%	91.16%	93.06%	91.61%	93.25%	94.82%
Average (4, 6, 7, 8)	94.97%	97.85%	95.99%	97.44%	97.40%	93.89%	95.51%	93.03%	95.97%	95.92%
Deviation up	3.18%	0.95%	2.69%	0.89%	0.69%	0.66%	0.61%	0.72%	0.94%	2.31%
Deviation down	3.98%	1.57%	1.53%	0.99%	0.91%	1.31%	0.97%	0.97%	1.40%	1.70%

Permeate flux ($L.h^{-1}.m^{-2}$):

	Lactose (20 g/L)					NaCl (2 g/L)				
Pressure (bar)	7.6	15.0	20.0	30.0	40.0	7.6	15.0	20.0	30.0	40.0
Corrected pressure (bar)	6.7	13.3	17.7	27.0	35.8	6.7	13.3	17.7	27.0	35.8
Device 1	16.6	37.5	56.7	94.6	127.5	23.0	46.5	63.8	102.5	141.0
Device 2	15.5	34.7	50.2	88.2	114.0	21.1	40.9	55.0	89.6	120.5
Device 3	17.2	40.3	53.3	93.9	124.0	23.1	44.7	55.8	97.9	129.5
Device 4	15.4	35.6	49.6	84.6	116.0	19.3	41.3	52.7	90.4	125.5
Device 5	14.3	32.2	46.3	78.2	101.0	18.0	37.5	49.6	83.9	108.0
Device 6	14.9	34.6	49.2	85.7	114.5	18.3	39.9	52.9	87.1	121.5
Device 7	14.5	32.5	47.1	79.6	106.5	17.0	37.2	48.8	82.5	114.5
Device 8	15.4	35.6	52.1	88.6	115.5	19.2	41.8	56.3	93.9	127.0
Average	15.5	35.4	50.5	86.7	114.9	19.9	41.2	54.4	91.0	123.4
Average (4, 6, 7, 8)	15.1	34.6	49.5	84.6	113.1	18.5	40.0	52.7	88.5	122.1
Deviation up	0.4	1.0	2.6	3.9	2.9	0.9	1.7	3.7	5.4	4.9
Deviation down	0.6	2.1	2.4	5.0	6.6	1.5	2.8	3.8	6.0	7.6

	MgSO4 (2 g/L)					MgSO4 (1 g/L)				
Pressure (bar)	7.6	15.0	20.0	30.0	40.0	7.6	15.0	20.0	30.0	40.0
Corrected pressure (bar)	6.7	13.3	17.7	27.0	35.8	6.7	13.3	17.7	27.0	35.8
Device 1	17.9	39.0	58.3	88.6	125.0	21.3	45.3	59.6	96.1	132.1
Device 2	18.0	37.5	49.4	80.4	111.3	19.3	40.1	51.0	86.8	120.8
Device 3	19.9	41.5	54.0	86.8	115.4	20.3	43.4	55.8	96.4	129.6
Device 4	17.0	35.7	48.1	78.2	107.5	19.1	39.1	49.6	80.0	110.0
Device 5	15.4	32.8	44.6	71.4	95.8	17.9	35.1	47.7	76.8	104.6
Device 6	16.4	35.4	47.5	76.1	104.6	19.4	39.3	51.3	83.9	107.9
Device 7	15.7	32.9	44.0	71.4	97.9	17.2	31.6	45.2	75.4	112.9
Device 8	16.8	36.5	51.9	80.0	108.3	19.4	40.6	52.5	85.7	116.7
Average	17.1	36.4	49.7	79.1	108.2	19.2	39.3	51.6	85.1	116.8
Average (4, 6, 7, 8)	16.5	35.1	47.9	76.4	104.6	18.8	37.6	49.6	81.3	111.9
Deviation up	0.5	1.3	4.0	3.6	3.8	0.6	2.9	2.9	4.5	4.8
Deviation down	0.8	2.2	3.8	5.0	6.7	1.6	6.0	4.4	5.9	4.0

C.6 Hydraulic permeability (CNF2)

Water permeate flux ($L.h^{-1}.m^{-2}$):

Pressure (bar)	7.0	13.7	20.2	26.8
Corrected pressure (bar)	6.6	13.0	19.1	25.0
Device 1	28.6	56.0	80.0	106.9
Device 2	23.9	45.3	64.4	86.9
Device 3	24.4	46.0	66.6	90.0
Device 4	18.1	35.1	51.9	69.4
Device 5	20.0	37.3	53.4	71.9
Device 6	17.5	32.9	48.8	61.3
Device 7	25.3	49.9	72.2	94.4
Device 8	21.1	40.4	60.3	79.4
Average	22.4	42.9	62.2	82.5
Deviation up	6.3	13.1	17.8	24.4
Deviation down	4.9	10.0	13.4	21.3

Average (1, 2, 3, 7)	25.6	49.3	70.8	94.5
Deviation up	3.1	6.7	9.2	12.3
Deviation down	1.7	4.0	6.4	7.7

C.7 Membrane rejection and permeate flux (CNF2)

Rejection (%):

	Lactose (20 g/L)						NaCl (2 g/L)					MsSO4 (2 g/L)					
Pressure (bar)	4.9	9.8	12.8	19.5	26.0	32.1	4.9	12.8	19.5	26.0	32.1	4.9	9.8	12.8	19.5	26.0	32.1
Corrected pressure (bar)	4.6	9.0	12.0	17.9	24.1	30.3	4.6	12.0	17.9	24.1	30.3	4.6	9.0	12.0	17.9	24.1	30.3
Device 1	99.58%	99.67%	99.65%	99.66%	99.54%	99.71%	17.31%	31.29%	29.05%	34.89%	34.54%	97.97%	98.80%	98.02%	98.15%	97.91%	98.53%
Device 2	99.11%	99.46%	99.50%	99.39%	99.62%	99.21%	15.80%	27.07%	28.77%	31.22%	36.83%	98.46%	98.32%	97.86%	98.16%	98.29%	98.53%
Device 3	99.46%	99.64%	99.68%	99.68%	99.70%	99.41%	16.36%	30.05%	30.65%	38.75%	38.84%	98.07%	98.81%	98.90%	98.21%	98.09%	97.68%
Device 4	99.30%	99.60%	99.57%	99.57%	99.68%	99.69%	21.00%	27.85%	29.41%	36.58%	41.87%	98.23%	98.75%	98.86%	98.64%	98.85%	98.41%
Device 5	99.47%	99.63%	99.67%	99.68%	99.68%	99.46%	22.16%	32.06%	35.26%	39.23%	48.83%	98.62%	99.15%	98.95%	98.47%	98.33%	98.61%
Device 6	99.37%	99.54%	99.51%	99.71%	99.37%	99.47%	27.56%	31.36%	39.27%	43.06%	47.21%	98.47%	99.09%	98.65%	98.08%	98.30%	98.36%
Device 7	98.54%	99.24%	99.23%	99.36%	99.36%	99.34%	16.25%	27.65%	27.41%	33.55%	41.22%	97.37%	98.29%	97.98%	97.41%	97.91%	98.28%
Device 8	99.16%	99.65%	—	—	—	—	20.66%	41.50%	—	—	—	96.79%	97.49%	97.57%	97.83%	98.11%	98.24%
Average	99.25%	99.55%	99.54%	99.58%	99.56%	99.47%	19.64%	31.10%	31.40%	36.75%	41.33%	98.00%	98.59%	98.35%	98.12%	98.22%	98.33%
Average (except 8)	99.26%	99.54%	99.54%	99.58%	99.56%	99.47%	19.49%	29.62%	31.40%	36.75%	41.33%	98.17%	98.74%	98.46%	98.16%	98.24%	98.34%
Deviation up	0.32%	0.13%	0.14%	0.13%	0.14%	0.24%	8.07%	2.44%	7.87%	6.30%	7.50%	0.45%	0.40%	0.49%	0.48%	0.61%	0.27%
Deviation down	0.72%	0.30%	0.32%	0.22%	0.21%	0.26%	3.69%	2.55%	4.00%	5.53%	6.80%	0.80%	0.45%	0.60%	0.75%	0.33%	0.66%

Permeate flux ($L.h^{-1}.m^{-2}$):

	Lactose (20 g/L)						**NaCl (2 g/L)**					**MsSO4 (2 g/L)**					
Pressure (bar)	4.9	9.8	12.8	19.5	26.0	32.1	4.9	12.8	19.5	26.0	32.1	4.9	9.8	12.8	19.5	26.0	32.1
Corrected pressure (bar)	4.6	9.0	12.0	17.9	24.1	30.3	4.6	12.0	17.9	24.1	30.3	4.6	9.0	12.0	17.9	24.1	30.3
Device 1	10.0	21.2	29.8	49.4	72.5	78.5	14.3	36.4	61.7	77.5	93.0	12.1	27.2	35.4	59.1	76.3	89.5
Device 2	8.6	18.9	26.3	43.6	62.5	74.5	12.8	35.5	55.8	73.3	88.0	10.2	23.2	30.2	50.0	67.5	76.0
Device 3	7.9	18.2	26.3	40.8	61.3	69.5	11.8	33.0	50.8	70.4	84.5	9.7	22.4	29.0	48.8	65.0	71.0
Device 4	6.7	15.5	21.0	33.6	50.0	57.0	10.4	27.5	42.8	57.1	68.5	8.1	17.9	23.7	39.7	52.5	60.0
Device 5	7.4	15.7	22.2	34.7	52.9	60.5	10.3	27.9	44.2	62.1	74.5	8.1	19.3	25.2	41.9	56.7	62.0
Device 6	6.5	14.6	20.3	31.4	48.3	56.5	9.3	25.0	40.0	54.2	65.0	7.6	17.2	23.1	38.4	50.4	55.5
Device 7	8.4	20.0	26.7	45.0	61.3	72.0	13.0	37.3	60.0	78.3	94.0	9.9	23.1	30.4	49.1	62.9	75.5
Device 8	6.8	19.5	12.2	16.1	18.3	24.0	10.8	12.7	15.0	13.8	16.5	9.8	23.2	29.8	49.1	65.0	77.0
Average	7.8	17.9	23.1	36.8	53.4	61.6	11.6	29.4	46.3	60.8	73.0	9.4	21.7	28.3	47.0	62.0	70.8
Average (except 8)	7.9	17.7	24.7	39.8	58.4	66.9	11.7	31.8	50.8	67.6	81.1	9.4	21.5	28.1	46.7	61.6	69.9
Deviation up	0.4	2.3	2.0	5.2	2.9	5.1	1.3	5.5	9.2	10.8	12.9	0.5	1.8	2.3	2.4	3.4	7.1
Deviation down	1.4	3.1	4.3	8.4	10.1	10.4	2.4	6.8	10.8	13.4	16.1	1.7	4.3	5.1	8.3	11.2	14.4